Multibody Dynamics Modelling and Analysis of the Human Hand

by

André Rui Dantas Carvalho
BSc, Instituto Superior Técnico, 2005

A Thesis Submitted in Partial Fulfillment
of the Requirements for the Degree of
MASTER OF APPLIED SCIENCE
in the
Department of Mechanical Engineering

SUPERVISOR COMMITTEE

Dr. Afzal Suleman, Supervisor (Dept. of Mechanical Engineering, University of Victoria)

Dr. Ron Podhorodeski, Member (Dept. of Mechanical Engineering, University of Victoria)

Dr. Daniela Constantinescu, Member (Dept. of Mechanical Engineering, University of Victoria)

Dr. Pan Agathoklis, External Examiner (Dept. of Electrical and Computer Engineering, University of Victoria)

Supervisor Committee:
Dr. Afzal Suleman, Supervisor (Dept. of Mechanical Engineering, University of Victoria)

Dr. Ron Podhorodeski, Member (Dept. of Mechanical Engineering, University of Victoria)

Dr. Daniela Constantinescu, Member (Dept. of Mechanical Engineering, University of Victoria)

Dr. Pan Agathoklis, External Examiner (Dept. of Electrical and Computer Engineering, University of Victoria)

ABSTRACT

This thesis presents a simulation model for the dynamics of the human hand for application to an anthropomorphic prosthesis. The Articulated Body Algorithm (ABA) algorithm was selected to model the dynamics of a tree type robotic structure. The ABA is a numerical Newton-Euler based algorithm that solves the forward dynamics (obtaining the joint accelerations from the applied torques and forces) for a joint-link model. The main advantage of this algorithm resides in the analysis of the system link by link rather than the entire system analysis. This

feature enables the implementation of a computationally efficient code and makes the algorithm generic enough to be applied to almost any robotic structure, with minimal additional effort. Furthermore, as the basic algorithm only handles serial structures, it was modified to include the effect of the gravity, loads on the end-effector, elasticity and damping at the joints, the generalization to tree-type structures, and, finally, the inclusion of impact analysis.

TABLE OF CONTENTS

LIST OF TABLES

LIST OF FIGURES

NOMENCLATURE

c	Angular dampening coefficient [N.m.s]
e	Restitution coefficient
g	Acceleration of gravity [m/s²]
k	Angular spring constant [N.m]
m	Mass [kg]
n_c	Index of contact link
O	Order of convergence
t	Time [s]
t_{sat}	Saturation time [s]
$\mathbf{a}^{CM}$	Acceleration of the center of mass [m/s²]
$\mathbf{a}^{O}$	Acceleration of the axis origin [m/s²]
$\hat{\mathbf{a}}$	Spatial acceleration [m/s²][rad/s²]
A_r	Rotation axis vector
A_t	Translation axis vector
$\hat{\mathbf{C}}$	Centripetal component of the spatial acceleration [m/s²] [rad/s²]
$\mathbf{F}$	Force [N]
$\hat{\mathbf{F}}$	Spatial force [N][N.m]
$\hat{\mathbf{F}}^{e}$	Tip spatial force [N][N.m]

$\hat{\mathbf{g}}$	Acceleration of gravity in spatial vector [m/s²]
$\dot{\mathbf{H}}^O$	Time derivative of the angular momentum about the origin [Nm]
$\mathbf{i}$	Linear impulse [N.s]
$\mathbf{i}_c$	Linear impact impulse [N.s]
$\hat{\mathbf{i}}$	Spatial impulse [N.s][N.m.s]
$\hat{\mathbf{i}}_c$	Impact spatial impulse [N.m][N.m.s]
$\mathbf{I}^O$	Inertia tensor about the origin [kg.m²]
$\hat{\mathbf{I}}$	Spatial inertia matrix [kg][kg.m²]
$\hat{\mathbf{I}}^A$	Articulated-Body inertia matrix [kg][kg.m²]
$\mathbf{M}^O$	Moment at the origin [N.m]
$\hat{\mathbf{n}}$	Normal vector
$\hat{\mathbf{n}}$	Normal vector in spatial form
$\mathbf{r}^C$	Position of the contact point [m]
$\mathbf{r}^{CM}$	Position of the center of mass [m]
$\mathbf{r}^L$	Position of the tip of the link [m]
$\mathbf{R}$	Rotation matrix
$\mathbf{S}_\mathbf{x}$	Skew-symmetric matrix of $\mathbf{x}$
$\mathbf{v}^O$	Linear velocity at the origin [m/s]
$\hat{\mathbf{v}}$	Spatial velocity [m/s][rad/s]
$\hat{\mathbf{v}}^+$	Spatial velocity after impact [m/s][rad/s]
$\hat{\mathbf{v}}^-$	Spatial velocity before impact [m/s][rad/s]
$\hat{\mathbf{X}}$	Spatial transformation matrix

Greek Symbols

α	Angular acceleration [rad/s²]
$\hat{\boldsymbol{\beta}}$	Spatial force bias [N][N.m]
$\hat{\boldsymbol{\beta}}^{A}$	Articulated-Body force bias [N][N.m]
$\hat{\boldsymbol{\beta}}_{c}$	Contact Spatial force bias [N][N.m]
$\hat{\boldsymbol{\gamma}}$	Spatial impulse bias [N.s][N.m.s]
$\hat{\boldsymbol{\gamma}}^{A}$	Articulated-Body impulse bias [N.s][N.m.s]
θ	Joint position [rad]
θ_{sat}	Joint limit [rad]
$\theta^{initial}$	Spring initial angular position [rad]
$\dot{\theta}$	Joint angular velocity [rad/s]
$\ddot{\theta}$	Joint angular acceleration [rad/s²]
$\boldsymbol{\iota}^{O}$	Angular impulse [kg.rad/s]
τ	Applied torque [Nm]
τ^{Dyn}	Dynamic torque [Nm]
τ^{*}	Total applied torque [Nm]
$\hat{\boldsymbol{\phi}}$	Spatial axis vector
ψ	Active inverse articulated-body inertia matrix [kg^{-1}][1/(kg.m²)]
Ψ	Total active inverse articulated-body inertia matrix [kg^{-1}][1/(kg.m²)]
$\boldsymbol{\omega}$	Angular velocity [rad/s]

Acronyms

ABA	Articulated-Body Algorithm
CM	Center of Mass
CMC	Carpometacarpal
DIP	Distal Interphalangial

DoF	Degree of Freedom
EMG	Electromyogram control
IABA	Impulse Articulated-Body Algorithm
IP	Intephalangeal
MCP	Metacarpophalangeal
MIT	Massachusetts Institute of Technology
NASA	National Aeronautics Space Administration
PIP	Proximal Interphalangeal

ACKNOWLEDGMENTS

I would like to thank Dr. Afzal Suleman for giving me the opportunity to be part of his research group and to work in the field I always wanted to. I would also like to thank Dr. Suleman, in a more personal way, for the support and for giving me the experience of living by myself and in a foreign country.

I would, also, like to thank Ricardo Paiva, my best friend, for all the support, friendship and for being with me every time I needed.

A special thank for Sandra Makosinki for all the help and kindness.

I thank Ryan Nicoll, Casey Keulen, Bruno and Joana Rocha, and Kerem Karakoc for their friendship.

I wanted to thank my “sister”, Ana Castanhito Almeida, for the sincere friendship and for sharing and listening about the troubles of living all by ourselves in Victoria and in London.

The final word of gratitude goes to my parents for all the support and love they gave me through my life, even with the “saudades” from my staying in Canada.

To my parents…

Chapter 1

INTRODUCTION

Losing a limb is an extremely traumatic event that changes forever one's life, especially in the case of the hand. The human hand is our main manipulator and its shape and dexterity is one of the evolutionary characteristics that make us humans. Apart from the obvious physical impairment, the loss of a hand has a profound impact in a person's social and emotional well-being as well.

This thesis work is a first step to create a human hand prosthesis that resembles, as much as possible, the natural hand. This prosthesis will have five fingers actuated by a tendon system, driven by artificial muscles made of intelligent materials, e.g. electro active polymers.

Prostheses and Anthropomorphic Manipulators in 1991, consisted mainly in mechanic artificial hands with three to five fingers, [1]. At the same time, artificial hands, like the Standford/JPL, the Utah/MIT or the Belgrade/USC Dextrous hands, were already being commercialized. The Standford/JPL hand is composed by three fingers, in which one is a thumb-like finger, Fig. 1-1. This hand has

twelve actuated joints, three for each finger and, because the fingers are actuated by a tendon system each one of them must be actuated by a set of four servomotors.

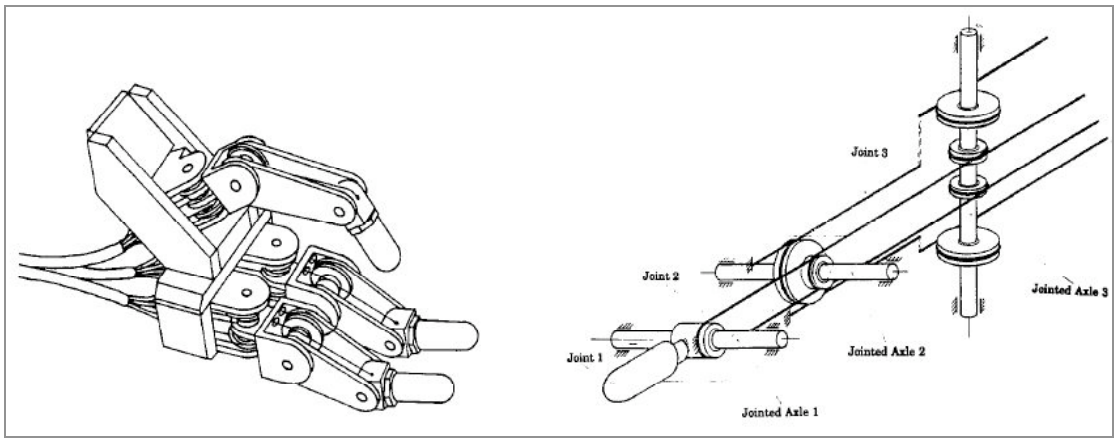

Fig. 1-1 Standford/JPL hand, [1].

The Utah/MIT hand has four 4-DOF fingers (one of them is a thumb) actuated by 32 independent tendons and pneumatic cylinders: 16 to close the hand and 16 to open, Fig. 1-2. This hand, although more anthropomorphic, has two disadvantages: it has a high number of actuators, and, because of the rigid tendons, the ulnar motion (the spreading of the fingers) affects the fingers flexion/extension movements.

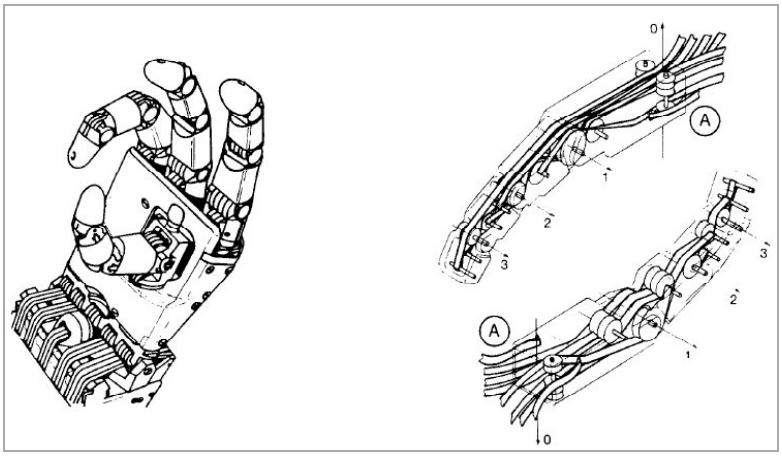

Fig. 1-2 Utah/MIT hand, [1].

The Belgrade/USC hand has five fingers, with four servomotors: one for each pair of fingers and two for the thumb, Fig. 1-3. This hand has a very limited motion, because only two servomotors actuate the four fingers and, consequently, the hand can only grasp objects, [1].

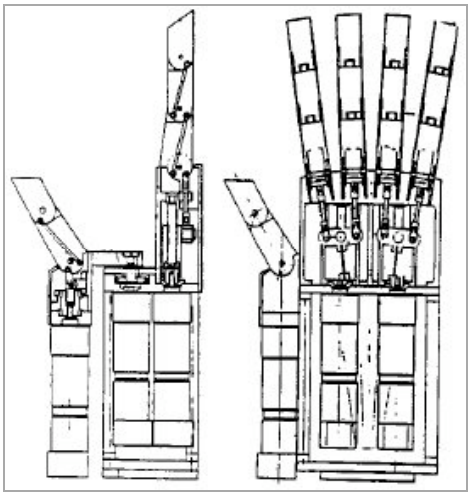

Fig. 1-3 Belgrade/USC hand, [1].

The authors in [1] also propose another type of hand, a three-finger manipulator with 3-DOF in each finger, Fig. 1-4.

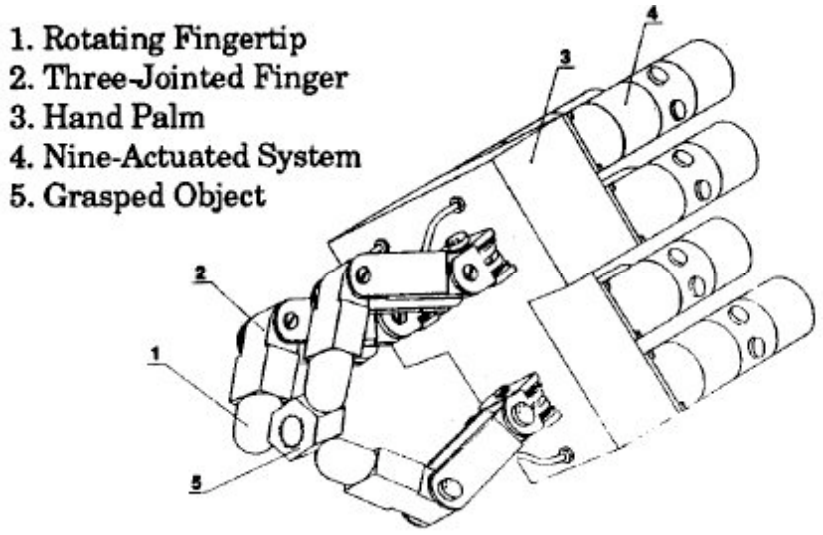

Fig. 1-4 Proposed hand, [1].

In reference [2], the authors introduce an anthropomorphic hand with five fingers and one thumb, actuated by pneumatic artificial muscles consisting in rubber sleeves that shorten their length when inflated, Fig. 1-5.

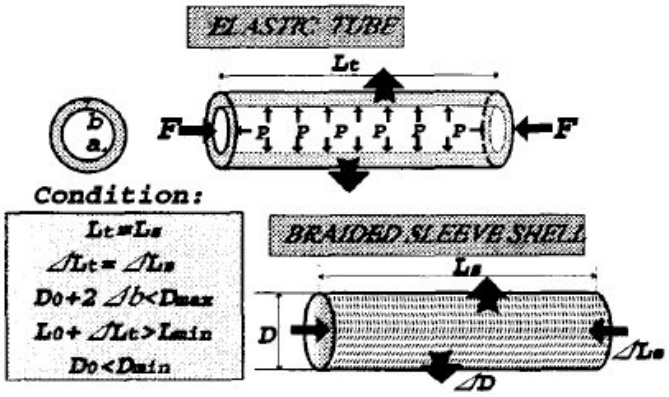

Fig. 1-5 Pneumatic artificial muscle, [2].

These muscles are placed on a skeletal framework, similar to the human hand bone structure in approximately the same arrangement of the natural muscles. Although the final artificial hand has less muscles than the human counterpart, it can grasp, hook grip and finger stretch, Fig. 1-6.

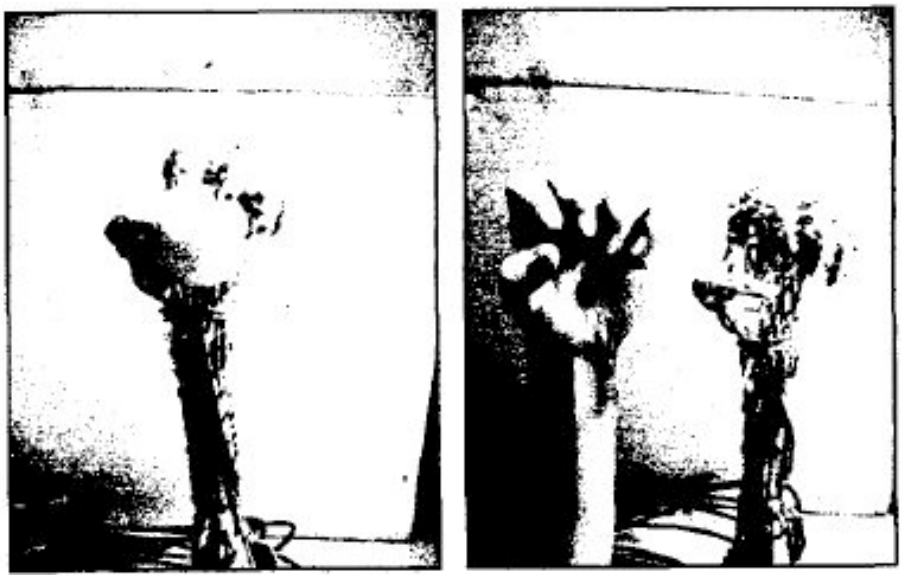

Fig. 1-6 Skeletal pneumatic artificial hand, [2].

The main disadvantages of this hand are its bulkiness (compared to the natural one) and the side apparatus needed for the hand to function: electromagnetic valves and an air compressor.

The Graspar hand, [3], has two 3-DOF fingers and one 2-DOF thumb and is mainly a grasping hand. This hand is actuated by electric servomotors and a tendon system, Fig. 1-7.

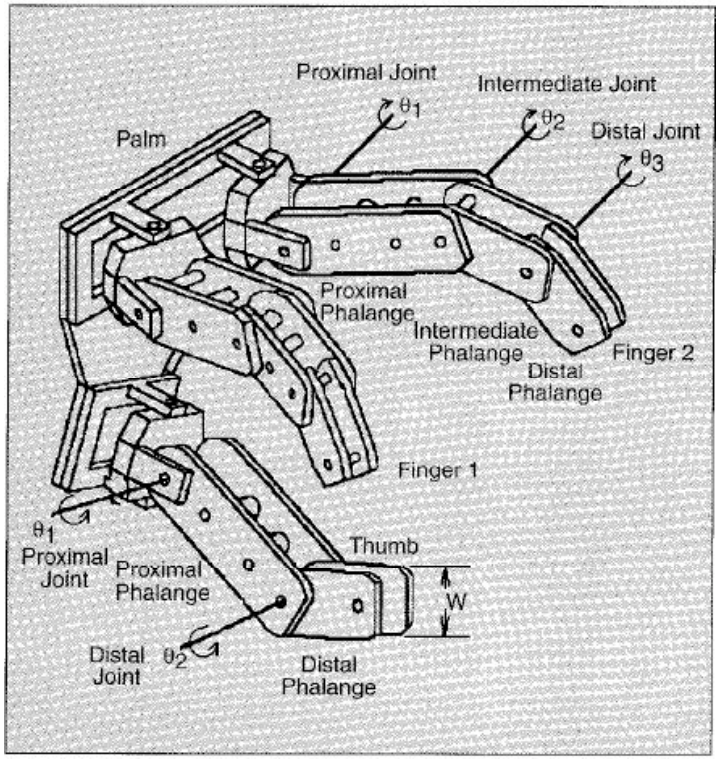

Fig. 1-7 Graspar hand, [3].

The Robonaut, is a NASA's space robot, [4]. This robot is a one legged anthropomorphic robot made to resist the harsh conditions of space and have at least the same manipulation capabilities of an astronaut, Fig. 1-8.

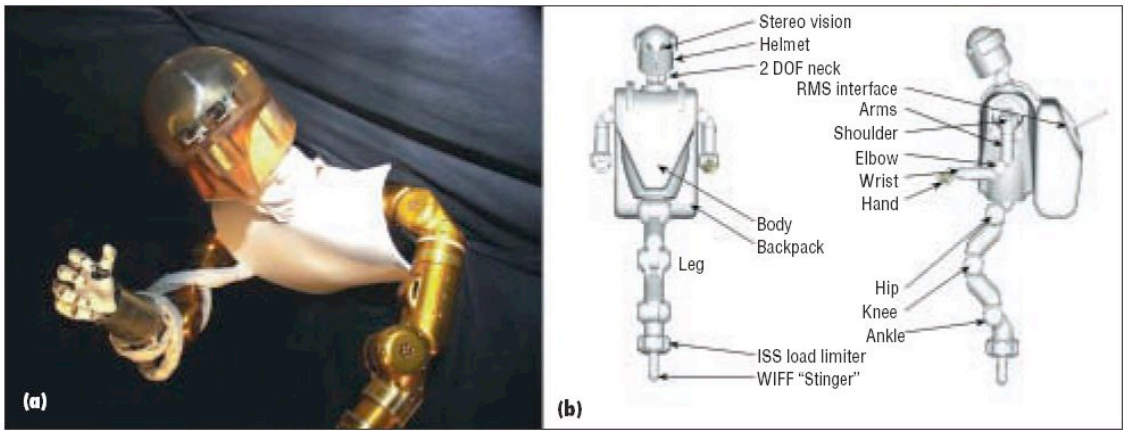

Fig. 1-8 NASA's Robonaut, [4].

The hand has 14 actuated joints and 5 fingers (one of them a thumb), and is actuated using a tendon system and 14 electric motors, Fig. 1-9.

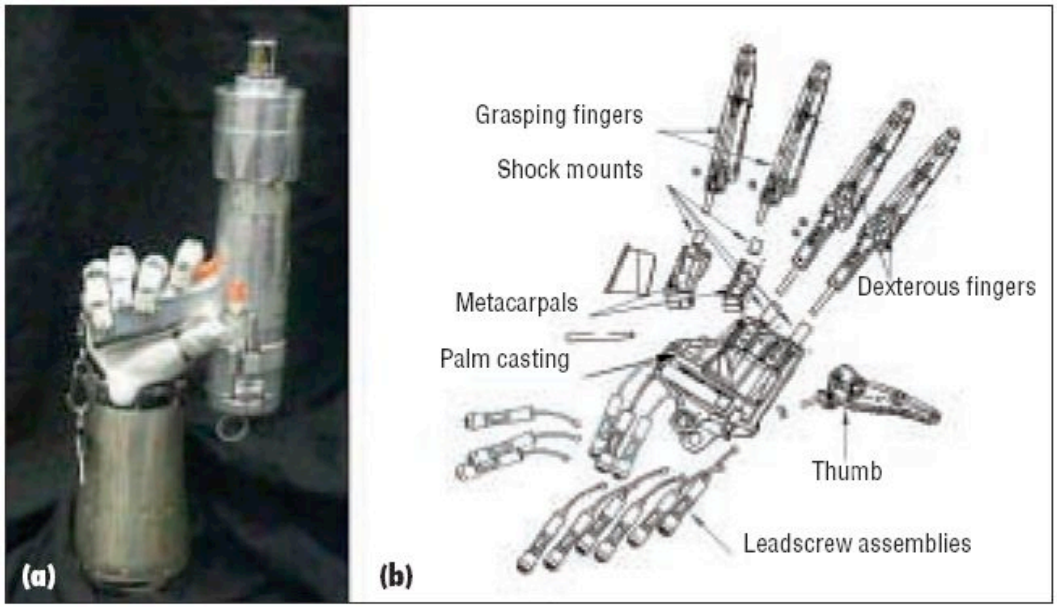

Fig. 1-9 Robonaut robotic hand, [4].

This is one of the most advanced artificial hands until today, is capable of grasping and manipulating objects, Fig. 1-9(a). The hand, along with the rest of the robot, is teleoperated.

The Oxford and Manus prostheses are 3 finger artificial hands, driven by electrical motors and a tendon system. The main difference between them is the way the tendon system is constructed, Fig. 1-10, [5].

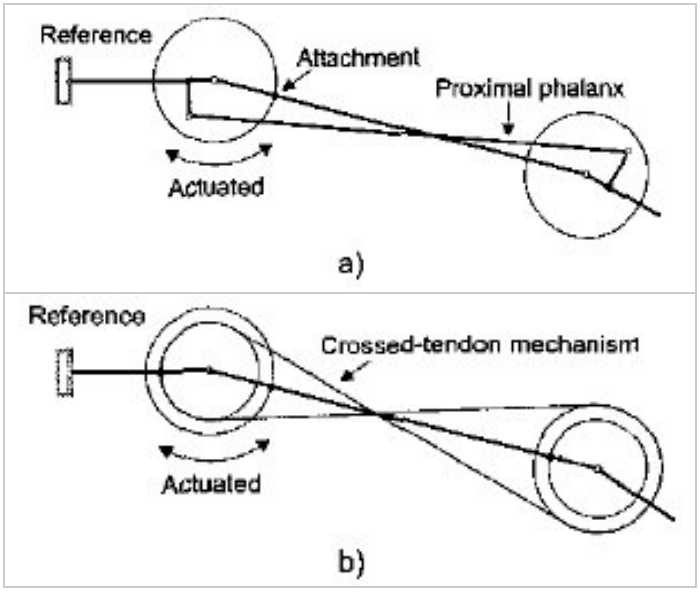

Fig. 1-10 Oxford and Manus hand tendon system, [5].

The fingers in both hands are 2-DOF, but the Oxford hand, Fig. 1-10(a), uses rigid links as tendons, unlike the Manus hand, Fig. 1-10(b), that uses a crossed-tendon mechanism with steel wires.

To become more anthropomorphic, both have two passive fingers, rigid in the case of the Oxford hand, or manually deformable in the case of the Manus hand.

Alongside with the mechanical and structural parts, the control system also has an important part in the design of the artificial hand. Nowadays, the more advanced prosthesis control system is the Electromyogram (EMG) control. With the EMG, an amputee can control the prosthesis directly with his brain, like one would control the natural hand, [6].

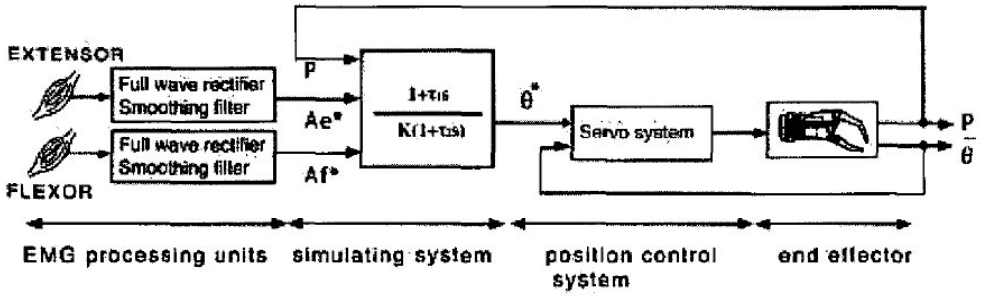

Fig. 1-11 EMG control block diagram, [6].

This type of prosthesis control, Fig. 1-11, however imposes limitations on the prosthesis itself. Because of its complex nature, EMG controlled hands only have a small number of actuated joints, thus limiting its capabilities. One example of an EMG controlled hand can be seen in Fig. 1-12.

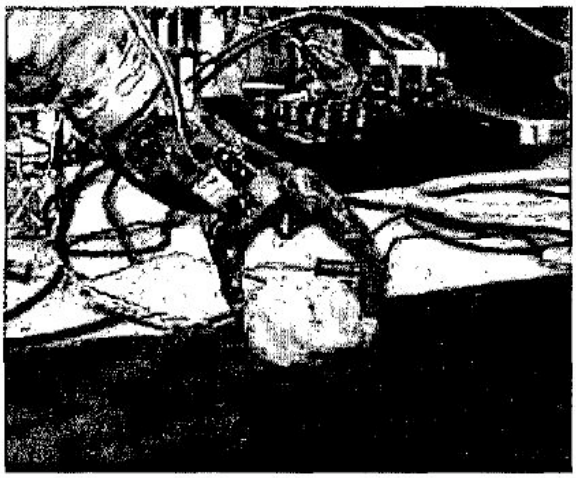

Fig. 1-12 EMG controlled hand, [6].

A more recent artificial anthropomorphic hand project is the Anatomically Correct Testbed hand (ACT hand), [7] and [8]. This hand was designed to study the natural hand movements and dynamics, and not for an application in robotics or prostheses. Nevertheless, this hand is important, since it tries to mimic the natural hand by constructing a similar muscular-skeletal structure. This hand uses servomotors and a tendon system as actuator. Both bone and tendon structures are made to be similar to the human hand, Fig. 1-13.

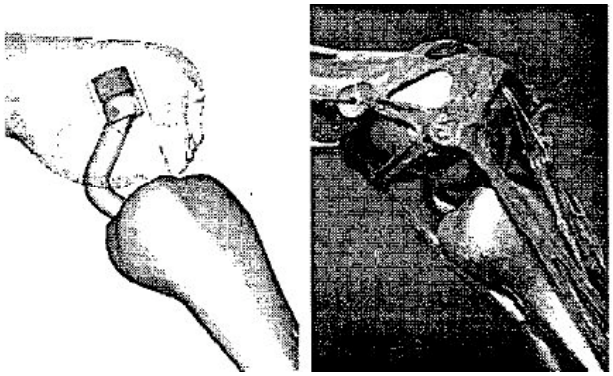

Fig. 1-13 Finger joint of the ACT hand, [7].

1.1. Thesis Objective

The main objective of this thesis is the development of a model of the human hand to help the development of the prosthesis prototype. The model will be used to determine the dynamic behavior of the hand and to estimate the characteristics of the actuators and control system. Within this main objective, the thesis has two sub-objectives:

1. Implement the simple serial structure Articulated-body algorithm;
2. Adapt the Articulated-Body Algorithm for the specific characteristics of the human hand: tree structure, elasticity and dampening on the joints, and joint limits;
3. Adapt the algorithm to handle impacts between the structure and its environment.

1.2. Thesis Outline

Chapter 2 will present the anatomy and physiology of the human hand. The first part will focus on the bone structure, detailing the functions and characteristics of the bones. Then the muscular system will be discussed, starting with the action and location of each muscle, along with some remarks about the way they function, and finishing with the physiology of the skeletal muscles.

In Chapter 3 the Articulated-Body algorithm will be explained in detail. The chapter will begin with the demonstration of the algorithm from the Newton-Euler equations. Then, it will be introduced the spatial notation, along with its

simplifications. The next step will be finding the recursive equations that calculate the articulated-body inertias and force bias. The presentation of the algorithm will continue with the adaptation of the algorithm to the more generic case of tree-structures and to the existence of elasticity and dampening on the joints. In the final section it will be explained how the algorithm was adapted to handle joint limits.

In Chapter 4 the Impulse Articulated-body algorithm and the impact impulse equation will be developed. The impulse articulated-body algorithm is an adaptation of the articulated-body algorithm that handles, exclusively, impact occurrences. With the algorithm developed, the next part will be dedicated to the demonstration of the impact impulse equations for single and multiple impacts. The last part will focus on prolonged contact between the structure and the environment.

In Chapter 5 the results taken from the algorithm will be presented. The tests done consist of a simple pendulum, a six-link serial structure, an inverted double pendulum, an eleven-link tree-structure and the human hand. The first two tests run the ABA on its simpler form, serial structure without any external actuation. The third test keeps the serial structure and adds the impact simulation to the ABA. The fourth test runs the ABA adapted to tree structures with and without applied torques, and the final test, the human hand, runs the ABA with joint limits and elasticity and dampening on the joints.

The conclusions are made in Chapter 6 as well suggestions for future work and improvements to the algorithm.

Chapter 2
THE HUMAN HAND

2.1. The Human Hand

The human hand is the most complex muscular-skeletal system in the human body. Apart from being our main manipulator, the hand, is also responsible for the majority of input information from our touch sense. The hand can be divided into three sub-systems: the skeletal system, the muscular system, and the dermo-neurological system, [9]. This section will, exclusively, detail the first two.

2.1.1. Skeletal system

The bones are the structural basis of the hand: they support the muscles and tendons, and give form to the hand itself. A normal human hand has 26 bones divided into three categories: the carpal bones, the metacarpal bones and the phalanxes; and 20 joints divided into four categories: the wrist joint, the

carpometacarpal joints, the metacarpophalangeal joint, and the digital joints, [9] and [10].

2.1.1.1. The Bones

The carpals are located on the lower part of the hand, Fig. 2-1. Although independent from each other, the Carpal bones are fixed and act as a solid block, making a progressive transition between the two wrist bones and the five Metacarpal bones.

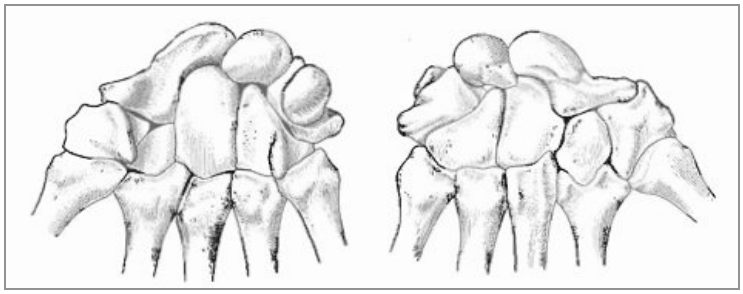

Fig. 2-1 The Carpal Bones, [10].

The five Metacarpal bones give form to the palm and are the largest bones in the hand, Fig. 2-2.

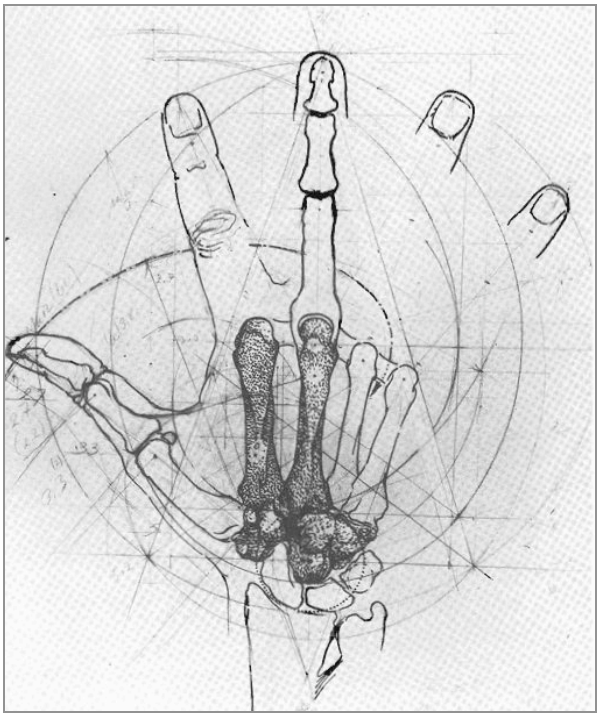

Fig. 2-2 The Metacarpal bones, [10].

Only the first and the fifth metacarpals (the leftmost and the rightmost, respectively) have active movements, whereas the second metacarpal has a passive movement and the last two are fixed along with the Carpal bones.

The Phalanges are the bones of the fingers and are denominated, from the base to the tip: proximal, middle and distal (with the exception of the thumb that only has the proximal and distal phalanxes).

2.1.1.2. The joints

The wrist joint has two degrees of freedom (DoF): lateral movement of the hand, also called abduction/adduction (Fig. 2-3A and B, respectively), and extension/flexion.

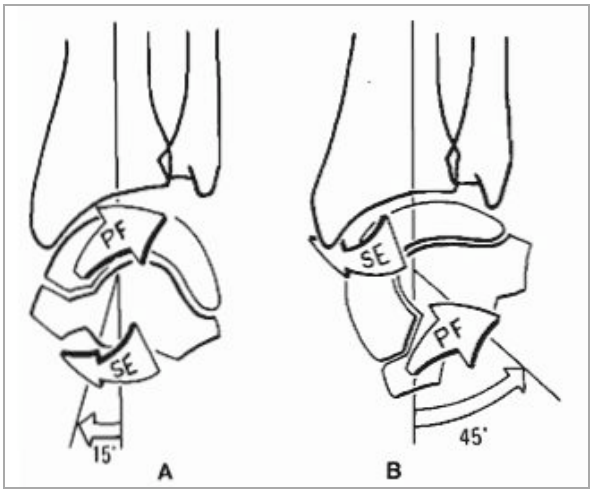

Fig. 2-3 The wrist joint, [10].

One characteristic of this joint is the coupling between the DoFs when the hand flexes or extends.

The carpometacarpal (CMC) joints are mainly fixed joints except for the first and fifth joints. The first joint has two degrees of freedom: rotation around an axis formed by the second metacarpal bone, and flexion/extension. Both movements are depicted in Fig. 2-4.

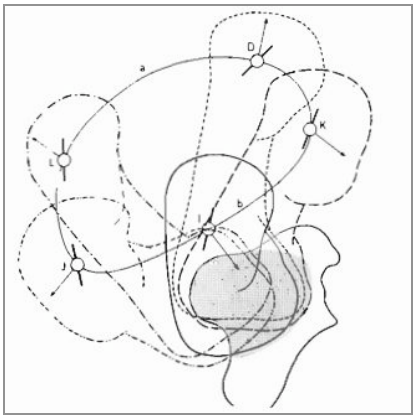

Fig. 2-4 Fist carpometacarpal joint, [10].

The fifth metacarpal joint has only a small rotation movement around an axis formed by the fourth metacarpal bone.

The metacarpophalangeal (MCP) joints (also called knuckles) are the first joints of the finger and all have two degrees of freedom (abduction/adduction and flexion/extension), with the sole exception of the thumb that has only one (flexion/extension). There is a small particularity in the second to fifth MPC joints, the extent of the abduction/adduction decreases with the increase of flexion.

The digital joints, the proximal joint (PIP) and the distal interphalangeal joint (DIP), are the main joint of the finger and only have flexion/extension movements.

2.1.2. Muscular system

All the hand muscles are skeletal muscles and can be divided into two categories: the extrinsic muscle and the intrinsic muscles.

The extrinsic muscles are located on the wrist and forearm, Fig. 2-5 and Fig. 2-6, and are responsible for the wider movements of the fingers. They are, also, the muscles with more strength and are the last to be actuated. The functions and actuation characteristic of these muscles are detailed on Table 2-I, [1], [11] and [10].

Table 2-I Extrinsic Muscles

Name	***Action***	***Active Joints***
Extensor Digitorum	Extend the four fingers simultaneously	Both IP joints
Extensor Indicis	Extend the index finger	Distal IP joint
Extensor Digiti Minimi	Extend the little finger	Distal IP joint
Extensor Carpi Radialis	Extend and abducts the hand	Wrist joint
Extensor Carpi Ulmaris	Extend and adducts the hand	Wrist joint
Palmaris Longus	Extend the hand	Wrist joint
Extensor Pollicis Longus	Extend the thumb	IP joint of the thumb
Extensor Pollicis Brevis	Extend the thumb	MCP joint of the thumb
Flexor Digitorum Profundus	Flex the four fingers simultaneously	Distal IP joints
Flexor Digitorum Superficialis	Flex the four fingers simultaneously	Proximal IP joints
Flexor Carpi Radialis	Flex and abducts the hand	Wrist joint
Flexor Carpi Ulnaris	Flex and adducts the hand	Wrist joint
Flexor Pollicis Longus	Flex the thumb	IP joint of the thumb
Abductor Pollicis Longus	Abduct and extend the thumb	CMC joint of the thumb

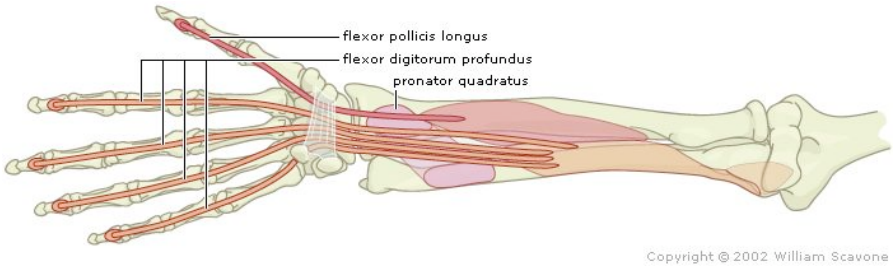

Fig. 2-5 Extrinsic flexor muscles, [9].

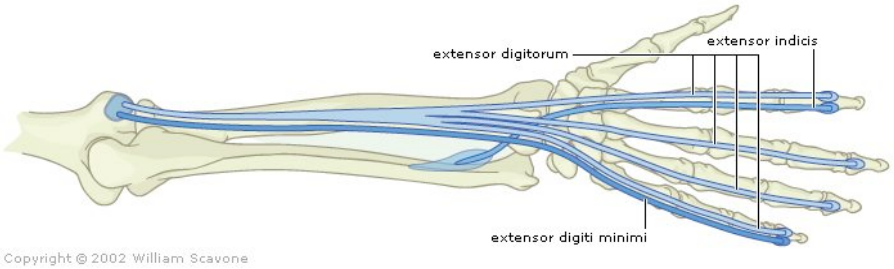

Fig. 2-6 Extrinsic extensor muscles, [9].

The intrinsic muscles are located on the hand itself and are responsible for small amplitude and strength movements. They are also used to fine-tune the movements done by the extrinsic muscles.

Table 2-II Intrinsic Muscles

Name	***Action***	***Active Joints***
Palmar Interossei	Adduct the index, ring, and little finger toward the axial line through the third digit. Assist in flexion of MCP joints, and extension of IP joints of the three fingers	MCP joints of the index, ring and little fingers
Lumbricals	Extend the IP joints and simultaneously flex the MCP joints of the second through fifth digits. The lumbicals also extend the IP joints when the MCP joints are extended	MCP and IP of the four fingers
Opponens Digiti Minimi	Opposes the little finger to the thumb.	CMC joint of the little finger
Abductor Digiti Minimi	Abduct the little finger	MCP joint of the little finger
Flexor Digiti Minimi	Flexes the little finger and helps the Opponens Digiti Minimi	MCP joint of the little finger
Adductor Pollicis	Adduct the metacarp of the thumb and flex the thumb	CMC and MCP joints of the thumb
Flexor Pollicis Brevis	Flex the thumb	MCP joint of the thumb
Abductor Pollicis Brevis	Abducts and extends the thumb	MCP joint of the thumb
Opponens Pollicis	Opposes the thumb to the little finger.	CMC joint of the thumb
Dorsal Interossei	Abdutcs the index, ring and middle finger, adducts the middle finger and assists in flexion of MCP joints, and extension of IP joints of the three fingers	MCP joints of the index, ring and middle fingers
Abductor Digiti Minimi	Abduct the little finger	MCP joint of the little finger

There are some remarks on the way the muscles actuate on the hand. The first is the intricate interaction between the Extensor Digitorum, the Dorsal and Palmar Interossei, and the lumbricals, called the Extensor Apparatus, Fig. 2-7, [9] and [10].

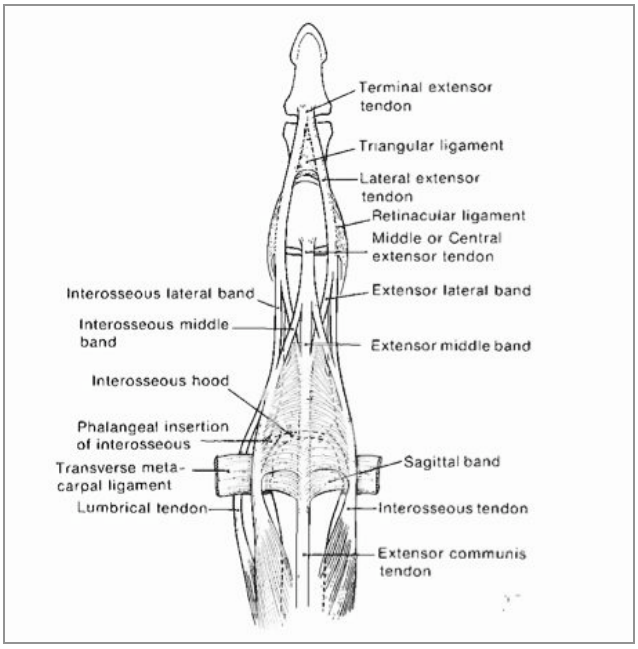

Fig. 2-7 Extensor Apparatus, [10].

The way these muscles interact and act on the fingers is very complex: the Extensor Digitorum has the sole function of extending the fingers, but depending on the state of the interossei muscle, the Extensor Digitorum can actuate only the distal IP joint or only the proximal IP joints.

As the fingers start to extend, the interossei hood (a ligament structure on top of the proximal phalanges connecting the opposing intesossei) moves in the direction of the MCP joint shifting the action of the lumbricals from extension of the MCP joints to flexion of the same joints, Fig. 2-8, [10].

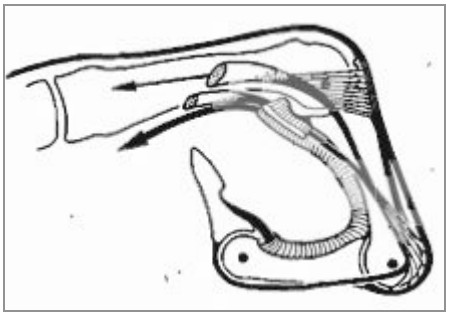

Fig. 2-8 Lumbricals acting as flexors, [10].

Since the Interossei are directly connected to the tendon of the Extensor Digitorum, rather than to the bone, they assist also in the extension of the fingers.

Another remark is how the muscles are actuated. When the hand grabs and pulls something, the first bones to be actuated are the intrinsic muscles. If the brain perceives that the muscles are not producing sufficient movement, the extrinsic muscles start to be actuated in small groups of fibers, depending on the force needed. Since the extrinsic muscles are now handling the force, the intrinsic are used to fine-tune the movements of the fingers.

Finally, looking to Table 2-I and Table 2-II, one can see that the muscular system is heavily coupled, because some muscles actuate several joints, simultaneously, and some joints are actuated by several muscles.

Chapter 3

ARTICULATED-BODY ALGORITHM

The Articulated-Body Algorithm (ABA) was developed by R. Featherstone [12] and currently is the fastest serial processing algorithm (for a series of rigid-bodies inter-connected by joints) when compared with other leading algorithms: the Divide-and-Conquer Algorithm (DCA), [13] and [14], and the Hybrid Direct/Iterative Algorithm (HDIA), [15], Table 3-I. The main advantages of the ABA are the low computational cost, the ABA is an *O(n)* algorithm (where *n* is the number of link of a robotic structure), and the algorithm relative versatility, the ABA has been adapted to handle different types of structures and even parallel computation, [15],[16] and [17].

Table 3-I Fastest Algorithms as function of number of bodies (N_B) and number of processors (N_P), [13].

	$N_B = 10$	$N_B = 100$	$N_B = 1000$
$N_P = 1$	ABA	ABA	ABA
$N_P = 10$	HDIA	HDIA	HDIA
$N_P = 100$	—	HDIA/DCA	HDIA/DCA
$N_P = 1000$	—	—	DCA

3.1. Serial Articulated-Body Algorithm

The ABA is based on the Newton-Euler dynamics equations. The original algorithm is limited to the simulation of serial structures, which is a chain of inter-connected rigid bodies with a single base (fixed or movable) and a single end-effector, Fig. 3-1.

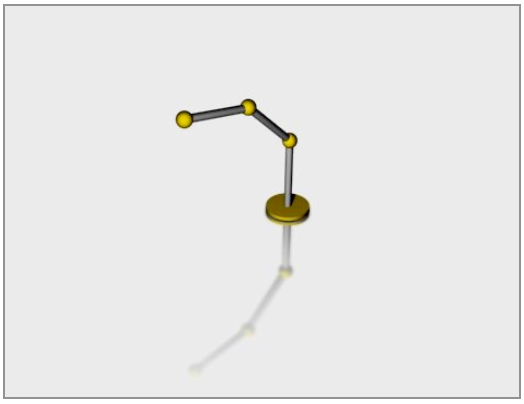

Fig. 3-1 Serial Structure

3.1.1. Newton-Euler Equations

The corner stone of the ABA is that any articulated structure, in a joint-link model, can be analyzed link by link, instead of the system as a whole, which has immediate advantage of avoiding the solution of an $n \times n$ system of equations. So the first step is choosing a random link from the serial structure to be analyzed and assign two reference frames (one at the base of the link, i-1, and one at the top of the link, i), Fig. 3-2.

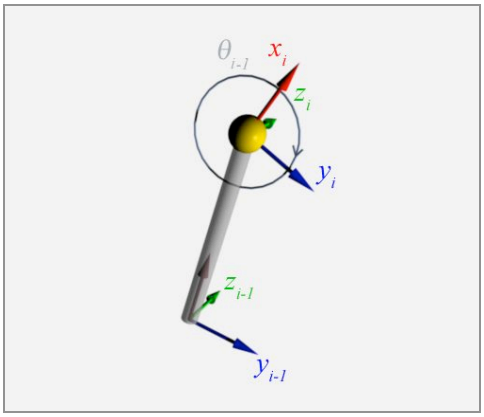

Fig. 3-2 Link with reference frames.

Note that the joint associated with the link is at the top of the link and the referential moves with the joint. In this configuration the base reference frame is fixed relatively to the link.

With the reference frames defined, one can consider a general kinematic state with linear and angular velocities and accelerations, Fig. 3-3.

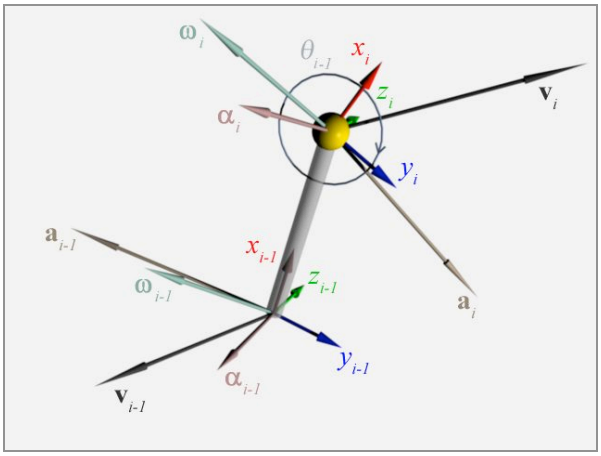

Fig. 3-3 Link in a General kinematic state.

Using the Newton-Euler equations, a relation can be established between the linear and angular velocities of both reference frames, (3.1) and (3.2), respectively:

$$\mathbf{v}_i^O = \mathbf{R}_{i-1}^i \mathbf{v}_{i-1}^O + \mathbf{R}_{i-1}^i \left(\boldsymbol{\omega}_{i-1} \times \mathbf{r}_{i-1}^L \right) \tag{3.1}$$

$$\boldsymbol{\omega}_i = \mathbf{R}_{i-1}^i \boldsymbol{\omega}_{i-1} + \dot{\boldsymbol{\theta}}_{i-1} \tag{3.2}$$

where $\mathbf{v}^O$ is the linear velocity of the reference frame origin, $\boldsymbol{\omega}$ is the angular velocity of the reference frame, $\dot{\boldsymbol{\theta}}$ is the joint angular velocity[1], $\mathbf{r}_{i-1}^L$ is the position of the *i*-frame relatively to the *(i*-1*)*-frame (a vector with norm equal to the length, *L*, of the link), and $\mathbf{R}_{i-1}^i$ is the rotation matrix form the *(i*-1*)*-frame to the *i*-frame.

For the linear and angular acceleration, one has (3.3) and (3.4), respectively:

$$\mathbf{a}_i^O = \mathbf{R}_{i-1}^i \mathbf{a}_{i-1}^O + \mathbf{R}_{i-1}^i \left(\boldsymbol{\alpha}_{i-1} \times \mathbf{r}_{i-1}^L \right) + \mathbf{R}_{i-1}^i \left(\boldsymbol{\omega}_{i-1} \times \left(\boldsymbol{\omega}_{i-1} \times \mathbf{r}_{i-1}^L \right) \right) \tag{3.3}$$

$$\boldsymbol{\alpha}_i = \mathbf{R}_{i-1}^i \boldsymbol{\alpha}_{i-1} + \ddot{\boldsymbol{\theta}}_{i-1} + \boldsymbol{\omega}_i \times \dot{\boldsymbol{\theta}}_{i-1} \tag{3.4}$$

where $\mathbf{a}^O$ is the linear acceleration of the reference frame origin, $\boldsymbol{\alpha}_{i-1}$ is the angular acceleration of the reference frame, and $\ddot{\boldsymbol{\theta}}$ is the joint angular acceleration.

Considering, now, a general dynamic state with forces and moments, Fig. 3-4,

[1] Note that the subscript index refers to the link index, which is the same as the base reference frame. The joint velocity is measured on the top reference frame.

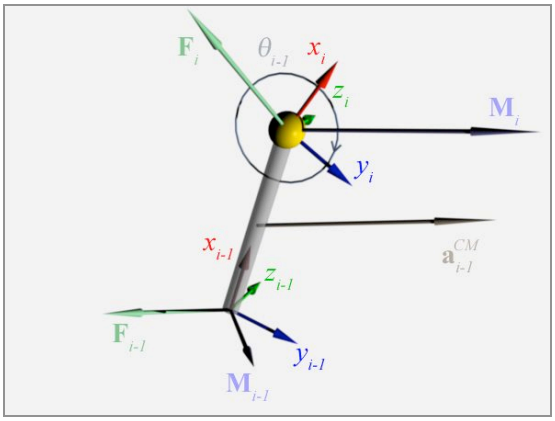

Fig. 3-4 Link in a general dynamic state.

one can define the balance of forces, (3.5), and the balance of moments, (3.6):

$$\sum \mathbf{F} = \mathbf{F}_{i-1} + \mathbf{R}_i^{i-1}\mathbf{F}_i = m_i \mathbf{a}_{i-1}^{CM} \tag{3.5}$$

$$\sum \mathbf{M}^O = \mathbf{M}_{i-1}^O + \mathbf{R}_i^{i-1}\mathbf{M}_i^O + \mathbf{r}_{i-i}^L \times \left(\mathbf{R}_i^{i-1}\mathbf{F}\right)_i = \dot{\mathbf{H}}_{i-i}^O \tag{3.6}$$

where $\mathbf{F}$ is an external force, m is the link mass, and $\mathbf{M}^O$ is an external moment. $\mathbf{a}_{i-1}^{CM}$ is the acceleration of the Center of Mass (CM) relatively to the *(i-1)*-frame, (3.7), and $\dot{\mathbf{H}}_{i-i}^O$ is the time derivative of the angular momentum, given in (3.8).

$$\mathbf{a}_i^{CM} = \mathbf{a}_{i-1}^O + \boldsymbol{\alpha}_{i-1} \times \mathbf{r}_{i-1}^{CM} + \boldsymbol{\omega}_{i-1} \times \left(\boldsymbol{\omega}_{i-1} \times \mathbf{r}_{i-1}^{CM}\right) \tag{3.7}$$

$$\dot{\mathbf{H}}_{i-1}^O = \mathbf{I}_{i-1}^O \alpha_{i-1} + \mathbf{r}_{i-1}^{CM} \times m_{i-1}\mathbf{a}_{i-1}^O + \omega_{i-1} \times \left(\mathbf{I}_{i-1}^O \omega_{i-1}\right) \tag{3.8}$$

$\mathbf{r}_{i-1}^{CM}$ is the position of the CM relatively to the *(i-1)*-frame and $\mathbf{I}_{i-1}^O$ is the inertia tensor at the origin of the *(i-1)*-frame.

3.1.2. Spatial Notation

Featherstone introduced a new notation, called the spatial vectors and matrices, to simplify the Newton-Euler equations, (3.1) to (3.8), [12].

The spatial notation consists in assembling the linear and angular parts of a quantity into a single vector or matrix, e.g. the spatial velocity[2] is given by (3.9):

$$\hat{\mathbf{v}}_i = \begin{bmatrix} \mathbf{v}_i^O \\ \boldsymbol{\omega}_i \end{bmatrix} \tag{3.9}$$

The spatial acceleration and force are defined by (3.10) and (3.11), respectively:

$$\hat{\mathbf{a}}_i = \begin{bmatrix} \mathbf{a}_i^O \\ \boldsymbol{\alpha}_i \end{bmatrix} \tag{3.10}$$

$$\hat{\mathbf{F}}_i = \begin{bmatrix} \mathbf{F}_i \\ \mathbf{M}_i^O \end{bmatrix} \tag{3.11}$$

With the new notation (3.1) to (3.8) become (3.12) to (3.14):

$$\hat{\mathbf{v}}_i = \hat{\mathbf{X}}_{i-1}^i \hat{\mathbf{v}}_{i-1} + \hat{\boldsymbol{\phi}}_{i-1} \dot{\theta}_{i-1} \tag{3.12}$$

$$\hat{\mathbf{a}}_i = \hat{\mathbf{X}}_{i-1}^i \hat{\mathbf{a}}_{i-1} + \hat{\boldsymbol{\phi}}_{i-1} \ddot{\theta}_{i-1} + \hat{\mathbf{C}}_i \tag{3.13}$$

$$\hat{\mathbf{F}}_{i-1} - \left(\hat{\mathbf{X}}_{i-1}^i\right)^T \hat{\mathbf{F}}_i = \hat{\mathbf{I}}_{i-1} \hat{\mathbf{a}}_{i-1} + \hat{\boldsymbol{\beta}}_i \tag{3.14}$$

[2] The definition of the spatial vectors given by [12] has the angular part first and then the linear part, but, for simplicity, they were switched in this work.

where $\hat{\mathbf{X}}_{i-1}^{i}$ is the transformation spatial matrix from the *(i-1)*-frame to the *i*-frame, (3.15):

$$\hat{\mathbf{X}}_{i-1}^{i} = \begin{bmatrix} \mathbf{R}_{i-1}^{i} & -\mathbf{R}_{i-1}^{i}\mathbf{S}_{\mathbf{r}_{i-1}^{L}} \\ \mathbf{0} & \mathbf{R}_{i-1}^{i} \end{bmatrix} \tag{3.15}$$

being $\mathbf{S}_{\mathbf{r}_{i-1}^{L}}$ the skew-symmetric matrix of $\mathbf{r}_{i-1}^{L}$.

$\hat{\boldsymbol{\phi}}$ is the spatial axis vector. This vector describes the orientation of the joint axis and the type: rotation, A_r, or translation, A_t, (3.16):

$$\hat{\boldsymbol{\phi}} = \begin{bmatrix} A_t \\ A_r \end{bmatrix} \tag{3.16}$$

$\hat{\mathbf{C}}$ contains the centripetal components of the accelerations (3.17):

$$\hat{\mathbf{C}}_i = \begin{bmatrix} \mathbf{R}_{i-1}^{i}\left(\boldsymbol{\omega}_{i-1} \times \left(\boldsymbol{\omega}_{i-1} \times \mathbf{r}_{i-1}^{L}\right)\right) \\ \boldsymbol{\omega}_i \times \boldsymbol{\phi}_i^{T}\dot{\theta}_i \end{bmatrix} \tag{3.17}$$

$\hat{\mathbf{I}}$ is the spatial inertia matrix, (3.18):

$$\hat{\mathbf{I}}_i = \begin{bmatrix} m_i\mathbf{1} & -m_i\mathbf{S}_{\mathbf{r}_i^{CM}} \\ m_i\mathbf{S}_{\mathbf{r}_i^{CM}} & \mathbf{I}_i^{O} \end{bmatrix} \tag{3.18}$$

and $\hat{\boldsymbol{\beta}}$ is the spatial force bias, (3.19):

$$\hat{\boldsymbol{\beta}}_i = \begin{bmatrix} \boldsymbol{\omega}_i \times \left(\boldsymbol{\omega}_i \times \mathbf{r}_i^{CM} \right) \\ \boldsymbol{\omega}_i \times \left(\mathbf{I}_i^O \boldsymbol{\omega}_i \right) \end{bmatrix} \tag{3.19}$$

The spatial force bias results from the moving the balance of forces from the CM to the origin of the base reference frame of the link.

3.1.3. Articulated-Body Quantities

Although simplifying the Newton-Euler equations, the spatial notation, by itself, does not the problem of the fully coupled system of equation. To decouple the system, one must transform the system in such way that the system matrix becomes diagonal, [18].

The last link of the structure (the end-effector) is the simplest case: there is no upper link and, consequently, the $\left(\hat{\mathbf{X}}_{i-1}^{i} \right)^T \hat{\mathbf{F}}_i$ term from (3.14) vanishes. So starting at the end-effector, one can define the following quantities, (3.20):

$$\hat{\mathbf{F}}_n = \hat{\mathbf{I}}_n^A \hat{\mathbf{a}}_n + \hat{\boldsymbol{\beta}}_n^A \tag{3.20}$$

where $\hat{\mathbf{I}}_n^A$ and $\hat{\boldsymbol{\beta}}_n^A$ are the articulated-body inertia and articulated-body force bias. The articulated-body quantities include not only the dynamic quantities of the link in study, but also the dynamic influences of the upper links of the structure

(were "upper" means from the link to the end-effector). Because (3.20) is the last link, the articulated-body quantities are equal to their spatial counterparts.

The effect of the movement of the link connected to the end-effector is introduced, into (3.20), through the spatial acceleration. So introducing (3.13) in (3.20) results in (3.21):

$$\hat{\mathbf{F}}_n = \hat{\mathbf{I}}_n^A \left(\hat{\mathbf{X}}_{n-1}^n \mathbf{a}_{n-1} + \hat{\boldsymbol{\phi}}_{n-1} \ddot{\theta}_{n-1} + \hat{\mathbf{C}}_n \right) + \hat{\boldsymbol{\beta}}_n^A \tag{3.21}$$

Since the joint acceleration is unknown, one must remove it from (3.21) in order to proceed. Pre-multiplying (3.21) with $\hat{\boldsymbol{\phi}}_{n-1}^T$ and knowing that $\hat{\boldsymbol{\phi}}_{n-1}^T \hat{\mathbf{F}}_n$ is the torque applied to the joint, results in (3.22):

$$\tau_{n-1} = \hat{\boldsymbol{\phi}}_{n-1}^T \hat{\mathbf{I}}_n^A \hat{\boldsymbol{\phi}}_{n-1} \ddot{\theta}_{n-1} + \hat{\boldsymbol{\phi}}_{n-1}^T \hat{\mathbf{I}}_n^A \left(\hat{\mathbf{X}}_{n-1}^n \hat{\mathbf{a}}_{n-1} + \hat{\mathbf{C}}_n \right) + \hat{\boldsymbol{\phi}}_{n-1}^T \hat{\boldsymbol{\beta}}_n^A \tag{3.22}$$

where τ is the applied torque to the joint.

Solving (3.22) to find the joint acceleration, one gets (3.23):

$$\ddot{\theta}_{n-1} = \left(\hat{\boldsymbol{\phi}}_{n-1}^T \hat{\mathbf{I}}_n^A \hat{\boldsymbol{\phi}}_{n-1} \right)^{-1} \left(\tau_{n-1} - \hat{\boldsymbol{\phi}}_{n-1}^T \hat{\boldsymbol{\beta}}_n^A - \hat{\boldsymbol{\phi}}_{n-1}^T \hat{\mathbf{I}}_n^A \left(\hat{\mathbf{X}}_{n-1}^n \hat{\mathbf{a}}_{n-1} + \hat{\mathbf{C}}_n \right) \right) \tag{3.23}$$

With the expression for the joint acceleration, one can replace (3.23) back into, (3.24):

$$\hat{\mathbf{F}}_n = \left(\hat{\mathbf{I}}_n^A - \hat{\mathbf{I}}_n^A \hat{\boldsymbol{\phi}}_{n-1} \left(\hat{\boldsymbol{\phi}}_{n-1}^T \hat{\mathbf{I}}_n^A \hat{\boldsymbol{\phi}}_{n-1} \right)^{-1} \hat{\boldsymbol{\phi}}_{n-1}^T \hat{\mathbf{I}}_n^A \right) \left(\hat{\mathbf{X}}_{n-1}^n \hat{\mathbf{a}}_{n-1} + \hat{\mathbf{C}}_n \right) + \hat{\mathbf{I}}_n^A \hat{\boldsymbol{\phi}}_{n-1} \left(\hat{\boldsymbol{\phi}}_{n-1}^T \hat{\mathbf{I}}_n^A \hat{\boldsymbol{\phi}}_{n-1} \right)^{-1} \left(\tau_{n-1} - \hat{\boldsymbol{\phi}}_{n-1}^T \hat{\boldsymbol{\beta}}_n^A \right) + \hat{\boldsymbol{\beta}}_n^A \tag{3.24}$$

Equation (3.24) can be simplified, yielding (3.25):

$$\hat{\mathbf{F}}_n = N_n \hat{\mathbf{X}}^n_{n-1} \hat{\mathbf{a}}_{n-1} + n_n M_n^{-1} \left(\tau_{n-1} - \hat{\boldsymbol{\phi}}^T_{n-1} \hat{\boldsymbol{\beta}}^A_n \right) + \hat{\boldsymbol{\beta}}^A_n + N_n \hat{\mathbf{C}}_n \tag{3.25}$$

where:

$$N_n = \hat{\mathbf{I}}^A_n - n_n M_n^{-1} n_n^T \tag{3.26}$$

$$n_n = \hat{\mathbf{I}}^A_n \hat{\boldsymbol{\phi}}_{n-1} \tag{3.27}$$

$$M_n = \hat{\boldsymbol{\phi}}^T_{n-1} \hat{\mathbf{I}}^A_n \hat{\boldsymbol{\phi}}_{n-1} \tag{3.28}$$

Moving to the link immediately below the end-effector, one has the following balance of forces:

$$\hat{\mathbf{F}}_{n-1} - \left(\hat{\mathbf{X}}^n_{n-1} \right)^T \hat{\mathbf{F}}_n = \hat{\mathbf{I}}_{n-1} \hat{\mathbf{a}}_{n-1} + \hat{\boldsymbol{\beta}}_n \tag{3.29}$$

The expression for the force that the end-effector does on this link is given by (3.25). Introducing (3.25) in (3.29) and rearranging it to show the spatial acceleration, results in (3.30):

$$\hat{\mathbf{F}}_{n-1} = \left(\hat{\mathbf{I}}_{n-1} + \left(\hat{\mathbf{X}}^n_{n-1} \right)^T N_n \hat{\mathbf{X}}^n_{n-1} \right) \hat{\mathbf{a}}_{n-1} + \left(\hat{\boldsymbol{\beta}}_{n-1} + \left(\hat{\mathbf{X}}^n_{n-1} \right)^T \left(\hat{\boldsymbol{\beta}}^A_n + n_n M_n^{-1} \tau^*_{n-1} + N_n \hat{\mathbf{C}}_n \right) \right) \tag{3.30}$$

where:

$$\tau^*_{n-1} = \tau_{n-1} - \hat{\boldsymbol{\phi}}^T_{n-1} \hat{\boldsymbol{\beta}}^A_n \tag{3.31}$$

Equation (3.30) has a structure similar to the balance of forces of the end-effector, given by (3.20), and can be rearranged into (3.32):

$$\hat{\mathbf{F}}_{n-1} = \hat{\mathbf{I}}^A_{n-1}\hat{\mathbf{a}}_{n-1} + \hat{\boldsymbol{\beta}}^A_{n-1} \tag{3.32}$$

where:

$$\hat{\mathbf{I}}^A_{n-1} = \hat{\mathbf{I}}_{n-1} + \left(\hat{\mathbf{X}}^n_{n-1}\right)^T N_n \hat{\mathbf{X}}^n_{n-1} \tag{3.33}$$

$$\hat{\boldsymbol{\beta}}^A_{n-1} = \hat{\boldsymbol{\beta}}_{n-1} + \left(\hat{\mathbf{X}}^n_{n-1}\right)^T \left(\hat{\boldsymbol{\beta}}^A_n + n_n M_n^{-1}\tau^*_{n-1} + N_n \hat{\mathbf{C}}_n\right) \tag{3.34}$$

With the balance of forces given by (3.32), the link becomes an independent system, enabling it to be handled like an end-effector.

Equations (3.33) and (3.34) can be extended to a generic form that can be applied to any link of the serial structure, (3.35) and (3.36):

$$\hat{\mathbf{I}}^A_{i-1} = \hat{\mathbf{I}}_{i-1} + \left(\hat{\mathbf{X}}^i_{i-1}\right)^T N_i \hat{\mathbf{X}}^i_{i-1} \tag{3.35}$$

$$\hat{\boldsymbol{\beta}}^A_{i-1} = \hat{\boldsymbol{\beta}}_{i-1} + \left(\hat{\mathbf{X}}^i_{i-1}\right)^T \left(\hat{\boldsymbol{\beta}}^A_i + n_i M_i^{-1}\tau^*_{i-1} + N_i \hat{\mathbf{C}}_i\right) \tag{3.36}$$

with the following initial conditions:

$$\hat{\mathbf{I}}^A_n = \hat{\mathbf{I}}_n$$

$$\hat{\boldsymbol{\beta}}^A_n = \hat{\boldsymbol{\beta}}_n$$

3.1.4. External and Dynamic Forces

The algorithm, with the equations presented this far, does not handle external forces applied to the links or dynamic forces on the joint: force coming from elasticity and damping.

The balance of forces with the application of external force is given by (3.37):

$$\hat{\mathbf{F}}_{i-1} - \left(\hat{\mathbf{X}}_{i-1}^{i}\right)^{T} \hat{\mathbf{F}}_{i} - \left(\hat{\mathbf{X}}_{i-1}^{e}\right)^{T} \hat{\mathbf{F}}_{i}^{e} = \hat{\mathbf{I}}_{i-1}\hat{\mathbf{a}}_{i-1} + \hat{\boldsymbol{\beta}}_{i} \tag{3.37}$$

where $\hat{\mathbf{F}}^{e}$ is the external force and $\hat{\mathbf{X}}_{i-1}^{e}$ is the spatial transformation from the link base reference frame to the application point of the external force.

Adding to both sides of (3.37) the external force terms, the spatial balance of forces becomes again (3.14) if one joins the spatial force bias and the external force terms in one and (3.19) becomes (3.38):

$$\hat{\boldsymbol{\beta}}_{i} = \begin{bmatrix} \boldsymbol{\omega}_{i} \times \left(\boldsymbol{\omega}_{i} \times \mathbf{r}_{i}^{CM}\right) \\ \boldsymbol{\omega}_{i} \times \left(\mathbf{I}_{i}^{O}\boldsymbol{\omega}_{i}\right) \end{bmatrix} + \left(\hat{\mathbf{X}}_{i-1}^{e}\right)^{T} \hat{\mathbf{F}}_{i}^{e} \tag{3.38}$$

The dynamic forces can be collected in a single expression, (3.39):

$$\tau_{i}^{Dyn} = c_{i}\dot{\theta}_{i} + k_{i}\left(\theta_{i} - \theta_{i}^{initial}\right) \tag{3.39}$$

where τ_i^{Dyn} is the dynamic forces generated torque, c is the angular damping coefficient, k is the torsion spring constant, and $\theta_i^{initial}$ is the initial position of the spring (the position where the spring torque is zero).

To introduce the effect of the dynamic forces on the algorithm, one must subtract (3.39) from (3.31):

$$\tau_{i-1}^{*} = \tau_{i-1} - \tau_{i-1}^{Dyn} - \hat{\boldsymbol{\phi}}_{i-1}^{T}\hat{\boldsymbol{\beta}}_i^{A} \tag{3.40}$$

3.1.5. The algorithm

The algorithm to determine the joint accelerations is divided in three cycles. The first cycle is where the velocity dependent variables are determined: the angular velocities of the links, the centripetal accelerations and the spatial force bias.

For i = 1 to i = n
$\boldsymbol{\omega}_i = \mathbf{R}_{i-1}^{i}\boldsymbol{\omega}_{i-1} + \dot{\boldsymbol{\theta}}_{i-1}$
$\hat{\mathbf{C}}_i = \begin{bmatrix} \mathbf{R}_{i-1}^{i}\left(\boldsymbol{\omega}_{i-1} \times \left(\boldsymbol{\omega}_{i-1} \times \mathbf{r}_{i-1}^{L}\right)\right) \\ \boldsymbol{\omega}_i \times \boldsymbol{\phi}_i^{T}\dot{\theta}_i \end{bmatrix}$
$\hat{\boldsymbol{\beta}}_i = \begin{bmatrix} \boldsymbol{\omega}_i \times \left(\boldsymbol{\omega}_i \times \mathbf{r}_i^{CM}\right) \\ \boldsymbol{\omega}_i \times \left(\mathbf{I}_i^{O}\boldsymbol{\omega}_i\right) \end{bmatrix}$

The cycle starts on the base link (i = 0) and, at this link, the angular velocity is known (if the structure is fixed the velocity is zero). The input values are the joint angular velocities from the previous iteration or, if it is the first iteration, the initial state of the robot.

The second cycle is responsible for the determination of the articulated-body quantities: the articulated-body inertia and articulated-body force bias.

For i = n to i = 1
$n_i = \hat{\mathbf{I}}_i^A \hat{\boldsymbol{\phi}}_{i-1}$
$M_i = \hat{\boldsymbol{\phi}}_{i-1}^T \hat{\mathbf{I}}_i^A \hat{\boldsymbol{\phi}}_{i-1}$
$N_i = \hat{\mathbf{I}}_i^A - n_i M_i^{-1} n_i^T$
$\tau_i^{Dyn} = c_i \dot{\theta}_i + k_i \left(\theta_i - \theta_i^{initial} \right)$
$\tau_{i-1}^* = \tau_{i-1} - \hat{\boldsymbol{\phi}}_{i-1}^T \hat{\boldsymbol{\beta}}_i^A$
$\hat{\mathbf{I}}_{i-1}^A = \hat{\mathbf{I}}_{i-1} + \left(\hat{\mathbf{X}}_{i-1}^i \right)^T N_i \hat{\mathbf{X}}_{i-1}^i$
$\hat{\boldsymbol{\beta}}_{i-1}^A = \hat{\boldsymbol{\beta}}_{i-1} + \left(\hat{\mathbf{X}}_{i-1}^i \right)^T \left(\hat{\boldsymbol{\beta}}_i^A + n_i M_i^{-1} \tau_{i-1}^* + N_i \hat{\mathbf{C}}_i \right)$

This cycle starts on the end-effector and consequently, the articulated-body inertia is equal to the spatial inertia (which is known) and the articulated-body force bias is equal to the spatial force bias, given by the first cycle.

The third and last cycle is where the spatial and joint accelerations are calculated:

For i = 1 to i = n
$\hat{\mathbf{a}}_i' = \hat{\mathbf{X}}_{i-1}^i \hat{\mathbf{a}}_{i-1} + \hat{\mathbf{C}}_i$
$\ddot{\theta}_{i-1} = M_i^{-1} \left(\tau_{i-1}^* - n_i^T \hat{\mathbf{a}}_i' \right)$
$\hat{\mathbf{a}}_i = \hat{\mathbf{a}}_i' + \hat{\boldsymbol{\phi}}_{i-1} \ddot{\theta}_{i-1}$

The cycle stars, again at the base link and, like on the first cycle, the spatial acceleration is known (if the base link is fixed the acceleration is the acceleration of gravity).

The last step of the algorithm is to integrate the joint accelerations over the sample time to get the joint velocities and integrate the joint velocities to get the joint positions.

3.2. Adaptation of the ABA to Tree Structures

The algorithm presented on the previous section only handles serial structures, but the human hand is a tree structure, one base link and multiple end-effectors.

3.2.1. Generalization of the equations

If one has multiple links connected to another link, the spatial balance of force, given by (3.14), becomes:

$$\hat{\mathbf{F}}_{i-1} - \sum_{j}\left(\left({}^{j}\hat{\mathbf{X}}_{i-1}^{i}\right)^{T}\,{}^{j}\hat{\mathbf{F}}_{i}\right) = \hat{\mathbf{I}}_{i-1}\hat{\mathbf{a}}_{i-1} + \hat{\boldsymbol{\beta}}_{i} \tag{3.41}$$

where the left superscript, *j*, represents the children links (upper links directly connected to current link).

To begin the derivation of the new ABM, one must consider multiple end-effectors connected to a single link. In this case, although being independent, all end-effectors have the same base spatial acceleration. In order to simplify the computation they will be treated as a group, rather than one by one:

$$\sum_j \left({}^j\hat{\mathbf{F}}_n \right) = \sum_j \left({}^j\hat{\mathbf{I}}_n^A \right) \hat{\mathbf{a}}_n + \sum_j \left({}^j\hat{\boldsymbol{\beta}}_n^A \right) \tag{3.42}$$

There are two kinds of links on a tree structure: a link with multiple joints each one connecting to another link or a link with one joint connecting to multiple links (the case of the human hand and the one that will be studied). This difference affects mainly how the joint accelerations are calculated. Expanding (3.42) and solving it in order to get the joint acceleration one obtains:

$$\ddot{\theta}_{n-1} = \left(\hat{\boldsymbol{\phi}}_{n-1}^T \sum_j \left({}^j\hat{\mathbf{I}}_n^A \right) \hat{\boldsymbol{\phi}}_{n-1} \right)^{-1} \left(\tau_{n-1} - \hat{\boldsymbol{\phi}}_{n-1}^T \sum_j \left({}^j\hat{\boldsymbol{\beta}}_n^A \right) - \hat{\boldsymbol{\phi}}_{n-1}^T \sum_j \left({}^j\hat{\mathbf{I}}_n^A \right) \left(\hat{\mathbf{X}}_{n-1}^n \hat{\mathbf{a}}_{n-1} + \hat{\mathbf{C}}_n \right) \right) \tag{3.43}$$

Replacing (3.43) back into (3.42), an expression similar to (3.25) can be obtained.

$${}^j\hat{\mathbf{F}}_n = {}^jN_n \, {}^j\hat{\mathbf{X}}_{n-1}^n \hat{\mathbf{a}}_{n-1} + {}^jn_n \, {}^jM_n^{-1} \, {}^j\tau_{n-1}^A + {}^j\hat{\boldsymbol{\beta}}_i^A + {}^jN_n \hat{\mathbf{C}}_i \tag{3.44}$$

where:

$${}^jN_n = {}^j\hat{\mathbf{I}}_n^A - {}^jn_n \, {}^jM_n^{-1} \, {}^jn_n^T \tag{3.45}$$

$${}^jM_n = \hat{\boldsymbol{\phi}}_n^T \, {}^jn_n \tag{3.46}$$

$${}^jn_n = {}^j\hat{\mathbf{I}}_n^A \hat{\boldsymbol{\phi}}_n \tag{3.47}$$

$${}^j\tau_{n-1}^* = \tau_{n-1} - \hat{\boldsymbol{\phi}}_{n-1}^T \, {}^j\hat{\boldsymbol{\beta}}_i^A \tag{3.48}$$

Moving to the *i*-1 link, replacing (3.44) into its spatial force balance and simplifying the result, (3.41) becomes:

$$\hat{\mathbf{F}}_{n-1} = \left(\hat{\mathbf{I}}_{n-1} + \sum_j \left(\left({}^j\hat{\mathbf{X}}_{n-1}^n \right)^T {}^j N_n \, {}^j\hat{\mathbf{X}}_{n-1}^n \right) \right) \hat{\mathbf{a}}_{n-1} + \left(\hat{\boldsymbol{\beta}}_{n-1} + \sum_j \left(\left({}^j\hat{\mathbf{X}}_{n-1}^n \right)^T \left({}^j N_n \hat{\mathbf{C}}_n + {}^j n_n \, {}^j M_n^{-1} \boldsymbol{\tau}_{n-1}^* + {}^j\hat{\boldsymbol{\beta}}_n^A \right) \right) \right) \tag{3.49}$$

Again, the generic expressions for the articulated-body inertia and force bias can be taken from the previous equation:

$$\hat{\mathbf{I}}_{i-1}^A = \hat{\mathbf{I}}_{i-1} + \sum_j \left(\left({}^j\hat{\mathbf{X}}_{i-1}^i \right)^T {}^j N_i \, {}^j\hat{\mathbf{X}}_{i-1}^i \right) \tag{3.50}$$

$$\hat{\boldsymbol{\beta}}_{i-1}^A = \hat{\boldsymbol{\beta}}_{i-1} + \sum_j \left(\left({}^j\hat{\mathbf{X}}_{i-1}^i \right)^T \left({}^j N_i \hat{\mathbf{C}}_i + {}^j n_i \, {}^j M_i^{-1} \boldsymbol{\tau}_{i-1}^* + {}^j\hat{\boldsymbol{\beta}}_i^A \right) \right) \tag{3.51}$$

3.2.2. Changes to the ABA

With the introduction of tree structures in the ABA, the presented algorithm has to be changed.

The first thing to be changed is how the cycles are done. For serial structures, the cycles were done link-by-link from one end to the other. But for tree structures the cycles must be done link-by-link and level-by-level, Fig. 3-5.

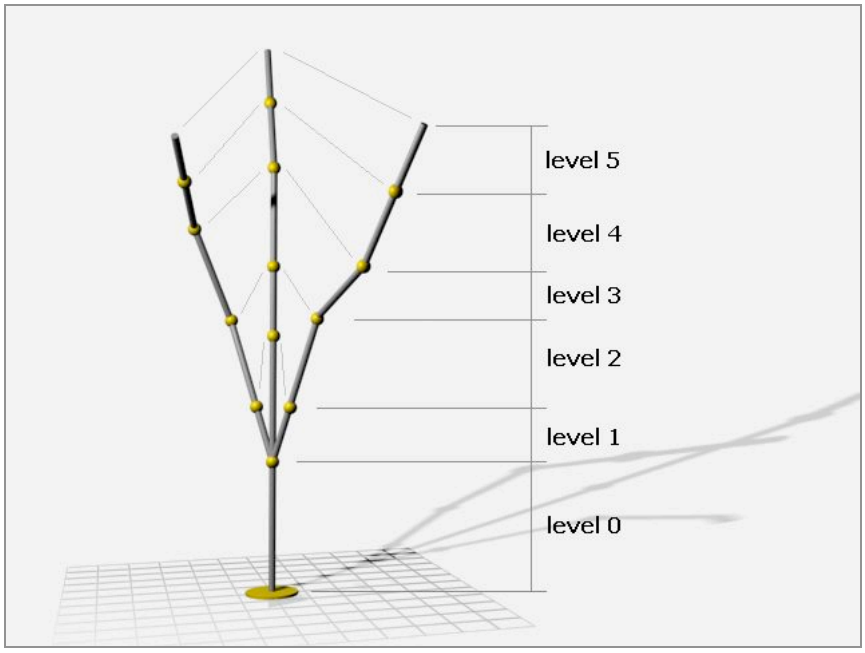

Fig. 3-5 Level arrangement.

Note that although requiring two loops for each cycle, the algorithm remains *O(n)*, because the algorithm only runs once for each link.

The second change is how the articulated-body inertia and force bias are calculated. Before the second cycle (where the articulated-quantities are determined) one must initialize all articulated-body inertias and force bias with the values of the spatial counterparts. Then on the second cycle, instead of using (3.50) and (3.51), we use (3.52) and (3.53).

$$\hat{\mathbf{I}}_{i-1}^{A} = \hat{\mathbf{I}}_{i-1}^{A} + \left({}^{j}\hat{\mathbf{X}}_{i-1}^{i}\right)^{T} {}^{j}N_i \, {}^{j}\hat{\mathbf{X}}_{i-1}^{i} \tag{3.52}$$

$$\hat{\boldsymbol{\beta}}_{i-1}^{A} = \hat{\boldsymbol{\beta}}_{i-1}^{A} + \left({}^{j}\hat{\mathbf{X}}_{i-1}^{i}\right)^{T} \left({}^{j}N_i\hat{\mathbf{C}}_i + {}^{j}n_i \, {}^{j}M_i^{-1}\tau_{i-1}^{*} + {}^{j}\hat{\boldsymbol{\beta}}_i^{A}\right) \tag{3.53}$$

3.3. Joint limits

With almost every joint there are limits. Normally a rotational joint cannot rotate 360º and the joints of the human hand are not an exception.

Joint limits, although simple saturation functions, impose several modification to the ABA algorithm, because they require that we pre-establish some of the solutions of the algorithm.

The first step is detecting if a joint limit is attained, by testing the solutions against the saturation values of each joint. Then, if at least one of the joints saturates, we must determine when it happened. This step is very important, because, if a joint saturates between sample times, the solutions obtained from that point beyond are incorrect. How the time of the saturation is determined depends on the numerical integration method used to calculate the joint velocities and positions. For the Forward Euler integration method we must solve the following equation for the saturated joint, (3.54).

$$\frac{1}{2}\ddot{\theta}_0 t_{sat}^2 + \dot{\theta}_0 t_{sat} + (\theta_0 - \theta_{sat}) = 0 \qquad (3.54)$$

After the saturation time is calculated, we must integrate the accelerations of all joints to get the status of the structure just before the saturation is attained.

At this point a new problem arises. Since the saturated joint cannot go any further, every torque applied to the joint that makes the joint move in the saturated direction is counteracted by a reaction torque with the same magnitude

and opposite direction. This reaction torque is unknown, but we only need to know its direction, because, when the joint is saturated, the total torque applied to the joint is zero, (3.40), independently of the magnitude of the external torque.

With the torque problem solved, the ABA must be run, for the rest of the sample time, to get the correct values, knowing that at the saturated joint, the position is the saturation position, and the velocity, acceleration and total torque are zero.

To test if the joint is no longer saturated, one must check if the external torque rotates the joint away from the saturation point.

Chapter 4

IMPACT AND CONTACT

4.1. Impact

Impact is a severe disturbance to a robot and can cause malfunction or unpredicted behavior (especially if the controller is not designed to handle unpredicted changes in the robot state). Because of this the impact analysis is a major area of study [19], [20], [21], [22], [23], [24], [25], [26].

The impact impulse equations given by the traditional rigid body dynamics are well known, [20], [21], but these expressions fail when the impacting rigid bodies have their movements constrained, e.g., any articulated structure. One solution to this problem is given by [22], where it is used that the fact that the relation between the impact impulse and the variation of the velocity is linear and constant for a given joint configuration. This linear transformation is determined by running the Impulse Articulated-body Algorithm (IABA) for a known arbitrary "test" impact impulse. After the matrix is determined it must be inverted in order to get the impact impulse.

In this method the IABA must be run four times to complete the calculations: one for each of the three components of the "test" impact impulse, and a fourth to get the results. In addition to the heavy number of computations, the method does not guarantee the invertibility of the linear transformation matrix, especially when one of the bodies intervening on the impact is fixed, e.g., a ground plane.

The focus of this chapter is to find a less computationally expensive and a non-black box model for the impact impulse using the properties and advantages of the IABA.

4.1.1. Impulse Articulated Body Algorithm

4.1.1.1. Algorithm equations

In the theory of rigid body dynamics, the impact is instantaneous and the impacting objects are affected by an external impulse with the direction of the normal of the contact plane. This impulse shifts the velocity to a direction pointing away from the other object, Fig. 4-1.

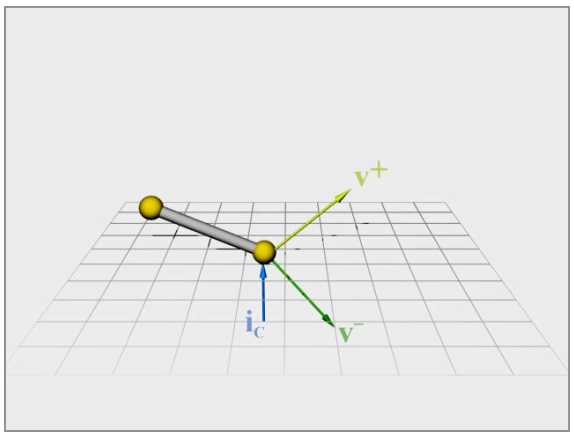

Fig. 4-1 Impact impulse.

Since the duration of the impact is zero, there is a discontinuity in the velocities and accelerations of the rigid bodies, and an infinite force must exist at the point of contact to create a finite impulse, (4.1):

$$\mathbf{i} = \mathbf{F}\Delta t \tag{4.1}$$

where **i** is the impulse.

Because of this infinite force, the simulation of the impact needs to be done on an impulse-based ABA rather than the traditional force-based ABA.

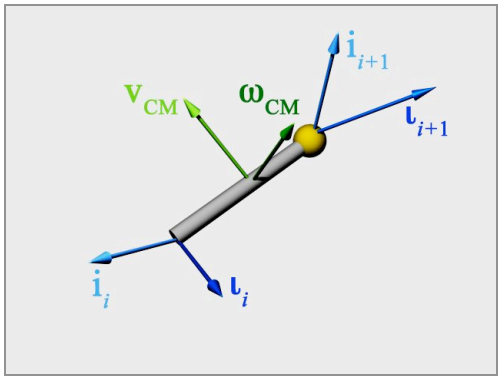

Fig. 4-2 Applied external impulses to the link.

The Impulse Articulated Body Algorithm (IABA) has its foundation on the time integral of (3.14), given by (4.2), Fig. 4-2.

$$\hat{\mathbf{i}}_i - \left(\hat{\mathbf{X}}_i^{i+1}\right)^T \hat{\mathbf{i}}_{i+1} = \hat{\mathbf{I}}_i \Delta\hat{\mathbf{v}}_i \tag{4.2}$$

where $\Delta\hat{\mathbf{v}}_i$ is the variation of the spatial velocity of the link, and $\hat{\mathbf{i}}$ is the spatial impulse, given by (4.3):

$$\hat{\mathbf{i}}_i = \begin{bmatrix} \mathbf{i}_i \\ \mathbf{t}_i^O \end{bmatrix} \tag{4.3}$$

where $\mathbf{t}_i^O$ is the angular impulse about the origin of the link base frame and $\hat{\mathbf{I}}$ is the spatial inertia matrix, (3.18).

Considering the last link of a chain of rigid bodies and that this link has an external impulse applied to it, we have (4.4):

$$\hat{\mathbf{i}}_i = \hat{\mathbf{I}}_i \Delta\hat{\mathbf{v}}_i + \hat{\boldsymbol{\gamma}}_i \tag{4.4}$$

where $\hat{\boldsymbol{\gamma}}_i$ is the spatial impulse bias, which contains the external impulse (relocated to the origin of the link base frame).

Since the link in study is the last one of its chain, the spatial inertia and spatial impulse bias are equal to the articulated-body inertia and articulated-body force bias, (4.5):

$$\hat{\mathbf{i}}_i = \hat{\mathbf{I}}_i^A \Delta\hat{\mathbf{v}}_i + \hat{\boldsymbol{\gamma}}_i^A \tag{4.5}$$

Introducing the variation version of (3.12) into (4.5), we get (4.5):

$$\hat{\mathbf{i}}_i = \hat{\mathbf{I}}_i^A \left(\hat{\mathbf{X}}_{i-1}^i \Delta\hat{\mathbf{v}}_{i-1} + \hat{\boldsymbol{\phi}}_i \Delta\dot{\theta}_i \right) + \hat{\boldsymbol{\gamma}}_i^A \tag{4.6}$$

Pre-multiplying (4.6) by the transpose of the axis space vector, $\hat{\boldsymbol{\phi}}_i^T$, and solving it for the variation of the joint angular velocity we obtain (4.7):

$$\Delta\dot{\theta}_i = \left(\hat{\boldsymbol{\phi}}_i^T \hat{\mathbf{I}}_i^A \hat{\boldsymbol{\phi}}_i\right)^{-1} \left(\iota_i - \hat{\boldsymbol{\phi}}_i \hat{\boldsymbol{\gamma}}_i^A - \hat{\boldsymbol{\phi}}_i^T \hat{\mathbf{I}}_i^A \hat{\mathbf{X}}_{i-1}^i \Delta\hat{\mathbf{v}}_{i-1}\right) \tag{4.7}$$

where ι_i is the impulse of the applied moment on the joint. Since the impact is instantaneous this term is zero.

Placing (4.7) back into (4.6) results in (4.8):

$$\hat{\mathbf{i}}_i = \mathbf{N}_i \hat{\mathbf{X}}_{i-1}^i \Delta\hat{\mathbf{v}}_{i-1} - \mathbf{n}_i \mathbf{M}_i^{-1} \hat{\boldsymbol{\phi}}_i \hat{\boldsymbol{\gamma}}_i^A + \hat{\boldsymbol{\gamma}}_i^A \tag{4.8}$$

Substituting (4.8) into (4.2) for the *i*-1 link, we get the expressions of the articulated-body inertia, which is similar to the one from ABA, and the expression for the articulated-body impulse bias, (4.9):

$$\hat{\boldsymbol{\gamma}}_{i-1}^A = \left(\hat{\mathbf{X}}_{i-1}^i\right)^T \left(\mathbf{1} - \mathbf{n}_i \mathbf{M}_i^{-1} \hat{\boldsymbol{\phi}}_i^T\right) \hat{\boldsymbol{\gamma}}_i^A \tag{4.9}$$

4.1.2. The algorithm

The algorithm has two cycles summarized as follows:

1) Articulated-Body quantities cycle: Starting at the last link of the chain, compute the articulated-body inertias and articulated-body impulse bias. The articulated-body inertia of the last link is equal to its spatial inertia, and the articulated-body impulse bias is equal to the impact impulse relocated

to the origin of the link base frame. Note that the impact impulse is not necessarily at the last link.

2) Velocities cycle: Starting at the first link, compute the variation of the spatial velocity and variation of the joint velocity for each link. If the first link is fixed, the variation of the velocity of the base link is zero

4.1.3. Impact Impulse for Constrained Rigid Bodies

4.1.3.1. Impact Impulse

The impulse generated by the impact of two rigid-bodies depends exclusively on the normal component of the relative velocity of the bodies, and their masses and inertias. The analytical expression for the impact impulse of two rigid bodies (denoted here "1" and "2") is given by (4.10), [21]:

$$\mathbf{i}_c = \frac{-(1+e)\left(\mathbf{v}_2^- - \mathbf{v}_1^-\right)}{\sum_{k=1}^{2}\left(\frac{1}{m_k} + \hat{\mathbf{n}}\cdot\left(\mathbf{I}_k^{-1}\left(\mathbf{r}_k \times \hat{\mathbf{n}}\right)\times \mathbf{r}_k\right)\right)} \tag{4.10}$$

where $\hat{\mathbf{n}}$ is the unitary normal of the contact plane, $\mathbf{r}_k$ is the position of the contact point in the body k relatively to its CM, $\mathbf{v}^-$ is the linear velocity of the contact point immediately before the impact, e is the restitution coefficient, and $\mathbf{i}_c$ is the impact linear impulse. The restitution coefficient measures the elasticity of an impact: 1 for totally elastic impacts and 0 for inelastic impacts.

Equation (4.10), although generic, fails when the impacting rigid bodies have constrained movements, e.g. articulated structures. In order to solve this problem we must determine the extension of (4.10) for articulated rigid bodies structures.

The first step is the elimination of the recursive form of (4.9), knowing that the first non-zero $\hat{\boldsymbol{\gamma}}^A$ in the recursion is the one corresponding to impacting link, (4.11):

$$\hat{\boldsymbol{\gamma}}_{n_C}^A = \hat{\boldsymbol{\gamma}}_{n_C} = -\left(\hat{\mathbf{X}}_{n_C}^{\mathbf{r}^C}\right)^T \hat{\mathbf{i}}_C \tag{4.11}$$

where n_C denotes the index of the colliding link and is greater than 0 and lesser or equal to the number of links. $\mathbf{r}^C$ is the position of the contacting point relatively to the link base frame, $\hat{\mathbf{X}}_{n_C}^{\mathbf{r}^C}$ is the corresponding spatial transformation matrix, and $\hat{\mathbf{i}}_C$ is the spatial impact impulse.

The non-recursive form of (4.9) is shown on (4.12):

$$\hat{\boldsymbol{\gamma}}_i^A = \left(\prod_{j=i+1}^{n_C} A_j\right)\hat{\boldsymbol{\gamma}}_{n_C}^A \tag{4.12}$$

where:

$$A_i = \left(\hat{\mathbf{X}}_{i-1}^i\right)^T \left(\mathbf{1} - n_i M_i^{-1} \hat{\boldsymbol{\phi}}_i^T\right) \tag{4.13}$$

The next step is to do the same, but for variation of velocity equation, (4.14):

$$\Delta\hat{\mathbf{v}}_i = \hat{\mathbf{X}}_{i-1}^{i}\Delta\hat{\mathbf{v}}_{i-1} + \hat{\boldsymbol{\phi}}_i\Delta\dot{\theta}_i \tag{4.14}$$

Replacing (4.7) into (4.14) and rearranging the result to explicit the articulated-body impulse bias, yields (4.15):

$$\Delta\hat{\mathbf{v}}_i = A_i^T\Delta\hat{\mathbf{v}}_{i-1} - \psi_i\hat{\boldsymbol{\gamma}}_i^A \tag{4.15}$$

where:

$$\psi_i = \hat{\boldsymbol{\phi}}_i\,\mathbf{M}_i^{-1}\hat{\boldsymbol{\phi}}_i^T \tag{4.16}$$

Removing the recursion from (4.15), we obtain the relation between the variation of the velocity on the impacting link and the articulated-body impulse bias,(4.17):

$$\Delta\hat{\mathbf{v}}_{n_C} = -\sum_{i=1}^{n_C}\left(\left(\prod_{j=i+1}^{n_C}A_j\right)^T\psi_i\left(\prod_{j=i+1}^{n_C}A_j\right)\right)\hat{\boldsymbol{\gamma}}_{n_C}^A \tag{4.17}$$

Analyzing the computational cost of (4.17), one reaches the conclusion that it is a $O(n^2)$, which is highly prejudicial to the performance of the algorithm. The solution is to transform (4.17) back into a recursive equation, (4.18):

$$\Delta\hat{\mathbf{v}}_{n_C} = -\Psi_{n_C}\hat{\boldsymbol{\gamma}}_{n_C}^A \tag{4.18}$$

where:

$$\Psi_i = A_i^T\Psi_{i-1}A_i + \psi_i \tag{4.19}$$

The starting point for (4.19) is $\Psi_1 = \psi_1$. The main advantage of (4.18) is that it is *O(n)* equation.

Replacing (4.11) into (4.18) and pre-multiplying it by $\hat{\mathbf{X}}^{\mathbf{r}^C}_{n_C}$ to get the variation of the velocity at the contact point, we obtain (4.20):

$$\hat{\mathbf{X}}^{\mathbf{r}^C}_{n_C} \Delta\hat{\mathbf{v}}_{n_C} = \hat{\mathbf{X}}^{\mathbf{r}^C}_{n_C} \Psi_{n_C} \left(\hat{\mathbf{X}}^{\mathbf{r}^C}_{n_C}\right)^T \hat{\mathbf{i}}_C \tag{4.20}$$

Because we are dealing with frictionless impact, only the normal component of the variation of the velocity is affected by the impulse and the impulse has the same direction of the normal. Pre-multiplying (4.20) by the transpose of the normal direction (converted to a spatial vector) and solving the result to get the impact impulse norm, we have (4.21):

$$\left\|\mathbf{i}_c\right\| = \frac{\hat{\mathbf{n}}^T_{n_C} \hat{\mathbf{X}}^{\mathbf{r}^C}_{n_C} \Delta\hat{\mathbf{v}}_{n_C}}{\hat{\mathbf{n}}^T_{n_C} \hat{\mathbf{X}}^{\mathbf{r}^C}_{n_C} \Psi_{n_C} \left(\hat{\mathbf{X}}^{\mathbf{r}^C}_{n_C}\right)^T \hat{\mathbf{n}}_{n_C}} \tag{4.21}$$

where $\hat{\mathbf{n}}_{n_C}$ is the spatial version of $\hat{\mathbf{n}}$ on the impacting link referential.

From [20], we know that the velocity (of the impact point) immediately after the impact is directly proportional to the velocity immediately before the impact and is given by (4.22):

$$\hat{\mathbf{n}}^T_{n_C} \hat{\mathbf{X}}^{\mathbf{r}^C}_{n_C} \hat{\mathbf{v}}^+_{n_c} = -e\, \hat{\mathbf{n}}^T_{n_C} \hat{\mathbf{X}}^{\mathbf{r}^C}_{n_C} \hat{\mathbf{v}}^-_{n_c} \tag{4.22}$$

Using (4.22), we can write the variation of the velocity as function of the velocity immediately before the impact, $\hat{\mathbf{v}}_{n_c}^{-}$, and consequently (4.21) becomes (4.23):

$$\left\|\mathbf{i}_c\right\| = -(1+e)\frac{\hat{\mathbf{n}}_{n_C}^T \hat{\mathbf{X}}_{n_C}^{\mathbf{r}^C} \hat{\mathbf{v}}_{n_c}^{-}}{\hat{\mathbf{n}}_{n_C}^T \hat{\mathbf{X}}_{n_C}^{\mathbf{r}^C} \Psi_{n_C} \left(\hat{\mathbf{X}}_{n_C}^{\mathbf{r}^C}\right)^T \hat{\mathbf{n}}_{n_C}} \tag{4.23}$$

Equation (4.21) gives us the impact norm for the collision of an articulated structure with the ground (a fixed object with a much greater mass than the articulated structure), but (4.21) can be modified for the more generic situation, that is the impact of two articulated structures, (4.24):

$$\left\|\mathbf{i}_c\right\| = -(1+e)\frac{\hat{\mathbf{n}}^T \left(\left({}^1\hat{\mathbf{R}}_0^{n_c}\right)^T {}^1\hat{\mathbf{X}}_{n_C}^{\mathbf{r}^C} {}^1\hat{\mathbf{v}}_{n_c}^{-} - \left({}^2\hat{\mathbf{R}}_0^{n_c}\right)^T {}^2\hat{\mathbf{X}}_{n_C}^{\mathbf{r}^C} {}^2\hat{\mathbf{v}}_{n_c}^{-}\right)}{\hat{\mathbf{n}}^T \left(\left({}^1\hat{\mathbf{R}}_0^{n_c}\right)^T {}^1\hat{\mathbf{X}}_{n_C}^{\mathbf{r}^C} {}^1\Psi_{n_C} \left({}^1\hat{\mathbf{X}}_{n_C}^{\mathbf{r}^C}\right)^T {}^1\hat{\mathbf{R}}_0^{n_c} + \left({}^2\hat{\mathbf{R}}_0^{n_c}\right)^T {}^2\hat{\mathbf{X}}_{n_C}^{\mathbf{r}^C} {}^2\Psi_{n_C} \left({}^2\hat{\mathbf{X}}_{n_C}^{\mathbf{r}^C}\right)^T {}^2\hat{\mathbf{R}}_0^{n_c}\right)\hat{\mathbf{n}}} \tag{4.24}$$

where the left superscript value identifies the articulated body, $\hat{\mathbf{n}}$ is the normal the base referential, and $\hat{\mathbf{R}}_0^{n_C}$ is spatial transformation matrix, from the base to the impacting link, for rotations only. Equation (4.24) has more coordinate transformations, because the normal vector must be in a referential shared by both articulated bodies.

Finally to get the impact impulse we must multiply the impact norm, given by (4.21) or (4.24), by the normal spatial vector.

4.1.3.2. Simultaneous Impacts

Simultaneous impacts are rare in the physical world, because the probability of two events happening at the same instant is extremely small. But since the simulation is done in a discrete time, this possibility must be dealt with.

When considering multiple impacts (4.12) must be replaced with (4.25) for each impacting link:

$$\hat{\boldsymbol{\gamma}}_i^A = \hat{\boldsymbol{\gamma}}_i + A_{i+1}\hat{\boldsymbol{\gamma}}_{i+1}^A \tag{4.25}$$

Repeating the same mathematical manipulations done for the single impact impulse, one reaches the following system, (4.26):

$$\begin{bmatrix} \Delta\hat{\mathbf{v}}_{c_1} \\ \Delta\hat{\mathbf{v}}_{c_2} \\ \vdots \end{bmatrix} = \begin{bmatrix} \Psi_{c_1} & \Psi_{c_2}\left(\prod_{j=c_1+1}^{c_2} A_j\right) & \cdots \\ \left(\prod_{j=c_1+1}^{c_2} A_j\right)^T \Psi_{c_2} & \Psi_{c_2} & \cdots \\ \vdots & \vdots & \ddots \end{bmatrix} \begin{bmatrix} \hat{\boldsymbol{\gamma}}_{c_1} \\ \hat{\boldsymbol{\gamma}}_{c_2} \\ \vdots \end{bmatrix} \tag{4.26}$$

where the c_1 and c_2 are the indices of the impacting links.

The existence of a fully coupled $6m$x$6m$ system, (4.26), increases the order of the algorithm to $O(m^2+n)$, where m is the number of impacting links and is, always, less than n. If a link impacts with another link belonging to the same structure, it counts only as one impact, thus increasing m only by one.

Pre-multiplying (4.26) by the transpose of the normal vectors and by the transformation matrices, we have (4.27):

$$\begin{bmatrix} \hat{\mathbf{n}}_{c_1}^T & 0 & 0 \\ 0 & \hat{\mathbf{n}}_{c_2}^T & 0 \\ 0 & 0 & \ddots \end{bmatrix} \begin{bmatrix} \hat{\mathbf{X}}_{c_1}^{\mathbf{r}^C} & 0 & 0 \\ 0 & \hat{\mathbf{X}}_{c_2}^{\mathbf{r}^C} & 0 \\ 0 & 0 & \ddots \end{bmatrix} \begin{bmatrix} \Delta\hat{\mathbf{v}}_{c_1} \\ \Delta\hat{\mathbf{v}}_{c_2} \\ \vdots \end{bmatrix} = \begin{bmatrix} \hat{\mathbf{n}}_{c_1}^T & 0 & 0 \\ 0 & \hat{\mathbf{n}}_{c_2}^T & 0 \\ 0 & 0 & \ddots \end{bmatrix} \begin{bmatrix} \hat{\mathbf{X}}_{c_1}^{\mathbf{r}^C} & 0 & 0 \\ 0 & \hat{\mathbf{X}}_{c_2}^{\mathbf{r}^C} & 0 \\ 0 & 0 & \ddots \end{bmatrix} \begin{bmatrix} \Psi_{c_1} & \Psi_{c_2}\left(\prod_{j=c_1+1}^{c_2} A_j\right) & \cdots \\ \left(\prod_{j=c_1+1}^{c_2} A_j\right)^T \Psi_{c_2} & \Psi_{c_2} & \cdots \\ \vdots & \vdots & \ddots \end{bmatrix} \begin{bmatrix} \hat{\boldsymbol{\gamma}}_{c_1} \\ \hat{\boldsymbol{\gamma}}_{c_2} \\ \vdots \end{bmatrix} \tag{4.27}$$

Simplifying (4.27) and replacing the spatial impulse bias by (4.11), we obtain (4.28):

$$\begin{bmatrix} \hat{\mathbf{n}}_{c_1}^T \hat{\mathbf{X}}_{c_1}^{\mathbf{r}^C} \Delta\hat{\mathbf{v}}_{c_1} \\ \hat{\mathbf{n}}_{c_2}^T \hat{\mathbf{X}}_{c_2}^{\mathbf{r}^C} \Delta\hat{\mathbf{v}}_{c_2} \\ \vdots \end{bmatrix} = \begin{bmatrix} \hat{\mathbf{n}}_{c_1}^T \hat{\mathbf{X}}_{c_1}^{\mathbf{r}^C} \Psi_{c_1} \left(\hat{\mathbf{X}}_{c_1}^{\mathbf{r}^C}\right)^T \hat{\mathbf{n}}_{c_1} & \hat{\mathbf{n}}_{c_1}^T \hat{\mathbf{X}}_{c_1}^{\mathbf{r}^C} \Psi_{c_2}\left(\prod_{j=c_1+1}^{c_2} A_j\right)\left(\hat{\mathbf{X}}_{c_2}^{\mathbf{r}^C}\right)^T \hat{\mathbf{n}}_{c_2} & \cdots \\ \hat{\mathbf{n}}_{c_2}^T \hat{\mathbf{X}}_{c_2}^{\mathbf{r}^C} \left(\prod_{j=c_1+1}^{c_2} A_j\right)^T \Psi_{c_2} \left(\hat{\mathbf{X}}_{c_1}^{\mathbf{r}^C}\right)^T \hat{\mathbf{n}}_{c_1} & \hat{\mathbf{n}}_{c_2}^T \hat{\mathbf{X}}_{c_2}^{\mathbf{r}^C} \Psi_{c_2} \left(\hat{\mathbf{X}}_{c_2}^{\mathbf{r}^C}\right)^T \hat{\mathbf{n}}_{c_2} & \cdots \\ \vdots & \vdots & \ddots \end{bmatrix} \begin{bmatrix} \left\|\hat{\mathbf{i}}_{c_1}\right\| \\ \left\|\hat{\mathbf{i}}_{c_2}\right\| \\ \vdots \end{bmatrix} \tag{4.28}$$

The system (4.28) is, now, an *m*x*m* linear system that must be solved in order to get the impact impulses. The system matrix is symmetric positive definite.

4.1.3.3. New Algorithm

The determination of the impact impulse introduces some changes into the IABA algorithm described above.

1) Articulated-Body Inertia cycle: Starting at the last link of the chain, compute the articulated-body inertias for the impact joint configuration.

2) Impact impulse: Starting at the first link, calculate the Ψ matrices for each link until the impacting link. With the matrices calculated compute the impact impulse.

3) Articulated-Body Impulse Bias cycle: Starting at the impacting link, compute the articulated-body impulse bias.

4) Velocities cycle: Starting at the first link, compute the velocities of each link. If the first link is attached to the environment, the variation of the velocity of the base link is zero.

4.2. Contact

Contact between two objects happens when the impact is plastic or when the participating objects are colliding repeatedly and the impact is not elastic. The main difference between the impact and contact is that in the latter the duration is finite. This difference implies a whole new perspective because the external force is now finite, thus changing the acceleration of the rigid bodies, Fig. 4-3.

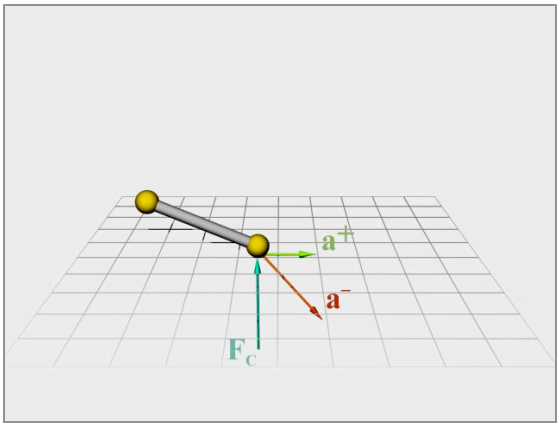

Fig. 4-3 Forces acting on an object during contact.

There are several methods to handle contact, i.e., linear complementarity problems, [27], [28], [29]. But, since in this thesis it is used the ABA, it is advantageous to use a formulation that already couples with this algorithm. So, like it was done for the impact impulse, the contact force will be derived from the ABA equations.

4.2.1. Contact Force

The contact force is the impact impulse counterpart for the contact. It depends on the articulated-body inertia, in the same fashion of the impact impulse, and depends on the external applied torque and gravity.

The contribution to the link spatial force bias is given by (4.29):

$$\hat{\boldsymbol{\beta}}_{n_c}^{c} = -\left(\hat{\mathbf{X}}_{n_C}^{\mathbf{r}^C}\right)^{T} \hat{\mathbf{F}}_{C} \tag{4.29}$$

where $\hat{\mathbf{F}}_{c}$ is the contact spatial force and $\hat{\boldsymbol{\beta}}_{n_c}^{c}$ is the contact spatial force bias.

The introduction of (4.13) into (3.36) yields (4.30):

$$\hat{\boldsymbol{\beta}}_{i-1}^{A} = B_i + A_i \hat{\boldsymbol{\beta}}_{i}^{A} \tag{4.30}$$

where:

$$B_i = \hat{\boldsymbol{\beta}}_{i-1} + \left(\hat{\mathbf{X}}_{i-1}^{i}\right)^T \left(N_i \hat{\mathbf{C}}_i + n_i M_i^{-1} \boldsymbol{\tau}_{i-1}^{*}\right) \tag{4.31}$$

and:

$$B_n = \hat{\boldsymbol{\beta}}_n$$

Removing the recursion from (4.30) and extracting the contact spatial force bias, one obtains (4.32):

$$\hat{\boldsymbol{\beta}}_{i}^{A} = \sum_{j=i}^{n} \left(\left(\prod_{k=i+1}^{j} A_k \right) \left(B_j \right) \right) + \left(\prod_{k=i+1}^{n_c} A_k \right) \hat{\boldsymbol{\beta}}_{n_c}^{c} \tag{4.32}$$

Like it was done for the velocity, the recursion must be removed from the acceleration equation, (3.13), yielding:

$$\hat{\mathbf{a}}_i = \left(\prod_{k=1}^{i} A_k \right)^T \hat{\mathbf{g}} - \sum_{j=1}^{i} \left(\left(\prod_{k=j+1}^{i} A_k \right)^T \left(\boldsymbol{\psi}_j \hat{\boldsymbol{\beta}}_j^{A} - \hat{\mathbf{C}}_j - D_j \right) \right) \tag{4.33}$$

where:

$$D_i = \hat{\boldsymbol{\phi}}_i M_i^{-1} \boldsymbol{\tau}_{i-1}^{*} \tag{4.34}$$

Comparing (4.33) with (4.17), one can see that the former is far more complex and has, considerably, more terms. Evaluating (4.33) on the contacting link and replacing the articulated-body force bias by (4.32), results (4.35):

$$\hat{\mathbf{a}}_{n_c} = \left(\prod_{k=1}^{n_c} A_k \right)^T \hat{\mathbf{g}} - \sum_{j=1}^{n_c} \left(\left(\prod_{k=j+1}^{n_c} A_k \right)^T \left(\boldsymbol{\psi}_j \left(\sum_{l=j}^{n} \left(\left(\prod_{k=j+1}^{l} A_k \right) (B_l) \right) + \left(\prod_{k=j+1}^{n_c} A_k \right) \hat{\boldsymbol{\beta}}_{n_c}^{c} \right) - \hat{\mathbf{C}}_j - D_j \right) \right) \tag{4.35}$$

After heavy mathematical manipulation, (4.35) can be simplified and regain the recursivity, (4.36).

$$\hat{\mathbf{a}}_{n_c} = \left(\prod_{k=1}^{n_c} A_k \right)^T \hat{\mathbf{g}} - \Psi_{n_c} U_{n_c} - \Psi_{n_c} \hat{\boldsymbol{\beta}}_{n_c}^{c} - A_{n_c}^T \Gamma_{n_c-1} (\psi L - C - D) \tag{4.36}$$

where $\Gamma_i(f)$ is a recursive functional defined by (4.37), U_i and L_i are defined by (4.38) and (4.39), respectively:

$$\Gamma_i(f) = A_i^T \Gamma_{i-1}(f) + f_i \tag{4.37}$$

$$U_i = B_i + A_{i+1} U_{i+1} \tag{4.38}$$

$$L_{i-1} = B_{i-1} + A_i L_i \tag{4.39}$$

and $U_{n_c} = B_{n_c}$, $L_{n_c-1} = B_{n_c-1}$.

Pre-multiplying (4.36) by the transpose of the normal spatial vector and by $\hat{\mathbf{X}}_{n_C}^{\mathbf{r}^C}$, and knowing that the normal component of the acceleration is zero, one gets (4.40):

$$\hat{\mathbf{n}}_{n_C}^T \hat{\mathbf{X}}_{n_C}^{\mathbf{r}^C} \left(\left(\prod_{k=1}^{n_c} A_k \right)^T \hat{\mathbf{g}} + \Psi_{n_c} U_{n_c} + A_{n_c}^T \Gamma_{n_c-1} \left(\psi L - C - D \right) \right) = -\hat{\mathbf{n}}_{n_C}^T \hat{\mathbf{X}}_{n_C}^{\mathbf{r}^C} \Psi_{n_c} \hat{\boldsymbol{\beta}}_{n_c}^c \tag{4.40}$$

Replacing the contact spatial force bias with (4.29) and solving for the contact force norm, (4.40) becomes (4.41):

$$\left\| \hat{\mathbf{F}}_c \right\| = \frac{\hat{\mathbf{n}}_{n_C}^T \hat{\mathbf{X}}_{n_C}^{\mathbf{r}^C} \left(\left(\prod_{k=1}^{n_c} A_k \right)^T \hat{\mathbf{g}} - \Psi_{n_c} U_{n_c} - A_{n_c}^T \Gamma_{n_c-1} \left(\psi L - C - D \right) \right)}{\hat{\mathbf{n}}_{n_C}^T \hat{\mathbf{X}}_{n_C}^{\mathbf{r}^C} \Psi_{n_c} \left(\hat{\mathbf{X}}_{n_C}^{\mathbf{r}^C} \right)^T \hat{\mathbf{n}}_{n_C}} \tag{4.41}$$

4.2.2. Multiple Contacts

Multiple contacts have a similar effect on the contact force expression as simultaneous impacts have on the impact impulse. However, on the contact force case, this effect is stronger, because of the increased complexity and because, unlike impacts, contacts can start to accumulate over time, increasing even further the size of the system to be solved.

Repeating the simplifications done to (4.35) but considering multiple $\hat{\boldsymbol{\beta}}_{n_c}^c$, one obtains the following system of equations, (4.42):

$$\begin{bmatrix} \hat{\mathbf{a}}_{c_1} \\ \hat{\mathbf{a}}_{c_2} \\ \vdots \end{bmatrix} = \begin{bmatrix} \left(\prod_{k=1}^{c_1} A_k\right)^T \hat{\mathbf{g}} - \Psi_{c_1} U_{c_1} - A_{c_1}^T \Gamma_{c_1-1}\left(\psi L - C - D\right) \\ \left(\prod_{k=1}^{c_2} A_k\right)^T \hat{\mathbf{g}} - \Psi_{c_2} U_{c_2} - A_{c_2}^T \Gamma_{c_2-1}\left(\psi L - C - D\right) \\ \vdots \end{bmatrix} - \begin{bmatrix} \Psi_{c_1} & \Psi_{c_1}\left(\prod_{k=c_1+1}^{c_2} A_k\right) & \cdots \\ \left(\prod_{k=c_1+1}^{c_2} A_k\right)^T \Psi_{c_1} & \Psi_{c_2} & \cdots \\ \vdots & \vdots & \ddots \end{bmatrix} \begin{bmatrix} \hat{\boldsymbol{\beta}}_{c_1}^c \\ \hat{\boldsymbol{\beta}}_{c_2}^c \\ \vdots \end{bmatrix} \tag{4.42}$$

Again pre-multiplying the system by the normal spatial vectors and by the transformations, and knowing that the normal components of the accelerations are zero, (4.42) becomes (4.43):

$$\begin{bmatrix} \hat{\mathbf{n}}_{c_1}^T \hat{\mathbf{X}}_{c_1}^{\mathbf{r}^C} \left(\left(\prod_{k=1}^{c_1} A_k\right)^T \hat{\mathbf{g}} - \Psi_{c_1} U_{c_1} - A_{c_1}^T \Gamma_{c_1-1}\left(\psi L - C - D\right) \right) \\ \hat{\mathbf{n}}_{c_2}^T \hat{\mathbf{X}}_{c_2}^{\mathbf{r}^C} \left(\left(\prod_{k=1}^{c_2} A_k\right)^T \hat{\mathbf{g}} - \Psi_{c_2} U_{c_2} - A_{c_2}^T \Gamma_{c_2-1}\left(\psi L - C - D\right) \right) \\ \vdots \end{bmatrix} = \begin{bmatrix} \hat{\mathbf{n}}_{c_1}^T \hat{\mathbf{X}}_{c_1}^{\mathbf{r}^C} \Psi_{c_1} \left(\hat{\mathbf{X}}_{c_1}^{\mathbf{r}^C}\right)^T \hat{\mathbf{n}}_{c_1} & \hat{\mathbf{n}}_{c_1}^T \hat{\mathbf{X}}_{c_1}^{\mathbf{r}^C} \Psi_{c_1} \left(\prod_{k=c_1+1}^{c_2} A_k\right) \left(\hat{\mathbf{X}}_{c_2}^{\mathbf{r}^C}\right)^T \hat{\mathbf{n}}_{c_2} & \cdots \\ \hat{\mathbf{n}}_{c_2}^T \hat{\mathbf{X}}_{c_2}^{\mathbf{r}^C} \left(\prod_{k=c_1+1}^{c_2} A_k\right)^T \Psi_{c_1} \left(\hat{\mathbf{X}}_{c_1}^{\mathbf{r}^C}\right)^T \hat{\mathbf{n}}_{c_1} & \hat{\mathbf{n}}_{c_2}^T \hat{\mathbf{X}}_{c_2}^{\mathbf{r}^C} \Psi_{c_2} \left(\hat{\mathbf{X}}_{c_2}^{\mathbf{r}^C}\right)^T \hat{\mathbf{n}}_{c_2} & \cdots \\ \vdots & \vdots & \ddots \end{bmatrix} \begin{bmatrix} \hat{\boldsymbol{\beta}}_{c_1}^c \\ \hat{\boldsymbol{\beta}}_{c_2}^c \\ \vdots \end{bmatrix} \tag{4.43}$$

Note that the system matrix of (4.43) is equal to the system matrix of the simultaneous impacts system, (4.28).

Chapter 5

SIMULATION RESULTS

The implementation of the Articulated-Body Algorithm and its Impact version was done using the paradigm of Object Oriented programming in C++ and C#. The core algorithm was programmed exclusively in C++, which brings two main advantages. The first is the platform independence, because computer programs coded in ANSI C++ can be compiled and, consequently, executed in any operating system and on any kind of CPU (Central processing Unit), and the second advantage are the class type of C++. The utilization of classes simplifies the code and, in most cases, can give a physical meaning to the variables of the program: each link-joint pair is represented by an instance of the Link class, which can, subsequently, be connected to other instances of the same class, creating the structure to be simulated.

The simulation software, when run in windows, also has a simple GUI (graphical user interface) programmed in C# and DirectX (Microsoft's library for 3D graphics).

The algorithms were tested using three simple tests, each one testing a particular aspect:

- A pendulum and a five-link structure, as a simple serial structures;
- Impact simulation with an inverted double pendulum;
- A 10-link "Y" tree structure, with and without external torques.

The last two tests were done using the human hand model in the simplest configuration and the final model with elasticity on the joints and joint limits.

5.1. Simple Serial Structures

5.1.1. Simple Pendulum

The simple planar pendulum, Fig. 5-1, is one of the few articulated structures with an analytical solution (although one can also write the differential equation system for more complex pendulums, the solutions become too difficult to reach).

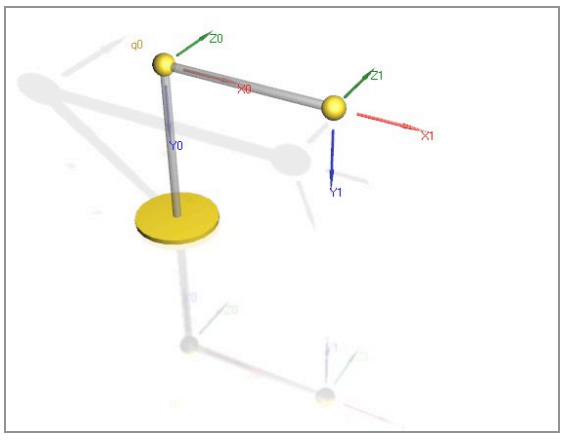

Fig. 5-1 Simple pendulum.

The differential equation that describes the movement of the pendulum is given by (5.1):

$$\frac{1}{6}m\left(l^2+3r^2\right)\ddot{\theta}-mgl\sin(\theta)=0 \qquad (5.1)$$

where m, l and r are the rigid link mass, length and radius, respectively. g is the gravity and θ is the angle.

Solving the differential equation, one gets the following results:

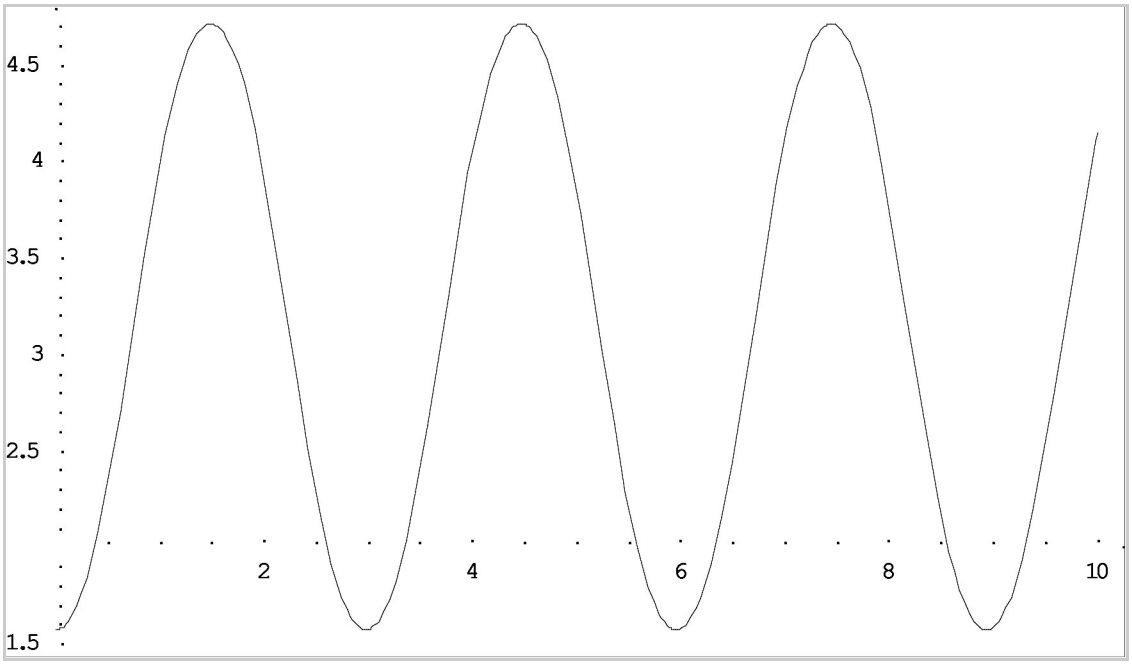

Fig. 5-2 Analytical Joint Position.

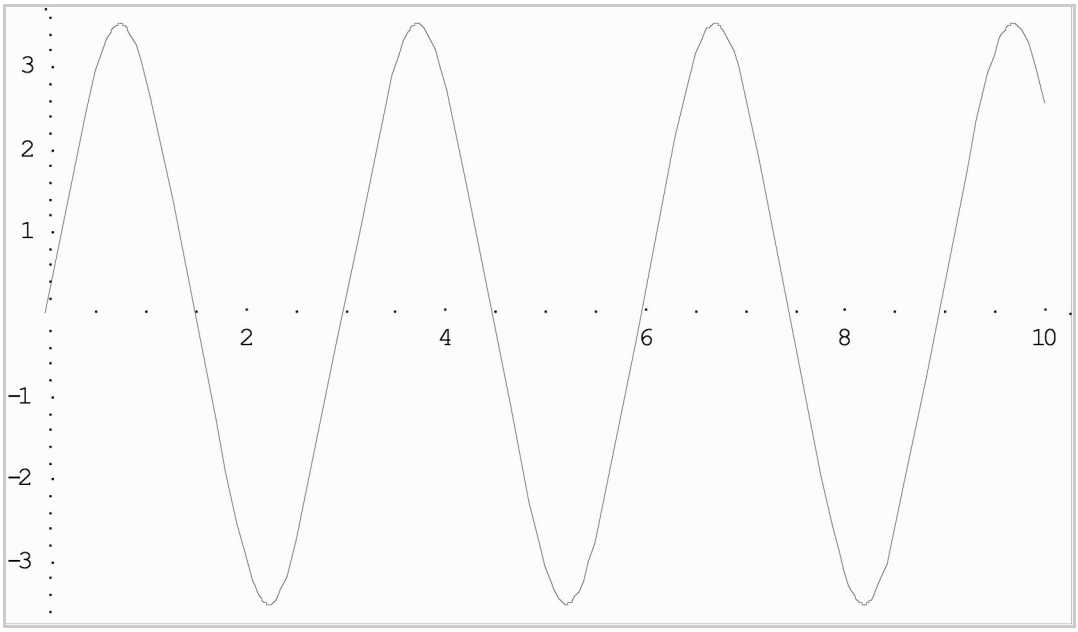

Fig. 5-3 Analytical Joint Velocity.

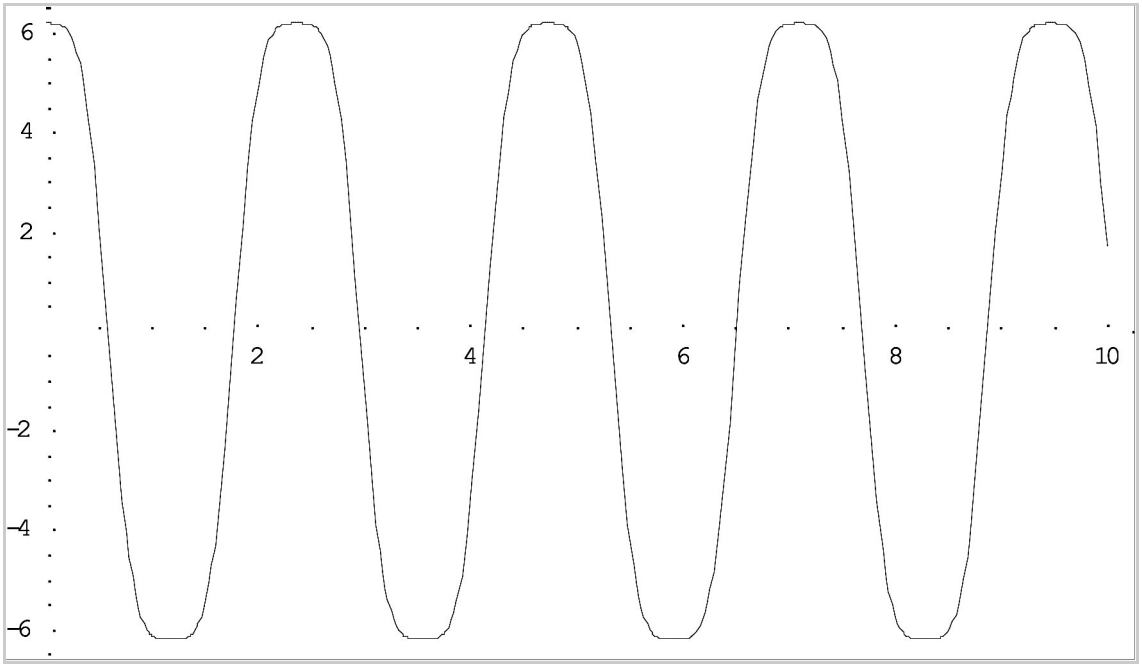

Fig. 5-4 Analytical Joint Acceleration.

The initial conditions are:

$$\theta = \frac{\pi}{2}$$
$$\dot{\theta} = 0$$

Using the ABA to solve the same problem, one gets the following results for the joint position, velocity and acceleration:

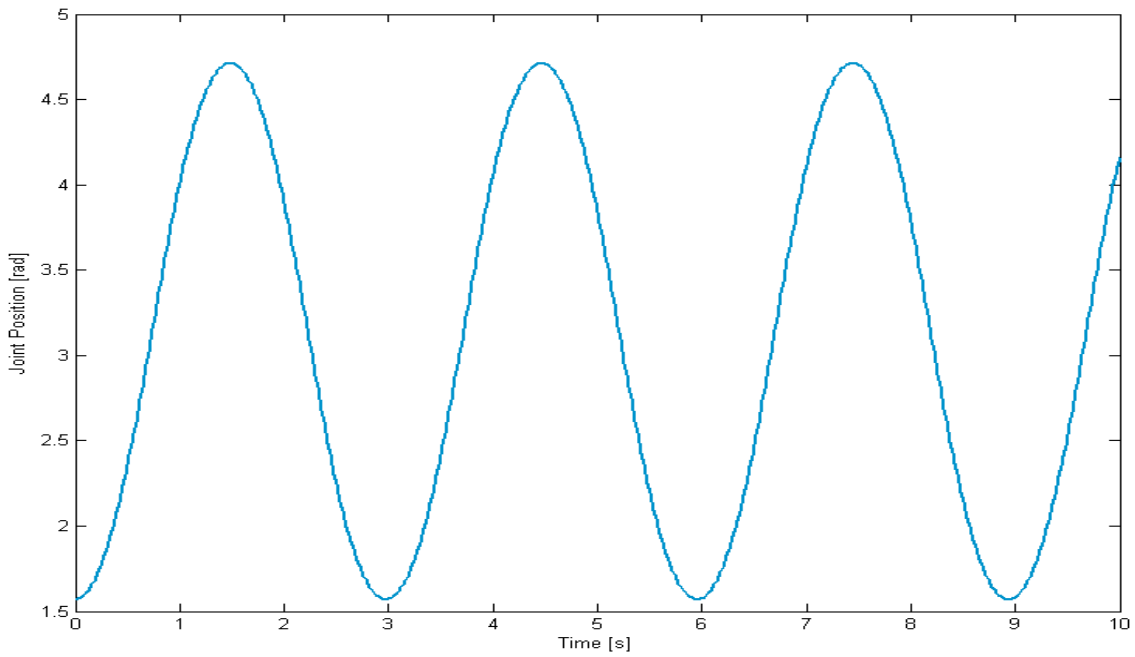

Fig. 5-5 Simple pendulum joint position.

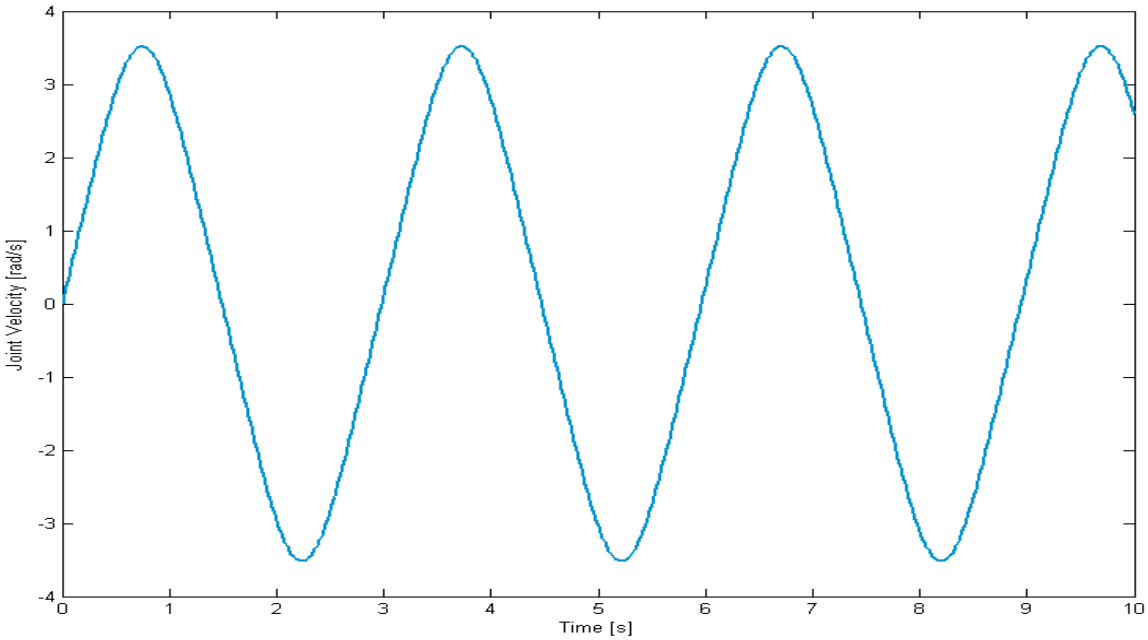

Fig. 5-6 Simple pendulum joint velocity

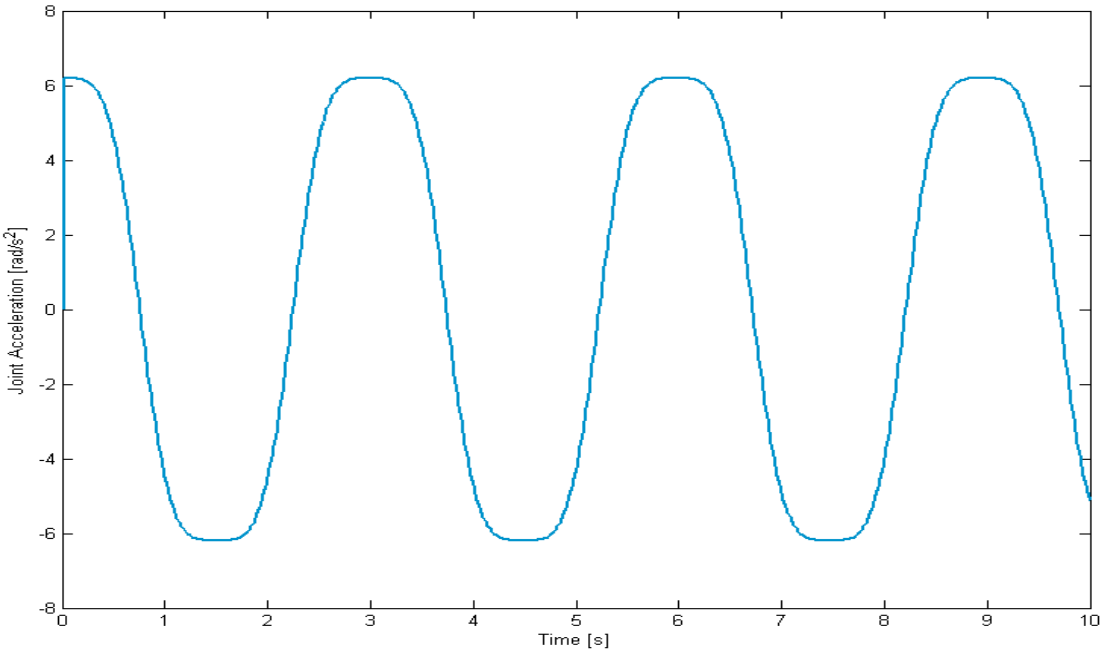

Fig. 5-7 Simple pendulum joint acceleration.

As expected the results taken from the ABA simulation are similar to the order of the 10^{-5}% to the ones taken from the analytical solution.

5.1.2. Five-link serial structure

A six-link serial structure, Fig. 5-8, is, already, too complex to be solved analytically.

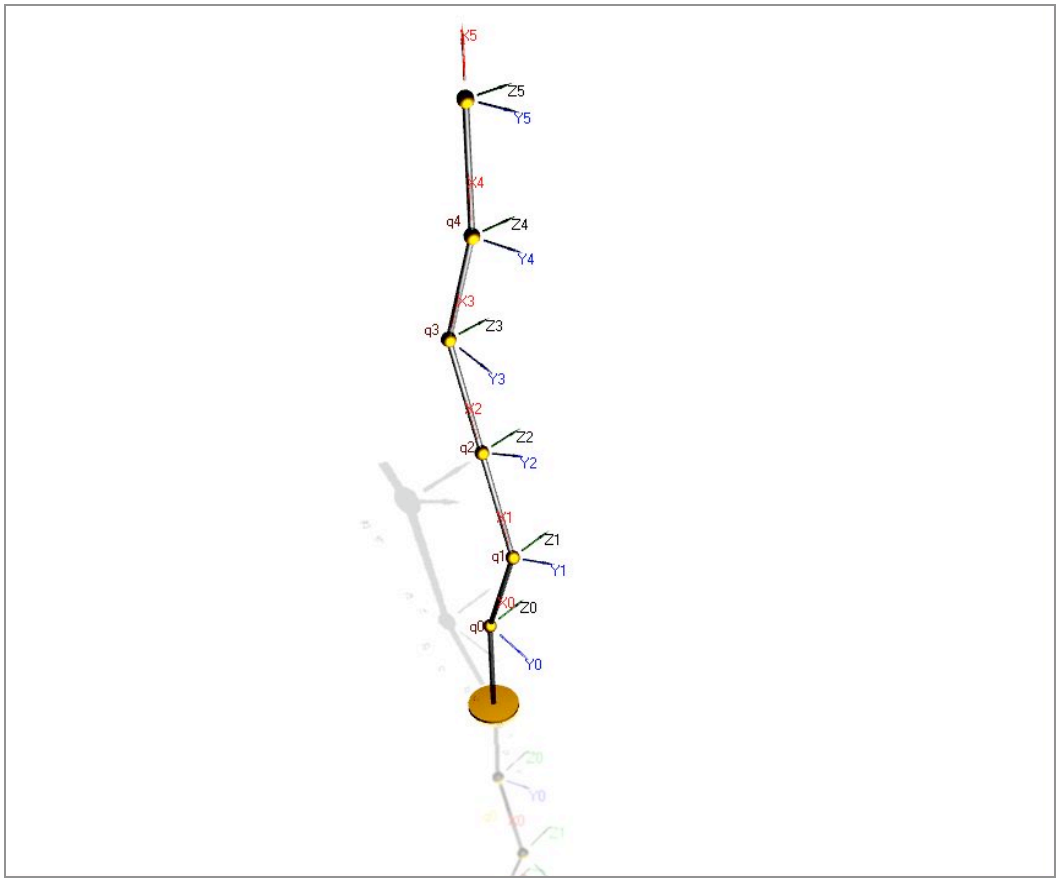

Fig. 5-8 5-link serial structure.

The simulation with the ABA was done using dampened joints with a dampening coefficient of 3N.s, and with the initial conditions shown in Fig. 5-8 and Table 5-I.

Table 5-I Initial positions (in radians) for the six-link structure

Joint 1	Joint 2	Joint 3	Joint 4	Joint 5
$\frac{\pi}{10}$	$-\frac{2\pi}{10}$	0	$\frac{2\pi}{10}$	$-\frac{\pi}{10}$

Screenshots of the simulation are shown in Fig. 5-9 and the plot of the joint positions in Fig. 5-10. The velocities and accelerations are on the Appendixes.

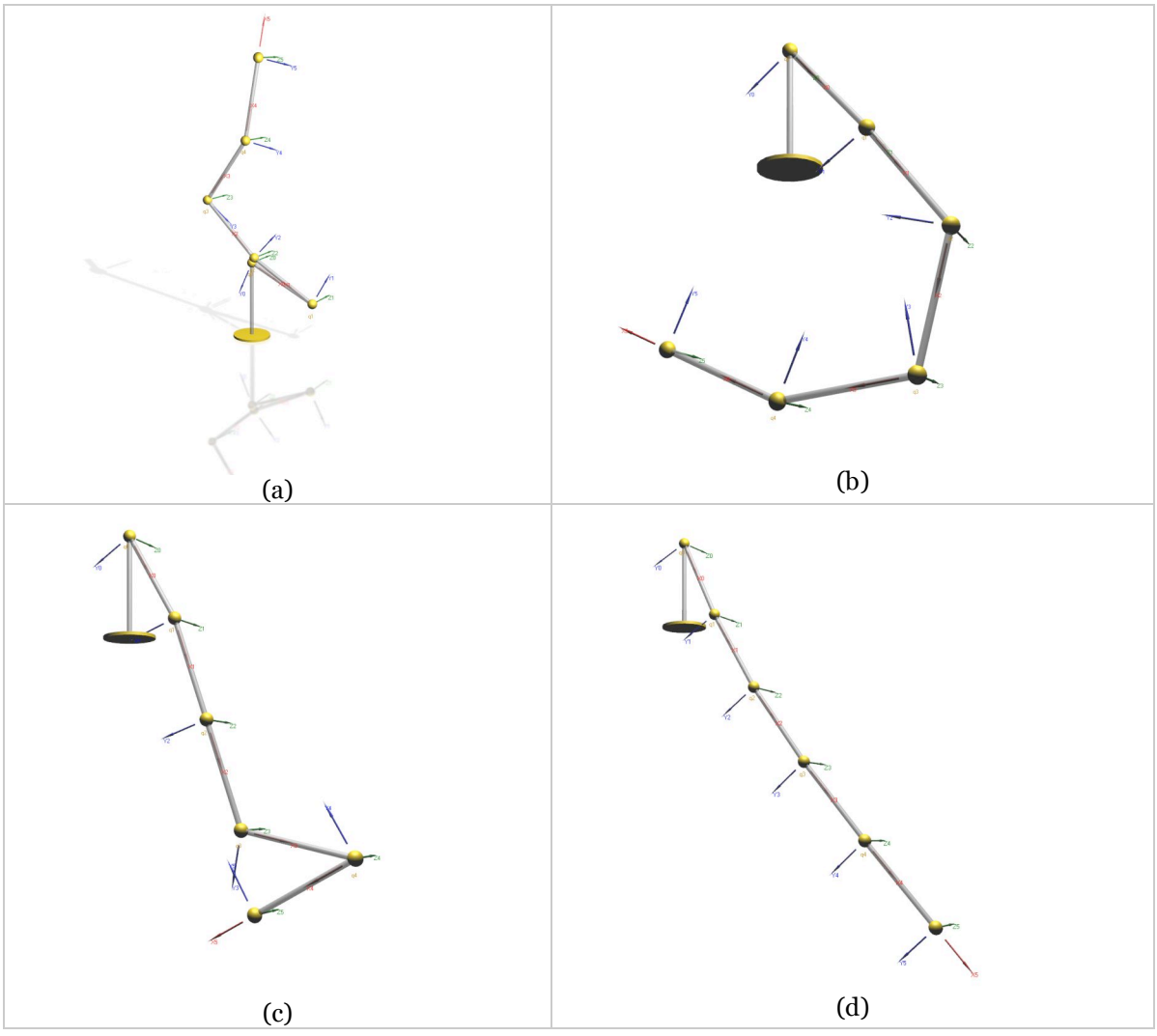

Fig. 5-9 Screenshots of the simulation at t = 1s (a), t = 2.5s (b), t = 4s (c), t = 9s (d).

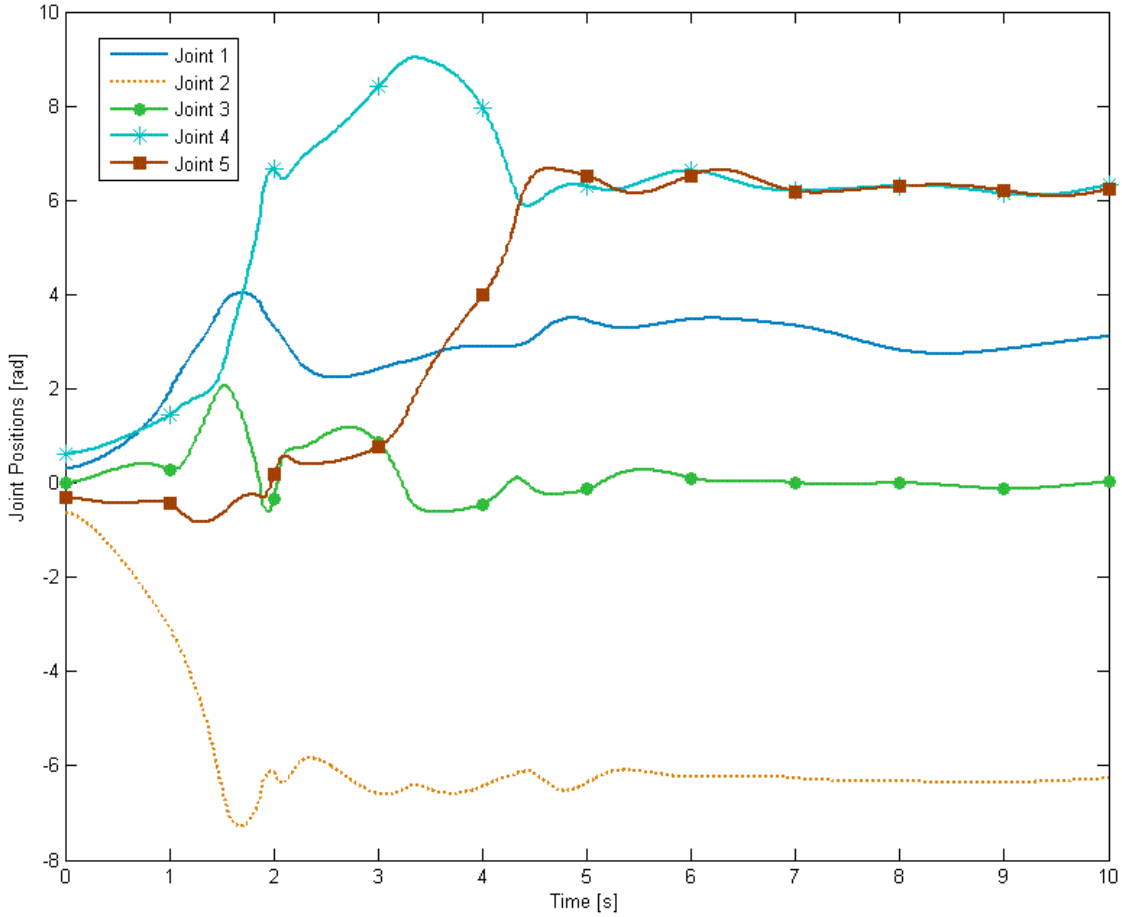

Fig. 5-10 Joint positions for the five-link structure.

5.2. Inverted Double Pendulum

The inverted planar double pendulum, depicted in Fig. 5-11, was used to test the impact algorithm.

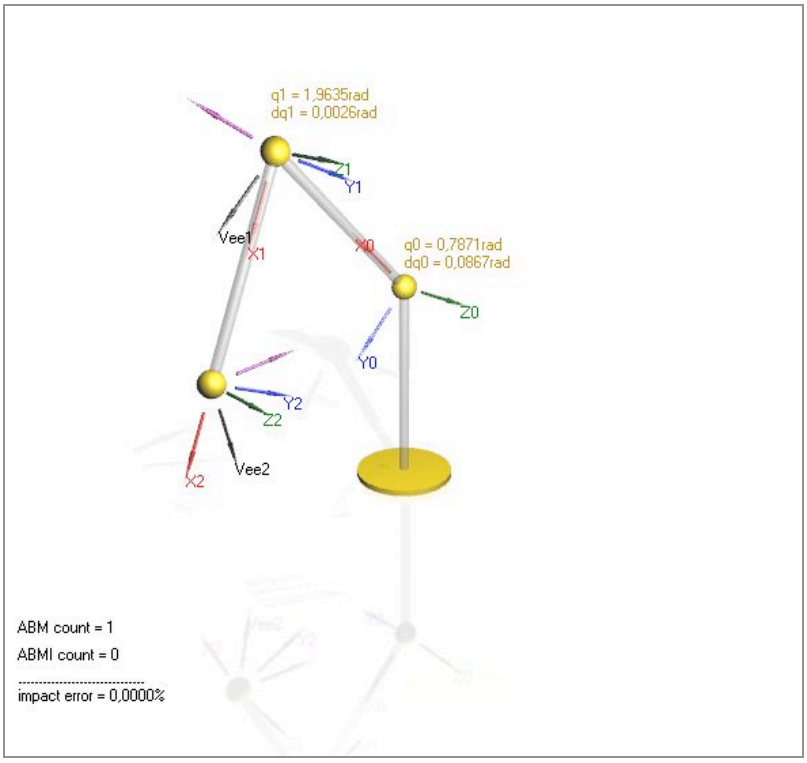

Fig. 5-11 Inverted double pendulum.

All links have the same length and, consequently, only the tip of the end-effector can touch the ground. The coefficient of restitution is 1, denoting a fully elastic collision and the initial positions are 45 degrees and 112.5 degrees, for the first and second joints, respectively. The plots in Fig. 5-12, Fig. 5-13, and Fig. 5-14 give the results for the joint positions, joint velocities, and joint accelerations, respectively.

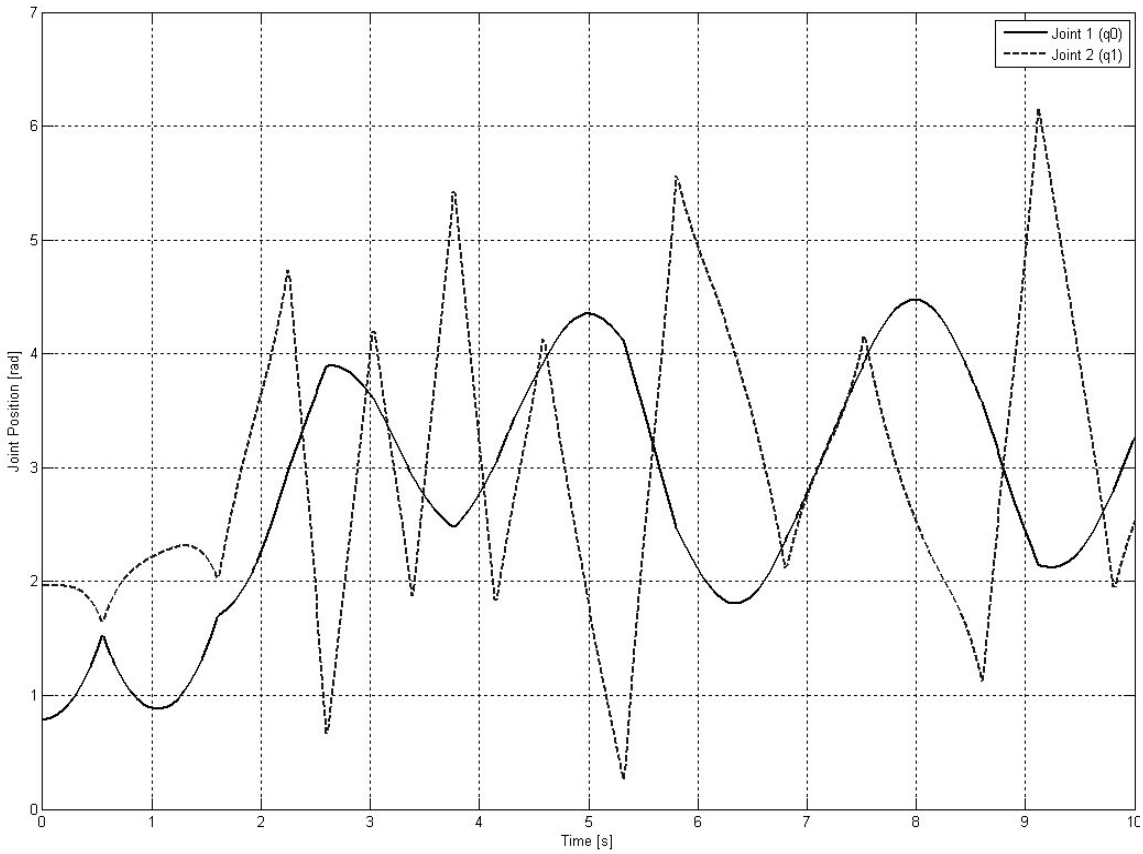

Fig. 5-12 Joint positions of the double pendulum.

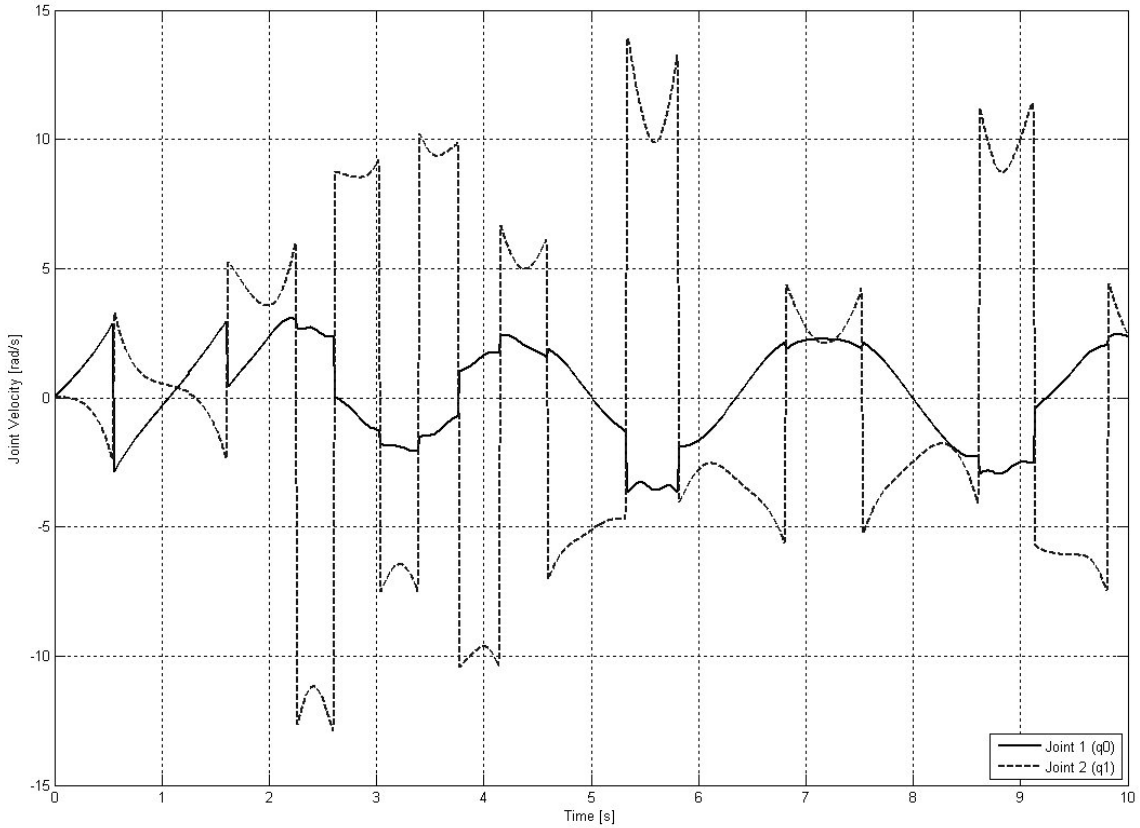

Fig. 5-13 Joint velocities of the double pendulum.

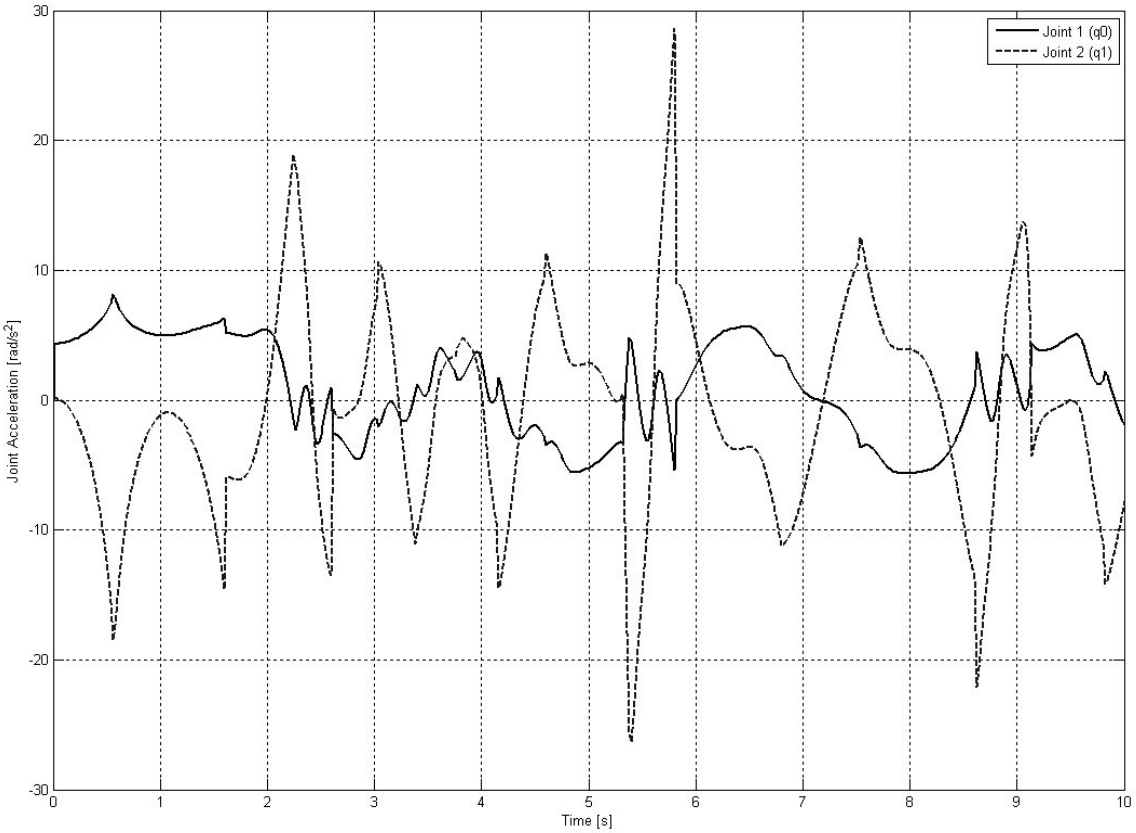

Fig. 5-14 Joint accelerations of the double pendulum.

From Fig. 5-13 we can see the discontinuities in the velocities marking each impact. The amplitude of the discontinuities is connected to the restitution coefficient. If we decrease the coefficient to half the movement becomes much more smooth, Fig. 5-15.

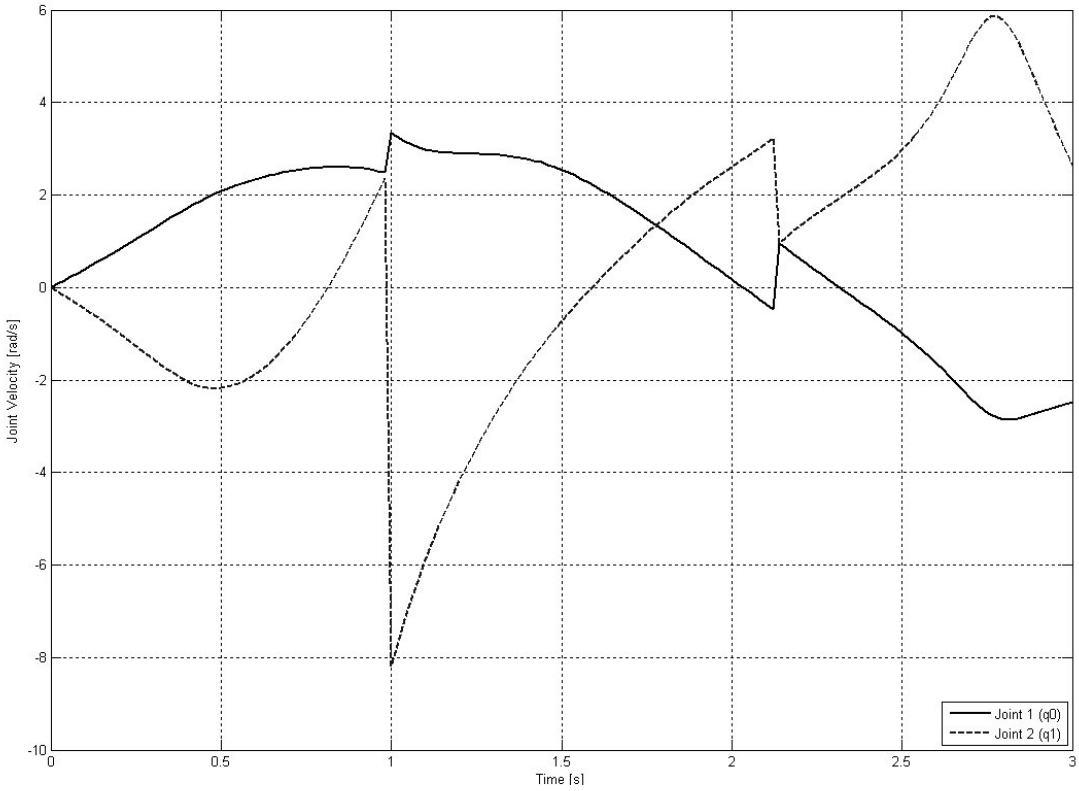

Fig. 5-15 Joint velocities for e = 0.5.

Analyzing the relative error between the impact velocity given by (4.22) and the impact velocities given by the algorithm, we get, for this case, an average of 0.001341%, Fig. 5-16.

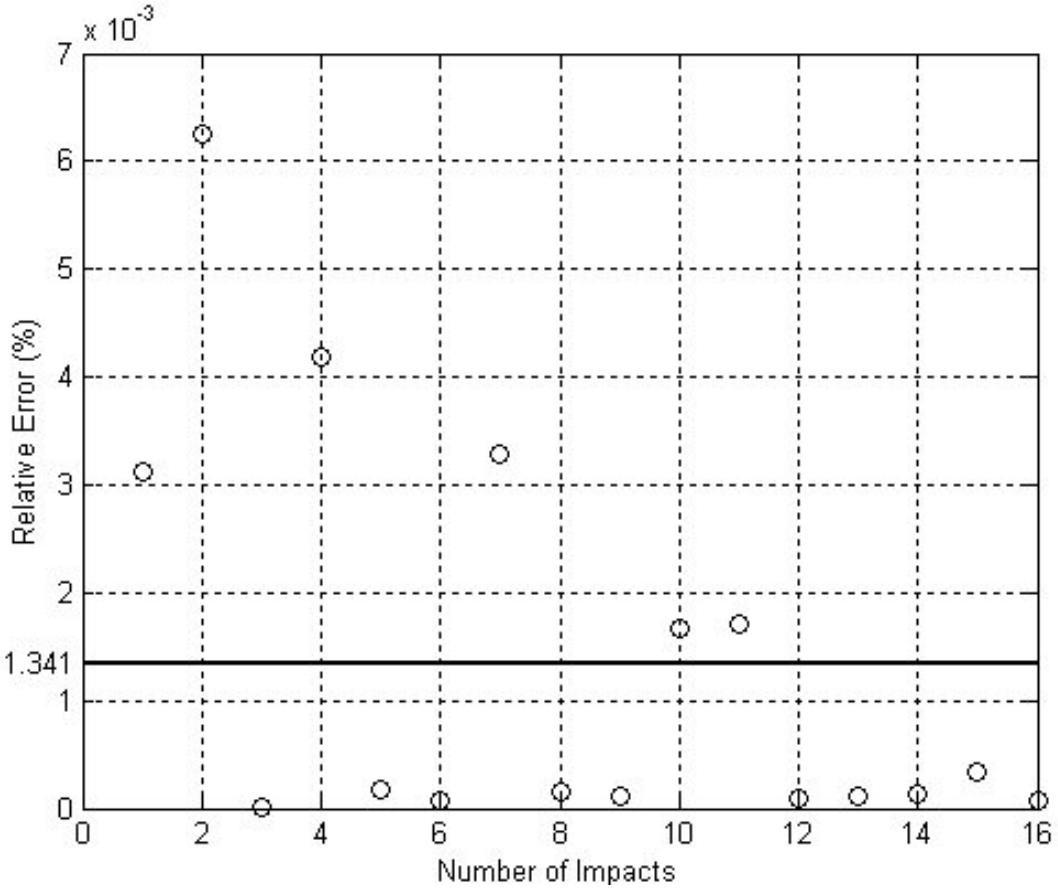

Fig. 5-16 Relative error of the impact velocities.

5.3. Simple Tree Structure

Tree structures have one added degree of complexity when compared to serial structures, because in this kind of structure the each link is not only affected the movements of the upper and lower links, but also by the links on other branches of the structure.

5.3.1. Ten-link "Y" tree structure in free fall

The first test with the eleven-link tree structure was performed much the same way the serial structure tests were done.

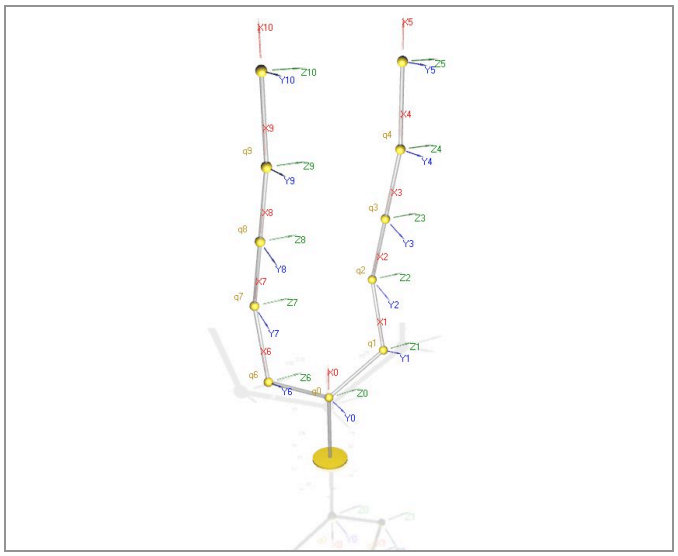

Fig. 5-17 10-link tree structure.

The initial positions of the joints are depicted in Fig. 5-17 and the initial status of the structure is described in Table 5-II.

Table 5-II 11-link tree structure initial positions.

Joint 1	Branch 1	Joint 2	Joint 3	Joint 4	Joint 5
		$-\frac{\pi}{10}$	$\frac{2\pi}{10}$	0	$-\frac{\pi}{10}$
0	Branch 2	Joint 6	Joint 7	Joint 8	Joint 9
		$-\frac{\pi}{10}$	$\frac{2\pi}{10}$	0	$-\frac{\pi}{10}$

The screenshots of the simulation are shown on Fig. 5-18 and the results for the joint positions, velocities and accelerations are on Fig. 5-19. Again the joint velocities and accelerations can be found in the Appendixes.

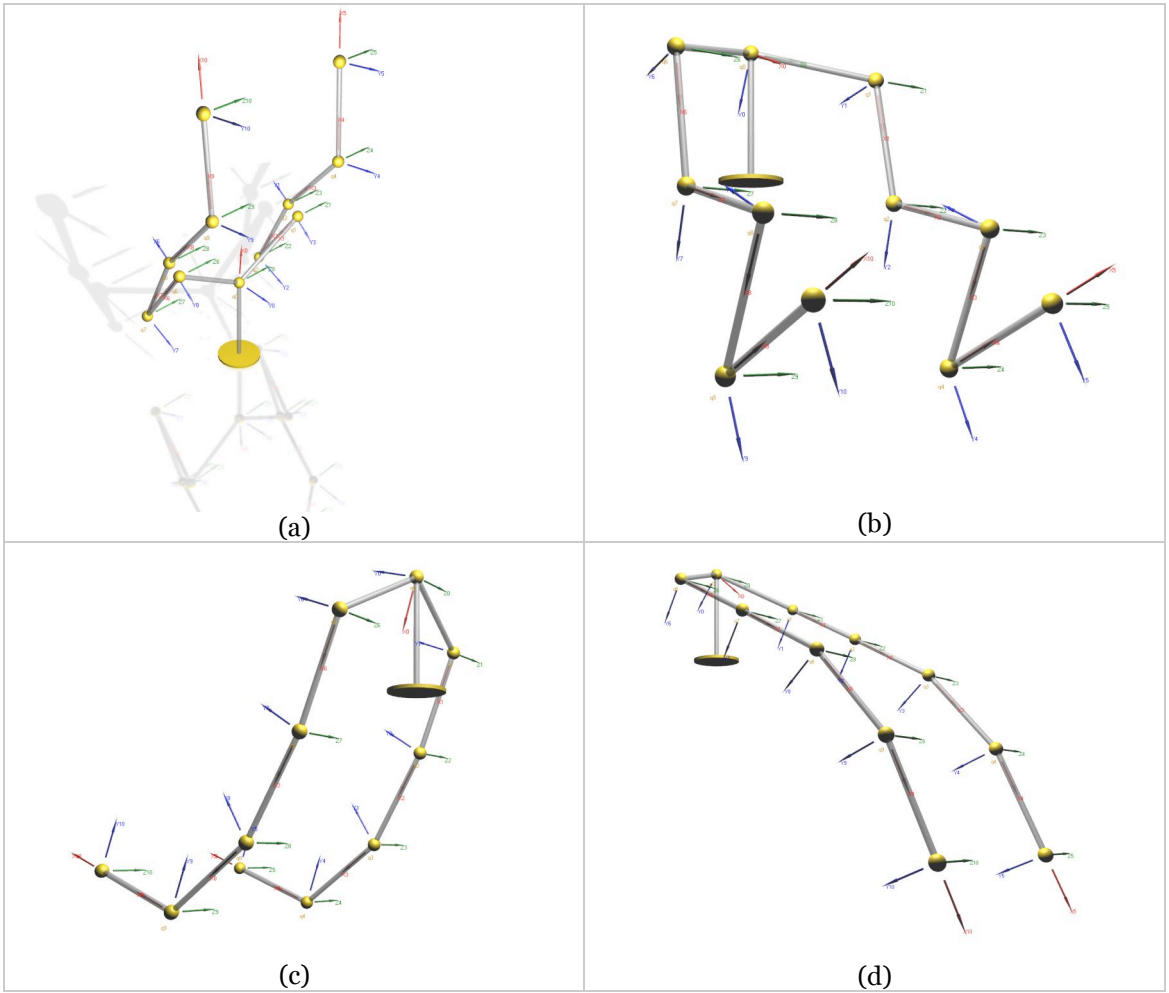

Fig. 5-18 Screenshots of the simulation at t = 1s (a), t = s (b), t = 5s (c), t = 7s (d).

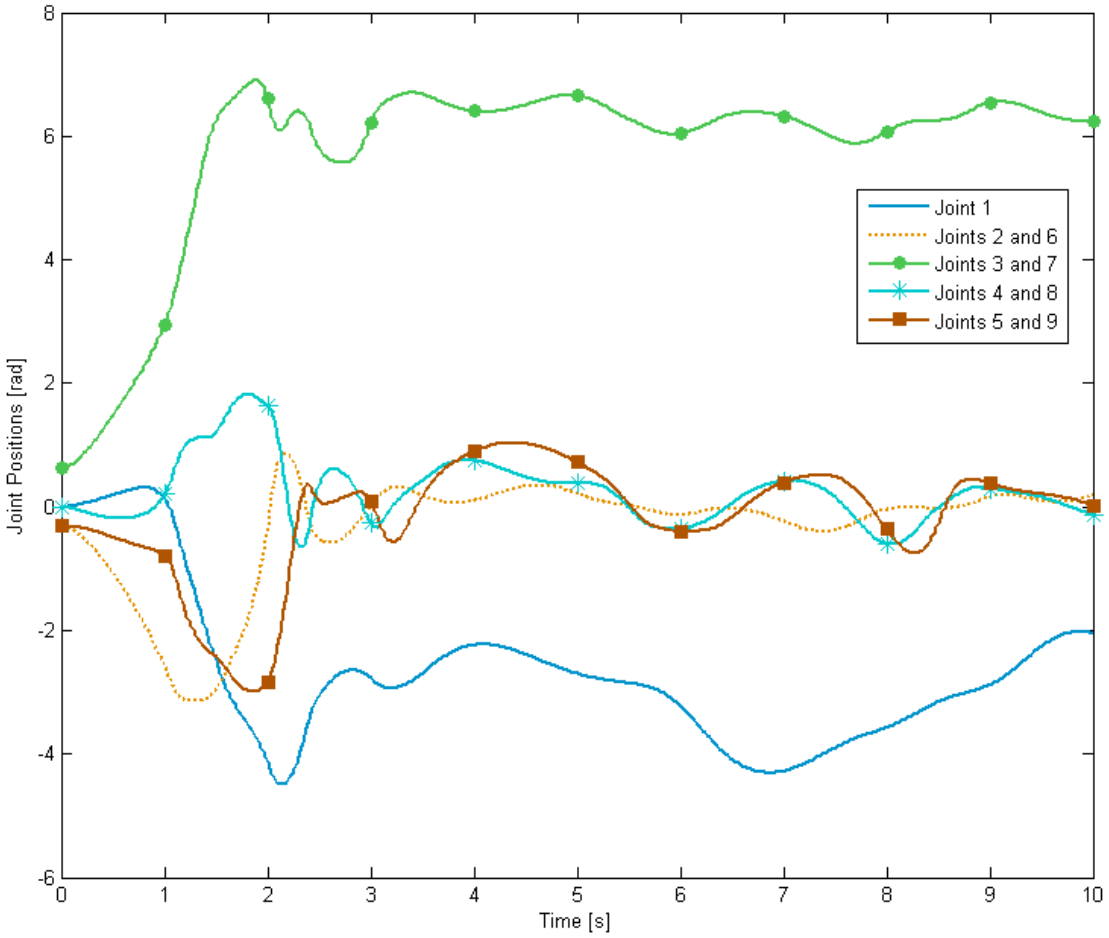

Fig. 5-19 Joint positions of the 11-link tree structure in free fall.

Because both the structure and the initial conditions are symmetric, the curves from the joints of the first branch (dashed curves) are superimposed by the ones from the second branch (solid curves).

Analyzing the joint positions, Fig. 5-19, one can see that, because of the dampening, the structure tends to go to the equilibrium position, with the branch joint going to 0 or 2π, and the first joint to π.

5.3.2. Ten-link tree structure with external torques

In this test, a set of external torques is applied to the 11-link structure, Fig. 5-17. The torques are different for each level and are given by:

$$\tau_i(t) = 20(n_l - n)\sin(t) \tag{5.2}$$

where n_l and n are the number of levels (five in this case) and the current level, respectively. Plotting (5.2), one gets the following torques:

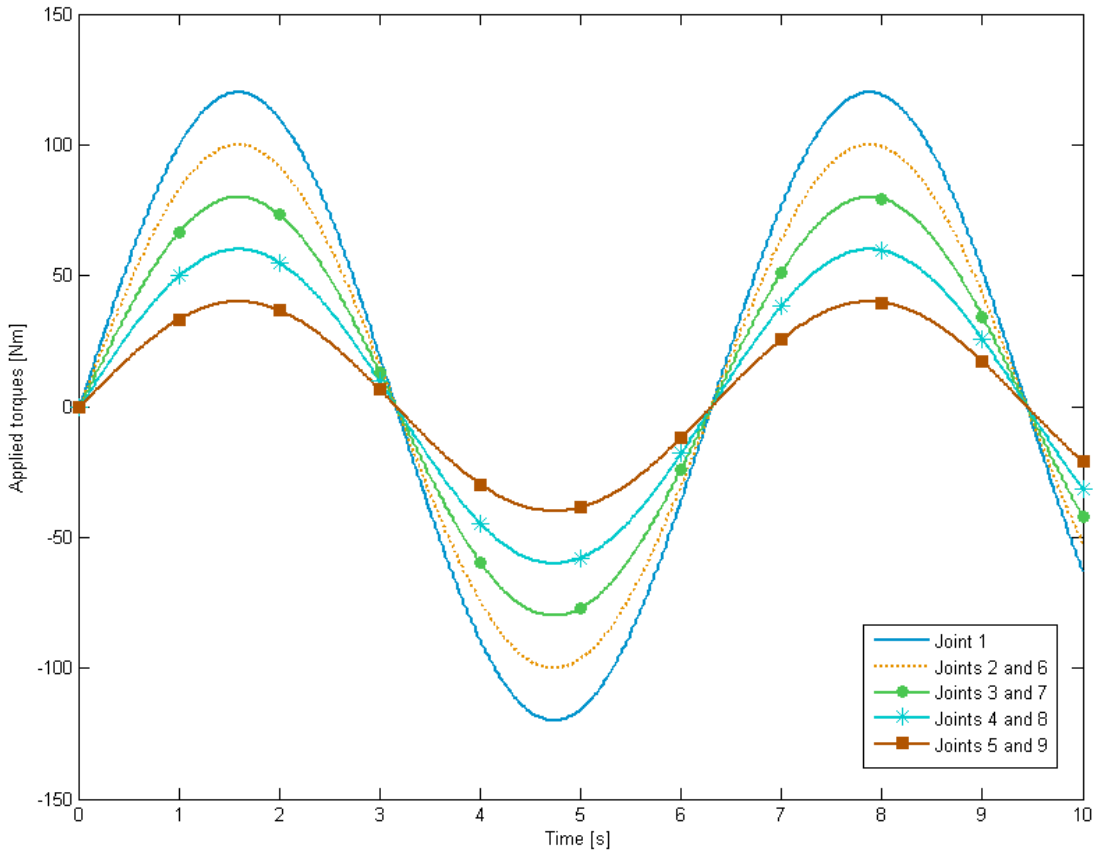

Fig. 5-20 Applied torques.

With the torques given by (5.2) and using the same initial conditions of the last test, Table 5-II, the structure moves as depicted on Fig. 5-21.

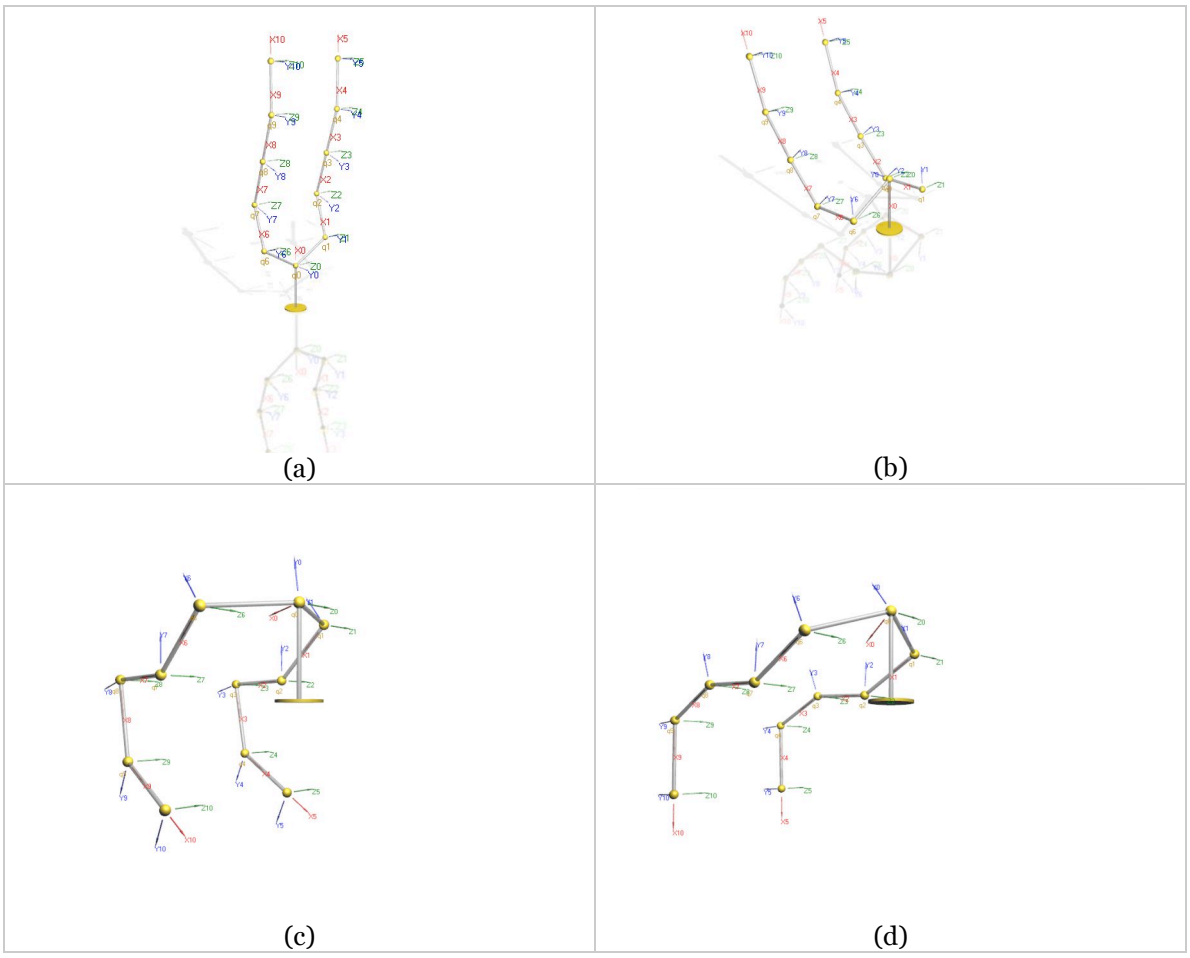

Fig. 5-21 Screenshots of the simulation at t = 0s (a), t = 2.5s (b), t = 5s (c), t = 10s (d).

Analyzing the joint positions, Fig. 5-22, it can be seen that the structure no longer goes to the equilibrium position, because the applied torques are constantly giving energy to the system. Again, because of the symmetry, the two branch curves are superimposed.

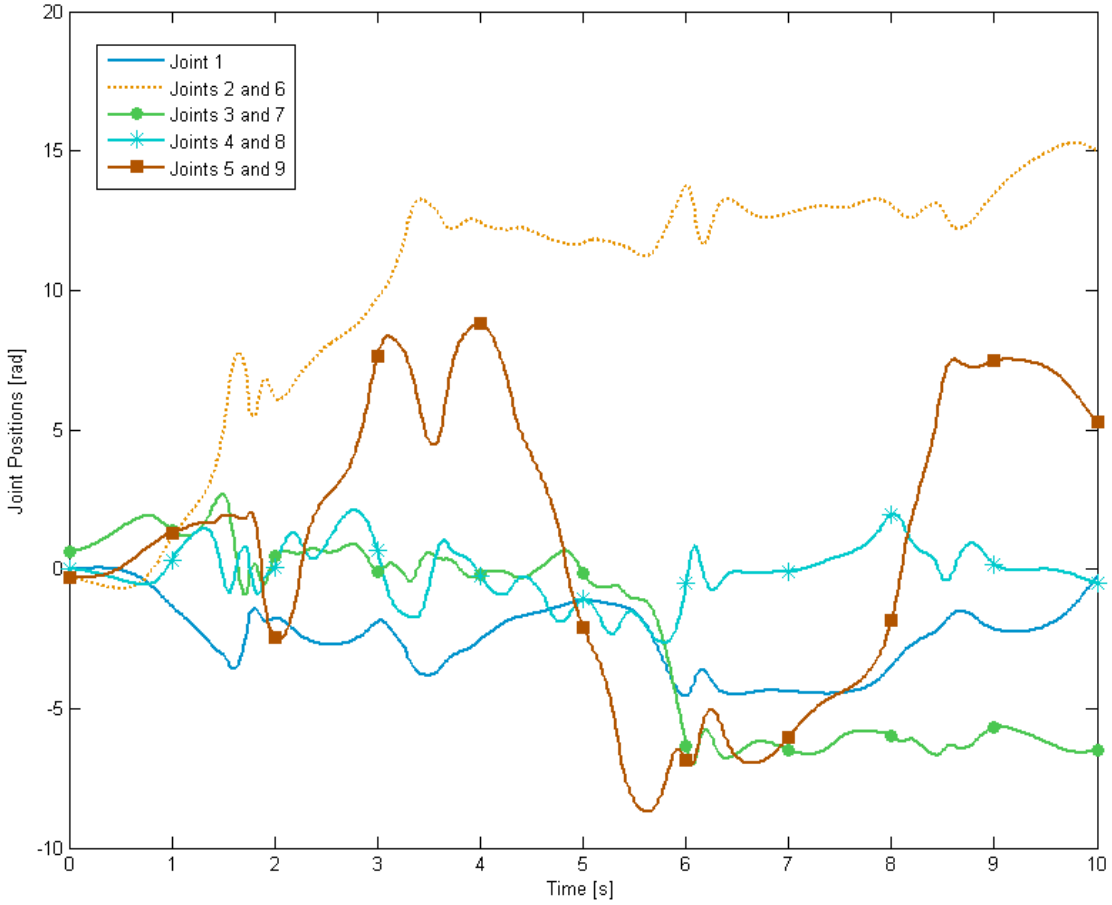

Fig. 5-22 Joint Positions of the 11-link tree structure with applied torques.

5.4. The Hand

5.4.1. Simple hand model in Dampened free fall.

The human hand was simulated using the structure depicted on Fig. 5-23.

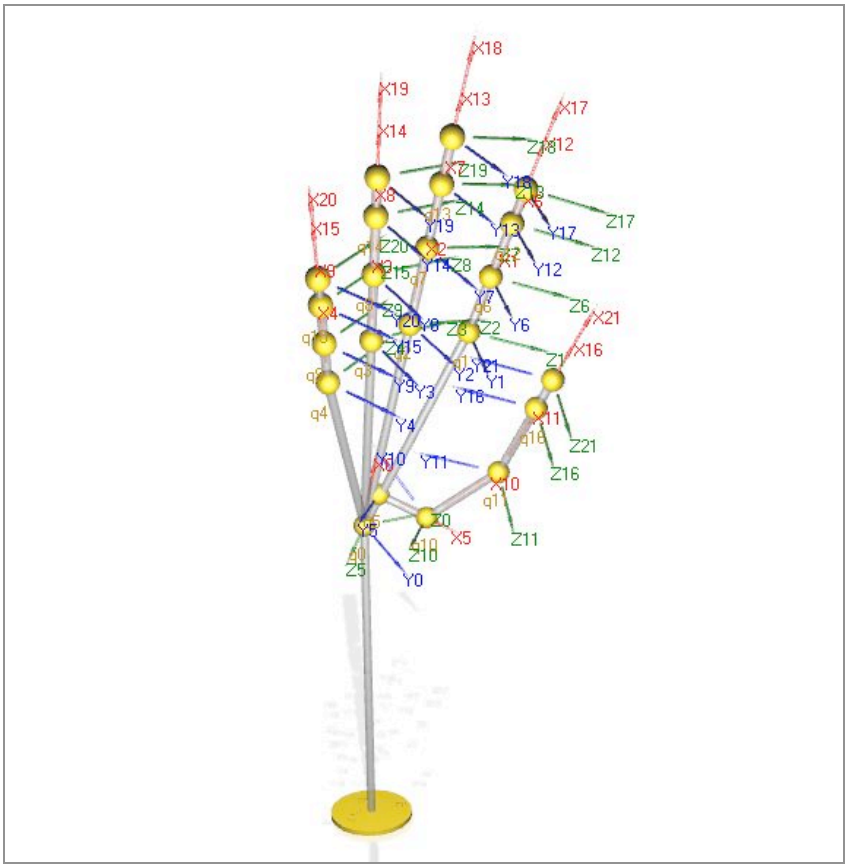

Fig. 5-23 Human Hand.

This, first, simulation of the hand was done with a constant dampening coefficient of 3N.s in every joint. There are no joint limits in this simulation and the initial positions are shown on Table 5-III.

Table 5-III Initial positions (in radians) of the hand model.

Joint	Joint Location	Initial position DoF 1	Initial position DoF 2
1	Wrist	$\frac{\pi}{32}$	$\frac{\pi}{10}$
2	Index MCP	0	0
3	Middle MCP	0	0
4	Ring MCP	0	0
5	Little MCP	0	0
6	Thumb CMC 1	$\frac{\pi}{4}$	–
7	Index PIP	0	–
8	Middle PIP	0	–
9	Ring PIP	0	–
10	Little PIP	0	–
11	Thumb CMC 2	$\frac{\pi}{3}$	–
12	Thumb MCP	$\frac{\pi}{6}$	–
13	Index DIP	0	–
14	Middle DIP	0	–
15	Ring DIP	0	–
16	Little DIP	0	–
17	Thumb IP	0	–

Note the CMC joint of the thumb was divided into two separate joints, because the MTC of the thumb does not have the same insertion point of the other MTC bones, Fig. 5-24.

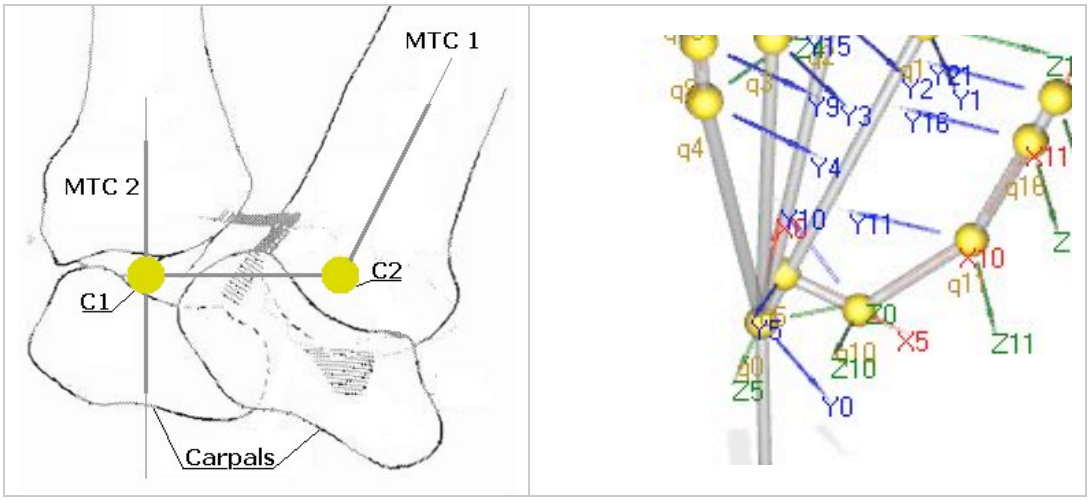

Fig. 5-24 Detail of the thumb CMC joint.

Also, the CMC joint of the little finger was removed, because this joint has little effect on the structure, it can only rotate approximately 5 degrees.

The screenshots obtained from the simulation are shown on Fig. 5-25, and the joint positions are plotted on Fig. 5-26 to Fig. 5-31.

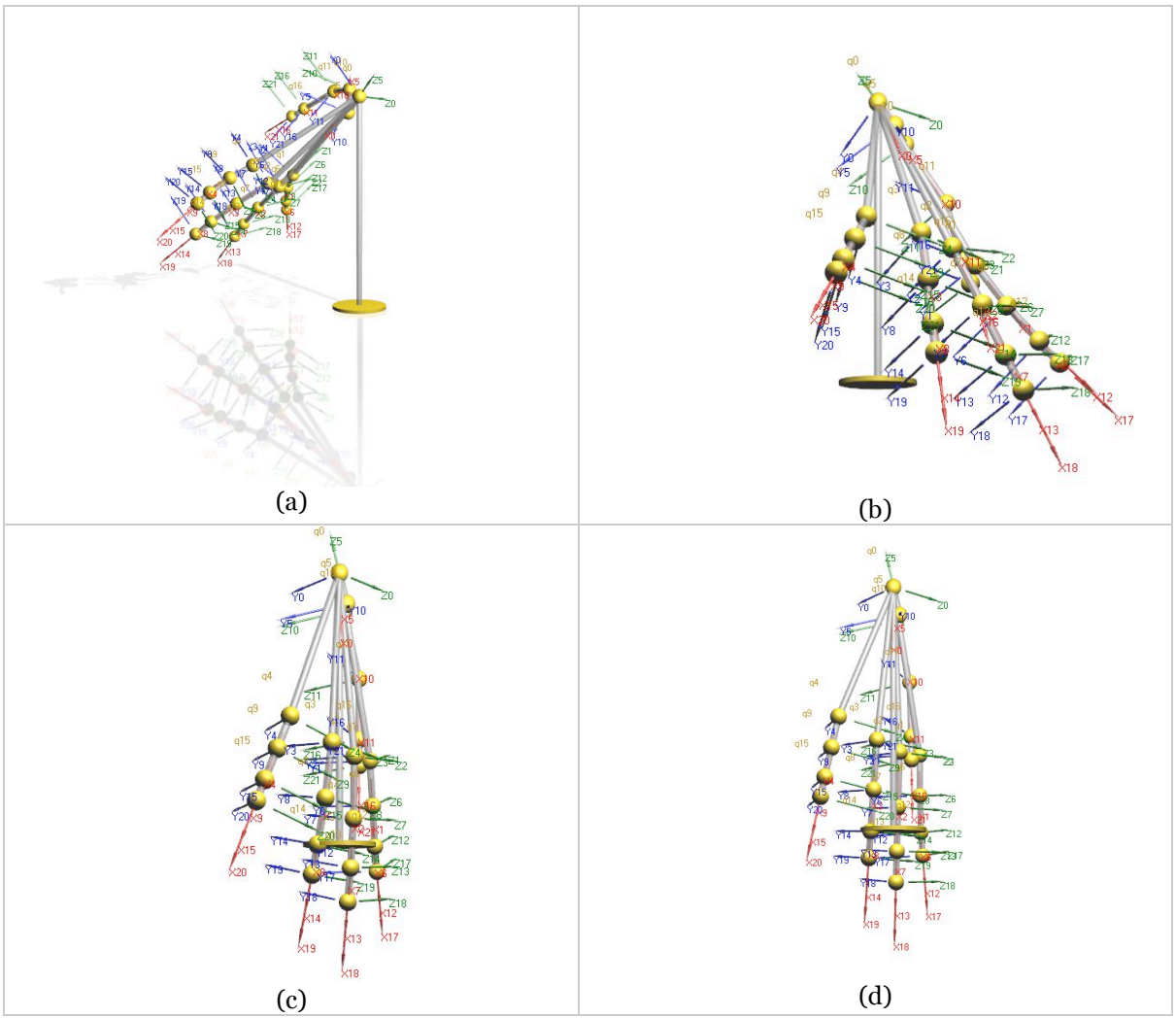

Fig. 5-25 Screenshots of the simulation at t = 2.5s (a), t = 5s (b), t = 7.5s (c), t = 10s (d).

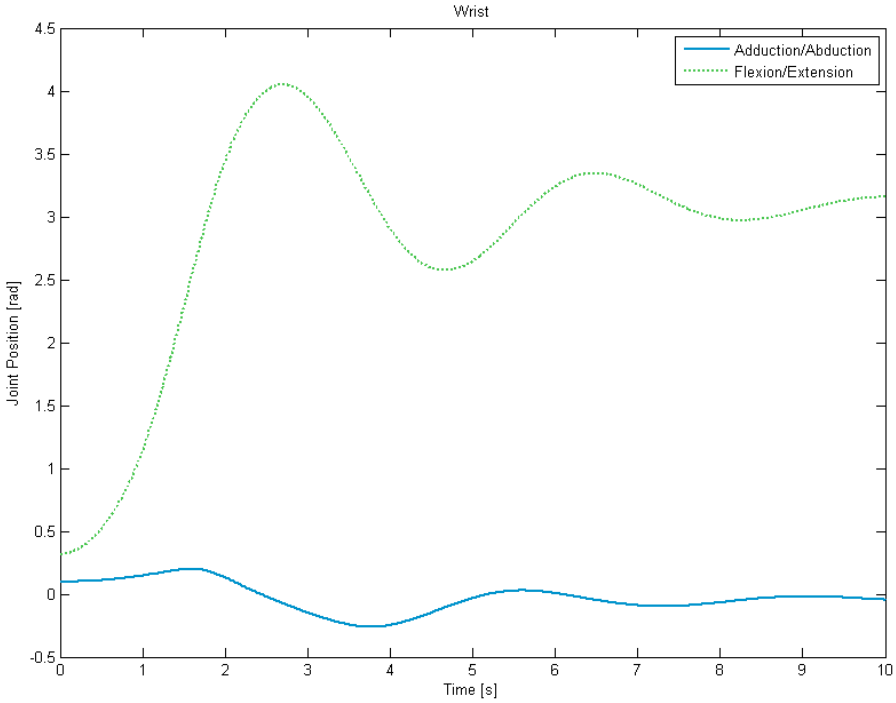

Fig. 5-26 Joint positions of the wrist.

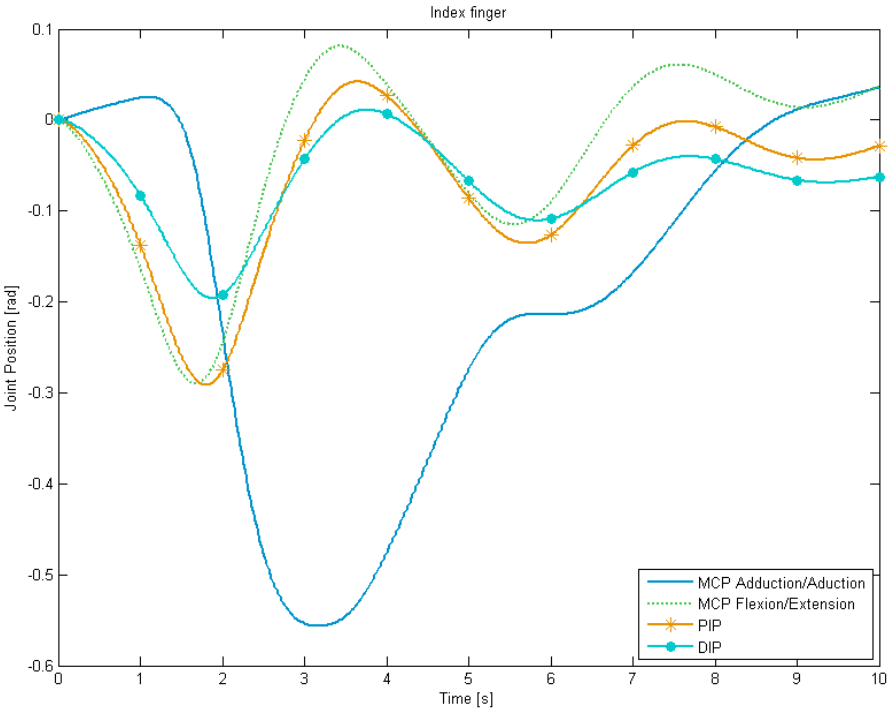

Fig. 5-27 Joint positions of the index finger.

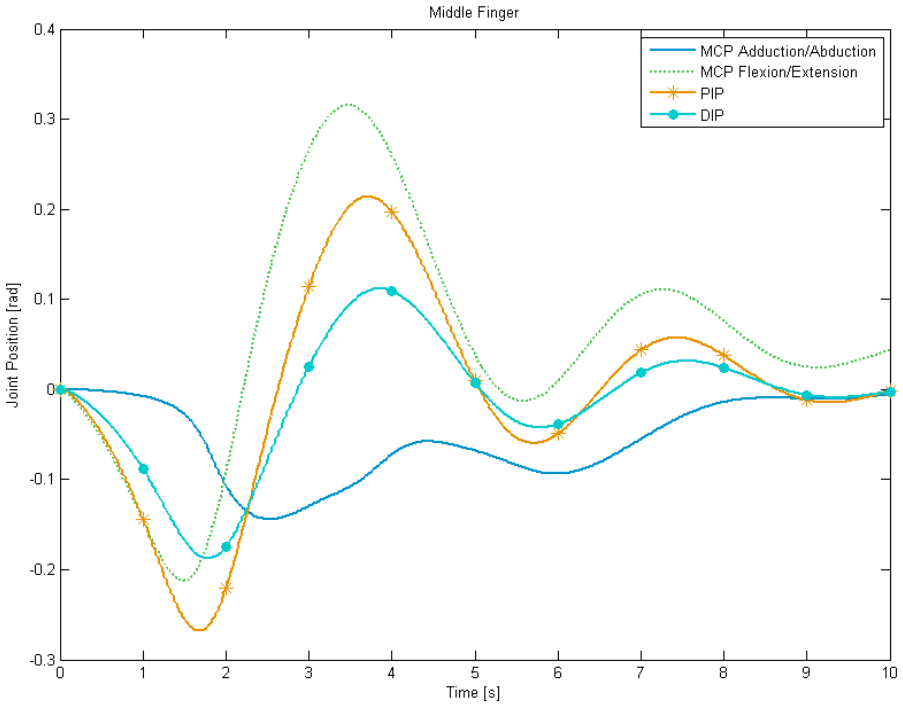

Fig. 5-28 Joint positions of the middle finger.

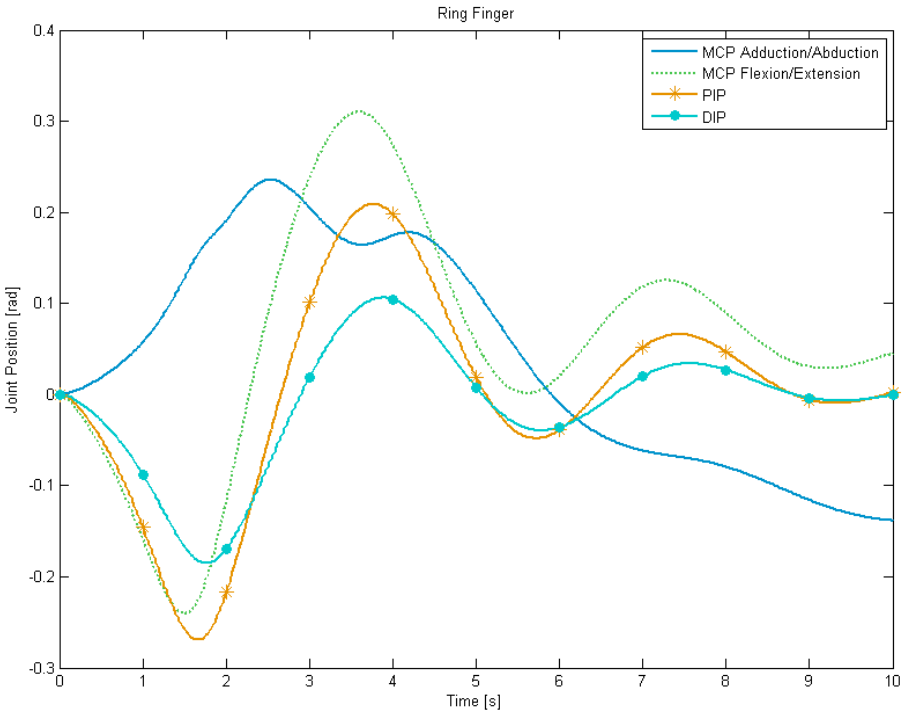

Fig. 5-29 Joint positions of the ring finger.

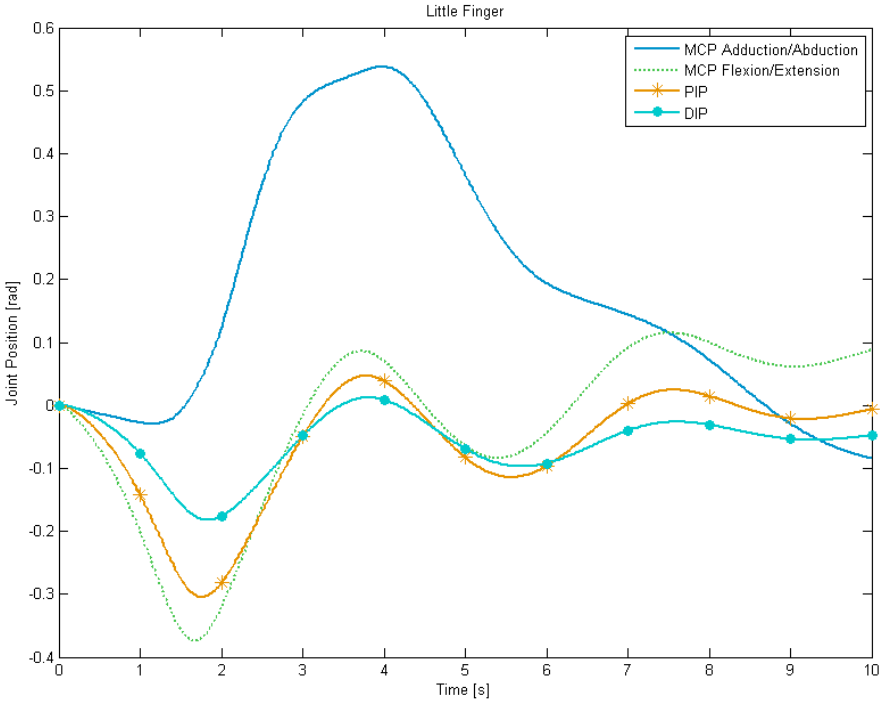

Fig. 5-30 Joint positions of the little finger.

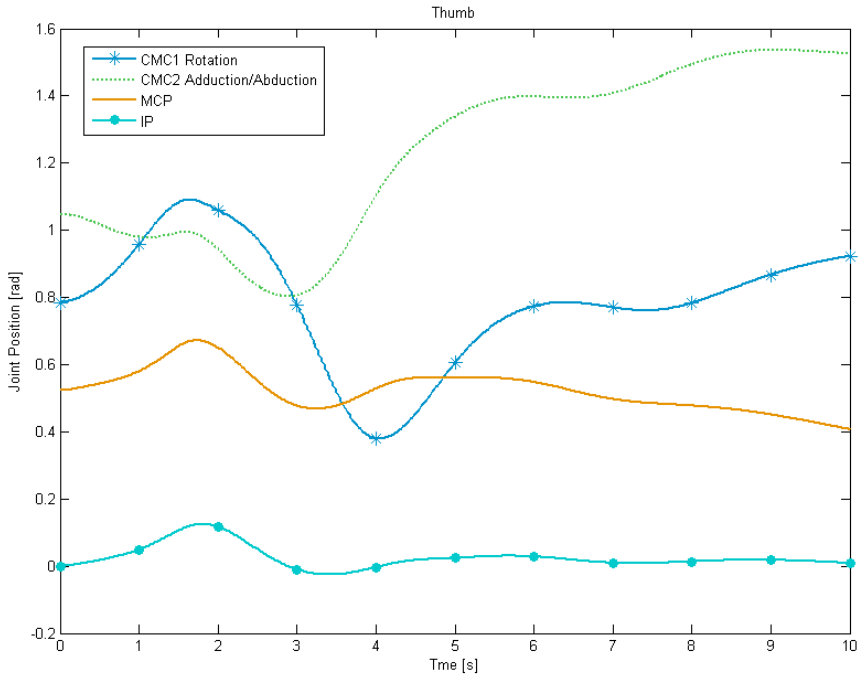

Fig. 5-31 Joint positions of the thumb.

5.4.2. Hand model with joint limits and elastic joints

This test adds joint limits and elasticity on the joints. There are two sources of elasticity on the human hand: one from the joints themselves and from the muscles.

The elasticity on each joint was estimated and is detailed on Table 5-IV, along with the corresponding joint limits.

Table 5-IV Elasticity parameters and joint limits of the hand model.

Joint	Spring Constant [N]	Spring initial position [rad]	Lower limits [rad]	Upper limits [rad]
1	$\begin{bmatrix} 2 & -4 \\ 0 & 2 \end{bmatrix}$	$\begin{bmatrix} \frac{\pi}{32} & 0 \end{bmatrix}^T$	$\begin{bmatrix} -\frac{\pi}{10} & 0 \end{bmatrix}^T$	$\begin{bmatrix} \frac{\pi}{4} & \frac{\pi}{2} \end{bmatrix}^T$
2	$\begin{bmatrix} 2 & 0 \\ 0 & 5 \end{bmatrix}$	$\begin{bmatrix} 0 & 0 \end{bmatrix}^T$	$\begin{bmatrix} -\frac{\pi}{10} & 0 \end{bmatrix}^T$	$\begin{bmatrix} \frac{\pi}{10} & \frac{\pi}{2} \end{bmatrix}^T$
3	$\begin{bmatrix} 2 & 0 \\ 0 & 1 \end{bmatrix}$	$\begin{bmatrix} 0 & 0 \end{bmatrix}^T$	$\begin{bmatrix} -\frac{\pi}{10} & 0 \end{bmatrix}^T$	$\begin{bmatrix} \frac{\pi}{10} & \frac{\pi}{2} \end{bmatrix}^T$
4	$\begin{bmatrix} 2 & 0 \\ 0 & 1 \end{bmatrix}$	$\begin{bmatrix} 0 & 0 \end{bmatrix}^T$	$\begin{bmatrix} -\frac{\pi}{10} & 0 \end{bmatrix}^T$	$\begin{bmatrix} \frac{\pi}{10} & \frac{\pi}{2} \end{bmatrix}^T$
5	$\begin{bmatrix} 2 & 0 \\ 0 & 1 \end{bmatrix}$	$\begin{bmatrix} 0 & 0 \end{bmatrix}^T$	$\begin{bmatrix} -\frac{\pi}{10} & 0 \end{bmatrix}^T$	$\begin{bmatrix} \frac{\pi}{10} & \frac{\pi}{2} \end{bmatrix}^T$
6	1	$\frac{\pi}{4}$	0	$\frac{\pi}{2}$
7	1	0	0	$\frac{\pi}{2}$
8	1	0	0	$\frac{\pi}{2}$
9	1	0	0	$\frac{\pi}{2}$
10	1	0	0	$\frac{\pi}{2}$
11	2	$\frac{\pi}{3}$	0	$\frac{\pi}{2}$
12	1	$\frac{\pi}{6}$	$\frac{\pi}{4}$	$\frac{\pi}{2}$
13 to 17	1	0	0	$\frac{\pi}{2}$

For the joint with two degrees of freedom, the spring constant has to be a 2x2 matrix, where the wrist joint (joint 1) is a special case. The wrist joint is partially coupled, because the first DoF (adduction/abduction of the wrist) moves when the second DoF (flexion/extension of the wrist) moves. To simulate this coupling the entry in the first row and second column of the spring constant matrix was set to a value different of zero, -4 in this case.

The results of this simulation can be seen on Fig. 5-32 and Fig. 5-33 to Fig. 5-38, the screenshots and joint positions, respectively.

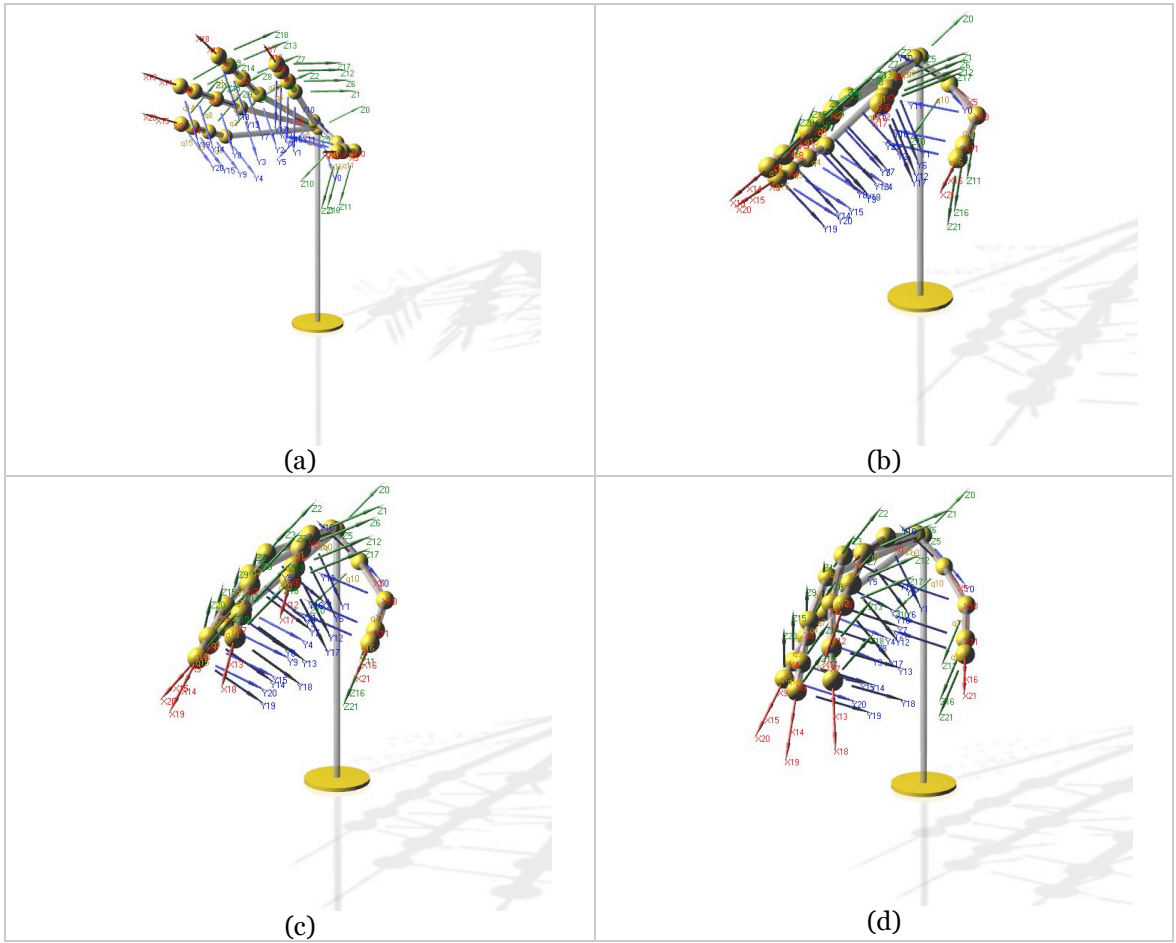

Fig. 5-32 Screenshots of the simulation at t = 1s (a), t = 1.5s (b), t = 2.5s (c), t = 10s (d).

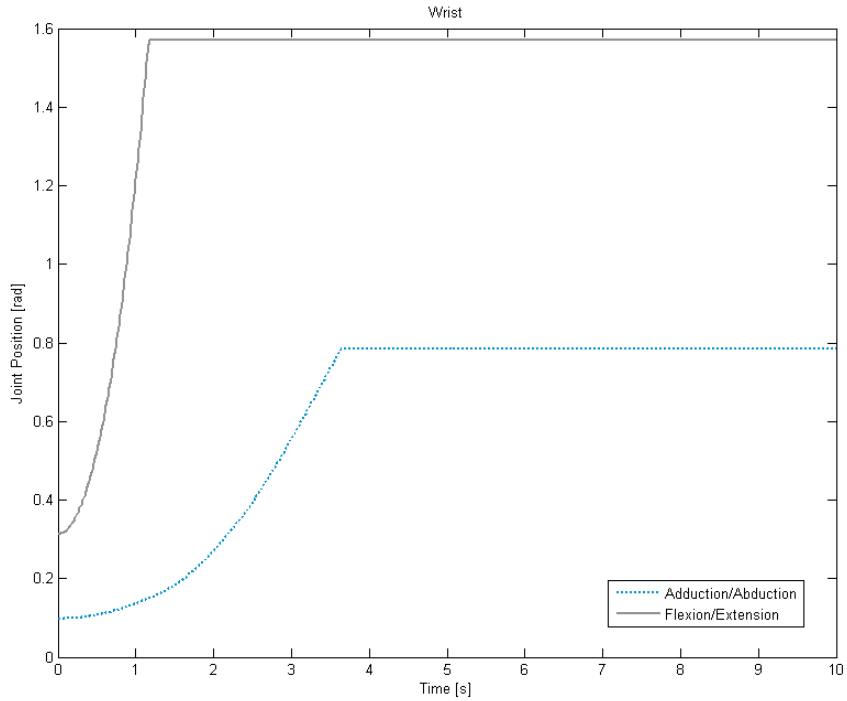

Fig. 5-33 Joint positions of the wrist.

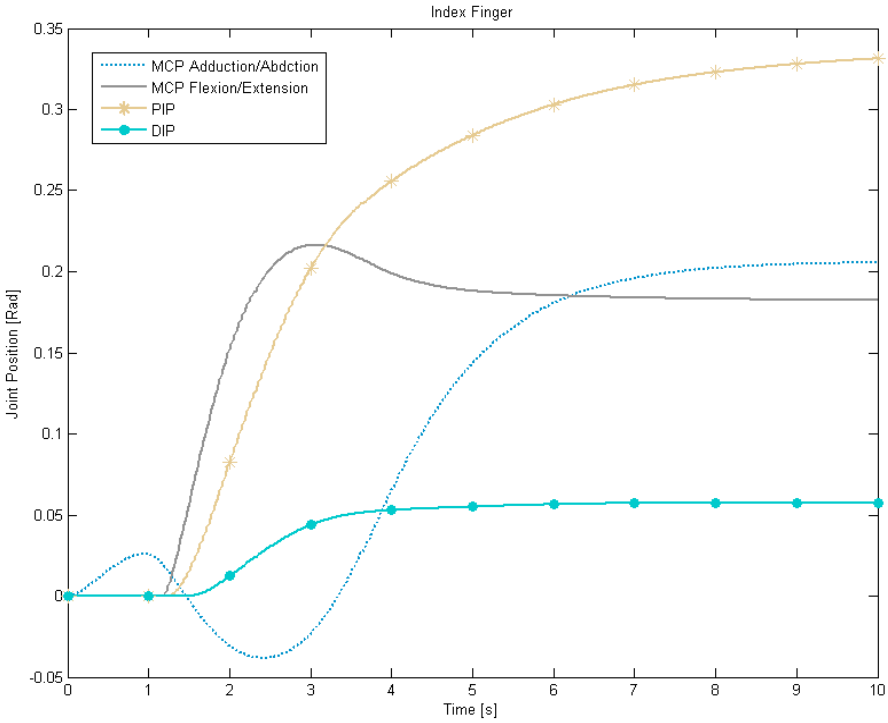

Fig. 5-34 Joint positions of the index finger.

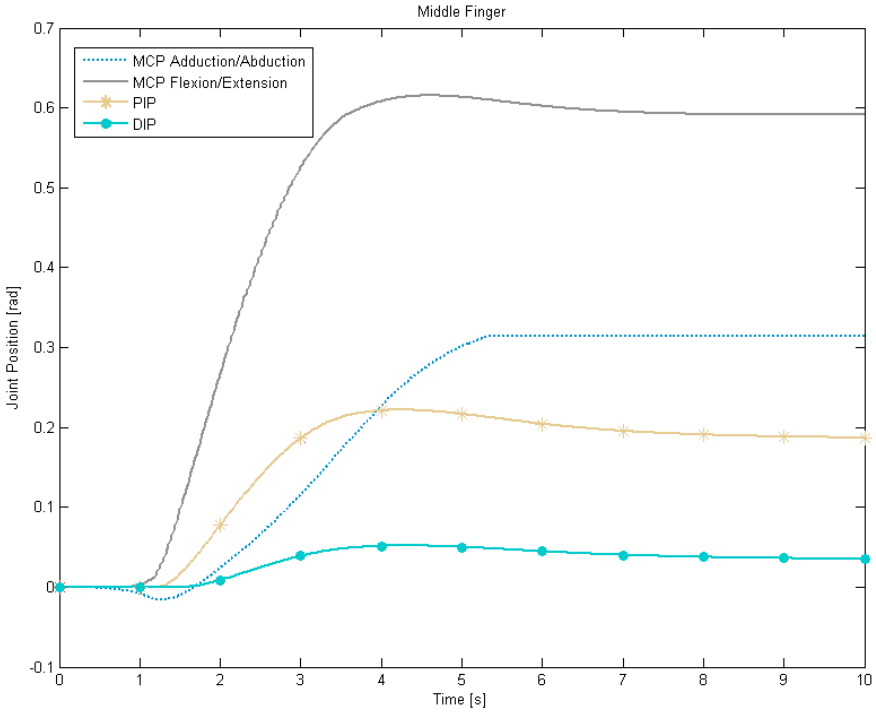

Fig. 5-35 Joint positions of the middle finger.

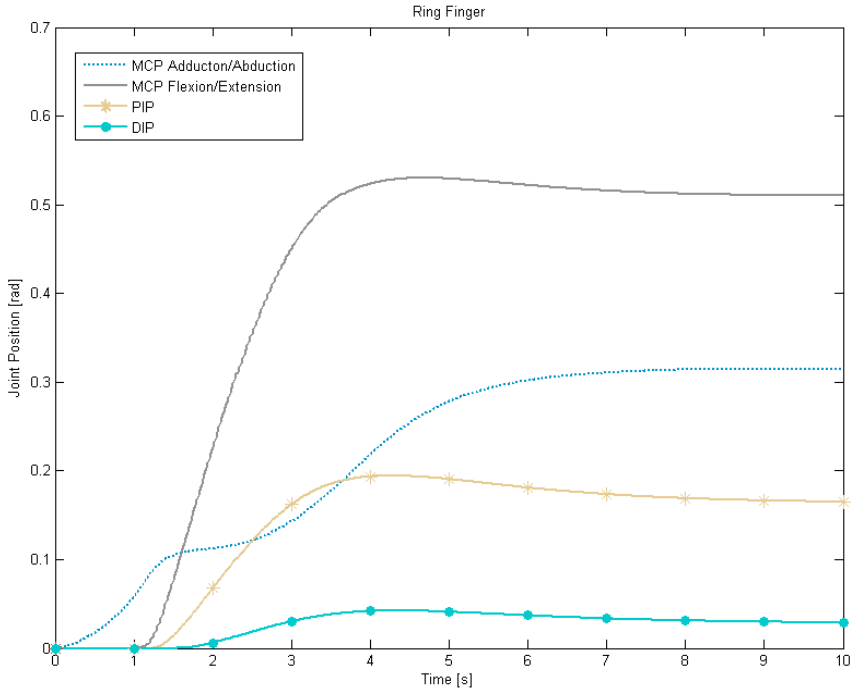

Fig. 5-36 Joint positions of the ring finger.

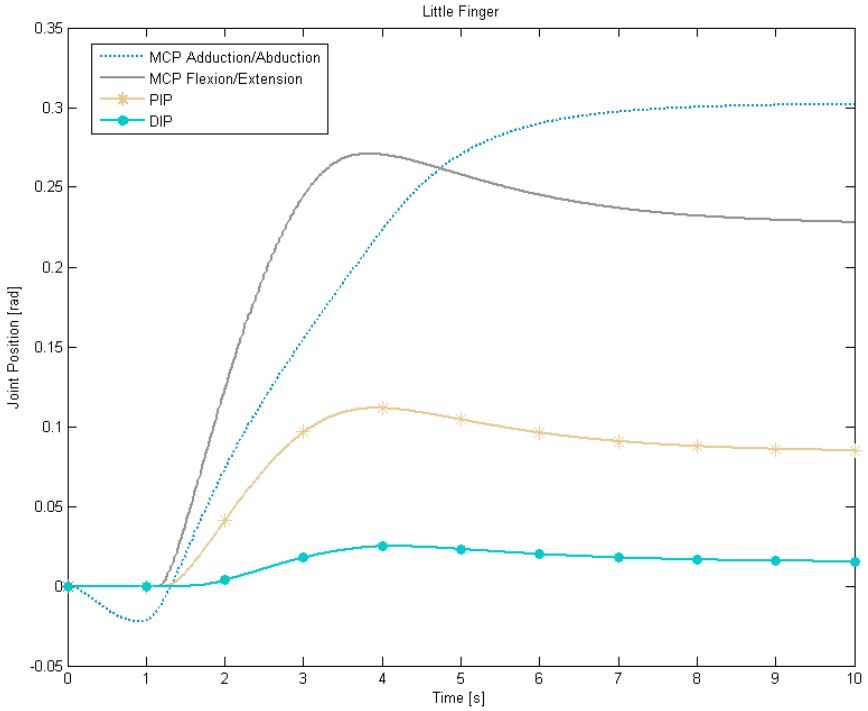

Fig. 5-37 Joint positions of the little finger.

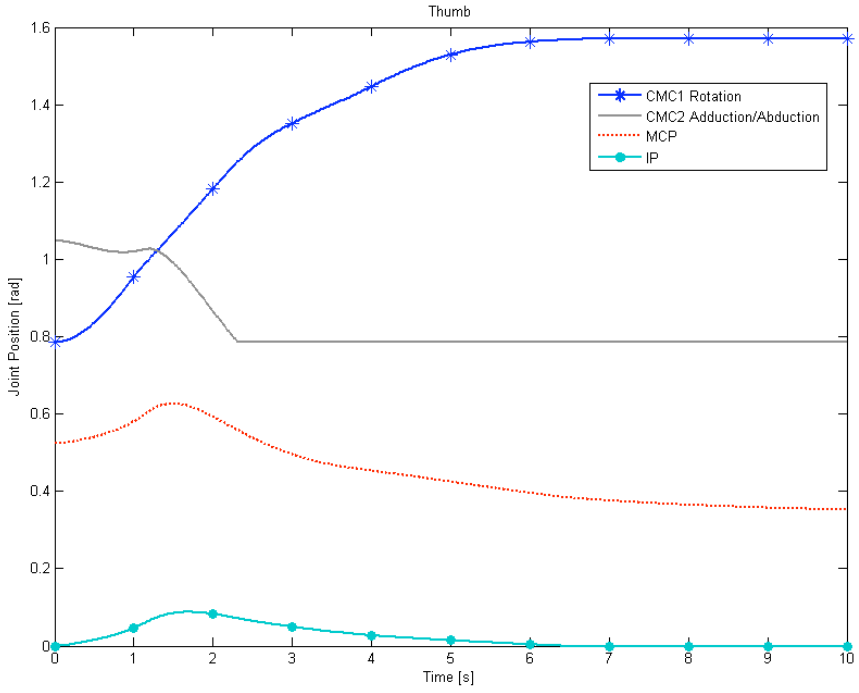

Fig. 5-38 Joint positions of the thumb.

From Fig. 5-33 to Fig. 5-38 one can see that the system is over-dampened, as expected, and since the weight of the hand rests on the wrist joint, the flexion/extension DoF is the first to saturate. Also, since the hand is not symmetric, it will rotate saturating too the adduction/abduction DoFs of the wrist.

Chapter 6

CONCLUSIONS

The objective of this thesis work was to simulate the dynamic behavior of the human hand. This simulation will be used in the design process of a five-fingered human hand prosthesis, helping estimating the characteristics of the actuators, the type of control system its parameters.

The simulation uses a Newton-Euler-based algorithm, the Articulated-Body Algorithm. This algorithm has two main advantages: it is a $O(n)$ algorithm and it can be modified to handle almost any kind of robotic structure. To simulate the human hand, the ABA was adapted to handle tree-structures, articulated structures with one base and multiple end-effectors, and a new algorithm, the IABA, was developed to work together with the ABA, enabling it to handle the severe disturbances caused by the impact and contact with other objects in the environment.

The simulation was tests against a set of benchmark examples yielding, for each structure, the expected results. The results of the human hand simulation were also as expected, however both spring constant and dampening coefficients of the joints

had to be estimated. These constants could not be found in the literature, because the main objects of study in medicine of the hand are the illnesses and deformations, and their cure. References [10] and [11] contain some biometric properties of the hand, but these are limited to the measures of the length and angles of the bones. It is very difficult to measure the mechanical properties of the muscles and tendons, because in order to function, the human muscles must be living tissue, unlike reptile muscles that can function without a supporting living being. In fact, the majority of tests done with muscles are with reptilian tissues and then the results are extrapolated to the human and mammal cases.

6.1. Future work

The current algorithm already simulates most of the aspects of the dynamics of the hand, however there are, still, some particularities of the hand to be correctly modeled. The first is the variable joint limits of the MTC joints of the finger (with the exception of the thumb), the joint limits of the adduction/abduction DoF depend on the position of the flexion/extension DoF, being tighter as the flexion increases. The second is finding the actual dampening coefficients and spring constants, to properly model the human hand in all it complexity. Finally, the contact part of the algorithm should be optimized since it is one of the heaviest parts of the algorithm.

As was mentioned in Chapter 1, the greater objective of this work is to build a hand prosthesis. The first thing to do is, using the model of the hand, getting the characteristics of the actuators and to get an initial set of parameters of the control system. With all this done, the next step will be to build the prosthesis itself, starting with the supporting structure, the bones, and then the actuator and control system.

REFERENCES

[1] Guo, G., Gruver, W. A., Qian, X., "A Robotic Hand Mechanism with Rotating Fingertips and Motor-Tendon Actuation", IEEE Robotics & Automation Magazine, 1991, pp. 1023-1028.

[2] Lee, Y. K., Shimoyama, I., "A skeletal framework artificial hand actuated by pneumatic artificial muscles", Proceedings of 1999 IEEE International Conference on Robotics & Automation, Detroit, 1999, pp. 926-931.

[3] Crisman, J. D., Kanojia, C., Zeid, I.,"Graspar: A flexible, easily controllable robotic hand", IEEE Robotics & Automation Magazine, 1996, pp. 32-38.

[4] Ambrose, R. O., Aldridge, H., Askew, R. S., Burridge, R. R., Bluethmann, W., Diftler, M., Lovechick, C., Magruder, D., Rehnmark, F., "Robonaut: NASA's Space Humanoid", IEEE Intelligent Systems, July/August 2000, pp. 57-63.

[5] Kyberd, P.J., Pons, J.L., "A Comparison of the Oxford and Manus Intelligent Hand Prostheses", Proceedings of the 2003 IEEE International Conference on Robotics & Automation, Taipe, 2003, pp. 3231-3236.

[6] Okuno, R., Fujikawa, M., Yoshida, M., Akazawa, K., "Biomimetic Hand Prosthesis with Easily Programmable Microprocessor and High Torque Motor", Proceedings of the 25th Annual International Conference of the IEEE EMBS, Cancun, 2003, pp. 1674-1677.

[7] Weghe, M. V., Rogers, M., Weissert, M., Matsuoka, Y., "The ACT Hand: Design of the Skeletal Structure", Proceedings of the 2004 IEEE

International Conference on Robotics & Automation, New Orleans, 2004, pp.3375-3379.

[8] Gialias, N., Matsuoka, Y., "Muscle Actuator Design for the ACT Hand", Proceedings of the 2004 IEEE International Conference on Robotics & Automation, New Orleans, 2004, pp. 3380-3385.

[9] Gray, H., "Gray's Anatomy", 16th ed., Senate, London, 2003.

[10] Tubiana, R., ed. "The Hand", vol. 1, WB. Saunders, Philadelphia, 1981.

[11] Mow, V. C., Huiskes, R., *Basic Orthopaedic Biomechanics and Mechano-Biology*, 3rd ed., Lippincott Williams & Wilkins, pp. 42-50, 2005.

[12] R. Featherstone, *Robot Dynamics Algorithms*, Kluwer Academic Publishers, 1984.

[13] R. Featherstone, "A Divide-and-Conquer Articulated-Body algorithm for Parallel O(log(n)) Calculation of Rigid-Body Dynamics. Part 1: Basic Algorithm", *The International Journal of Robotics Research*, vol. 18, no. 9, pp. 867-875, 1999.

[14] R. Featherstone, "A Divide-and-Conquer Articulated-Body algorithm for Parallel O(log(n)) Calculation of Rigid-Body Dynamics. Part 2: Trees, Loops and Accuracy", *The International Journal of Robotics Research*, vol. 18, no. 9, pp. 876-892, 1999.

[15] K.S. Anderson, S. Duan, "Highly Paralelizable Low Order Algorithm for the Dynamics of Complex Multi-rigid-body Systems", AIAA Jnl. Guidance, Control & Dynamics, vol. 23, no. 2, pp. 355-364, 2000.

[16] K.S. Anderson and J.H. Critchley, "Improved 'Order-N' Performance Algorithm for the Simulation of constrained multi-Rigid-Body Dynamic Systems", *Multibody systems Dynamics*, vol. 9, pp. 185-212, 2003.

[17] K. Yamane and Y. Nakamura, "Parallel O(log N) Algorithm for Dynamic Simulation of Humanoid Robots", *Proceedings of the HUMANOIDS'06 2006 IEEE-RAS International Conference on Humanoid Robots*, pp. 554-559, 2006.

[18] S. McMillan, D. E. Orin, R. B. McGhee, “Efficient Dynamic Simulation of an Underwater Vehicle with a Robotic Manipulator”, *IEEE Transactions on Systems, Man and Cybernetics*, vol. 25, no. 3, pp. 1194-1206, 1995.

[19] D. Baraff, “Fast contact force computation for nonpenetrating rigid bodies”, *Computer Graphics Proceedings*, Annual Conference Series, Orlando, pp. 23-34, 1994.

[20] D. Baraff, “An Introduction to Physically Base Modeling: Rigid Body Simulation I — Unconstrained Rigid Body Dynamics*”, Siggraph’97 Course Notes*, pp. D1-D31, 1997.

[21] D. Baraff, “An Introduction to Physically Base Modeling: Rigid Body Simulation II — Nonpenetration Constrains”, *Siggraph’97 Course Note*s, pp. D32-D68, 1997.

[22] B. Mirtich, “Impulse-based Dynamic Simulation of Rigid Body Systems”, *Doctoral Thesis*, cap. 5, pp. 132-147, 1996.

[23] Y. Wang, “On Impact Dynamics of Robotic Operations”, *Technical Report (CMU-RI-TR-86-14)*, Carnegie-Mellon University, 1986.

[24] T. Liu and Y. Wang, “Computation of Multi-Rigid-Body Contact Dynamics”, *Proceedings of the 2004 IEEE International Conference on Robotics & Automation*, New Orleans, pp. 3220-3225, 2004.

[25] Y.F. Zheng, H. Hemani, “Mathematical modeling of a robot collision with its environment”, *IEEE Transctions on Systems, Man, and Cybernetics*, vol. 14, no. 3, 1984.

[26] A. Tornambé, “Global regulation of planar robot arm striking a surface”, *IEEE Transactions on Automatic Control*, vol. 41, no. 10, pp. 1517-1521, 1996.

[27] R.W. Cottle, J.S. Pang, R.E. Stone, *The linear complementarity problem*, Academic Press, 1992.

[28] M. Anitescu, S.K. Arason, V.I. Arnold, I.U. Bronshtein, “Formulating dynamic multi-body contact problems with friction as solvable linear complementary problems”, *Reports on computational Mathematics*, no. 93/1996, Dept. of Mathematics, University of Iowa, USA, 1996.

[29] D. Baraff, “Fast contact force computation for non-penetrating rigid-bodies”, *Algorithmica*, vol. 10, pp. 292-352, 1994.

APPENDIX

A1. Velocities and accelerations of the 5-link serial structure:

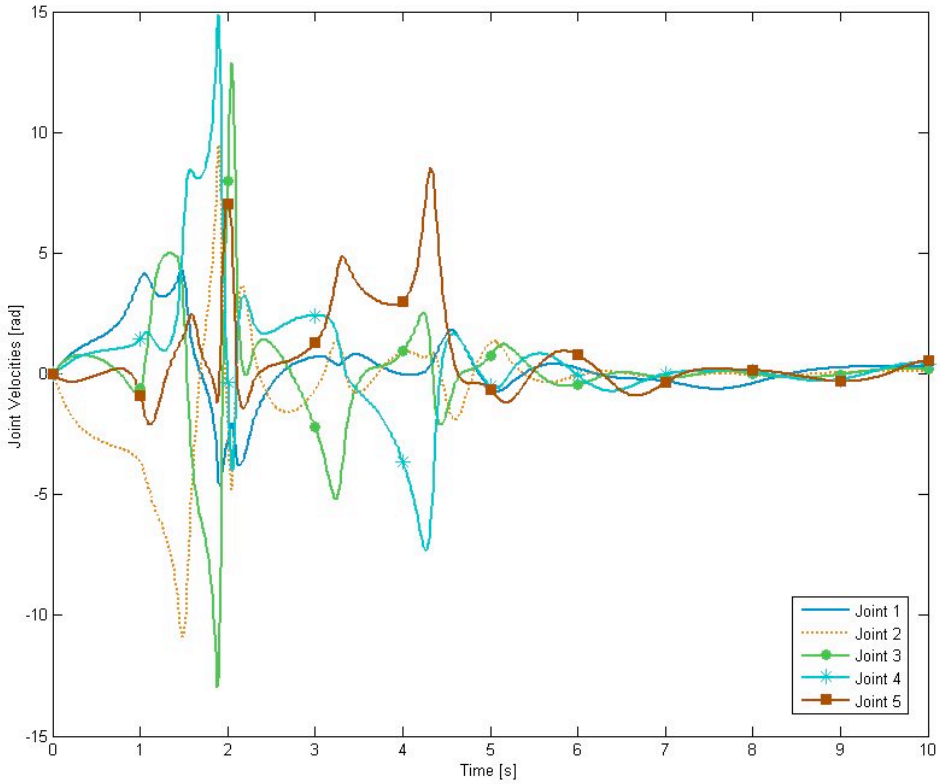

Joint Velocities

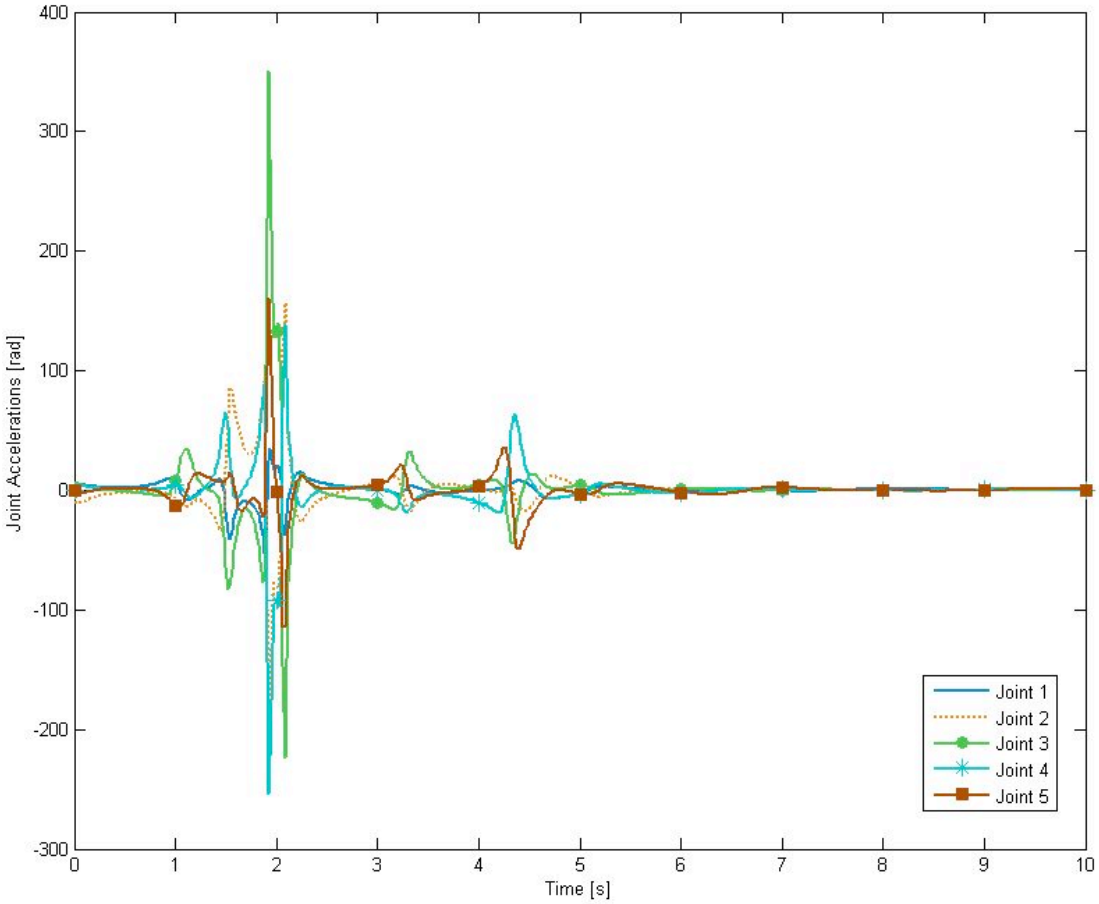

Joint accelerations

A2. Velocities and Accelerations of the 10-links tree structure in free fall.

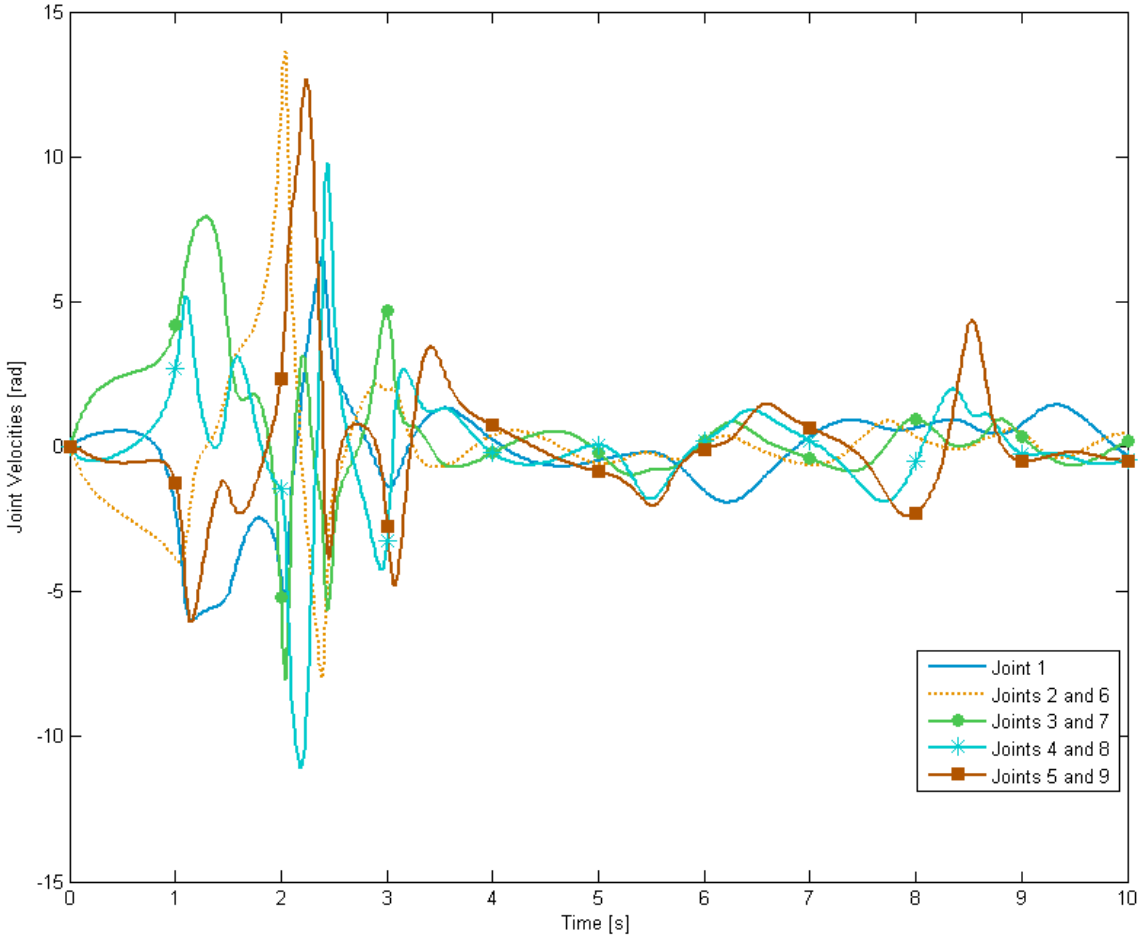

Joint Velocities

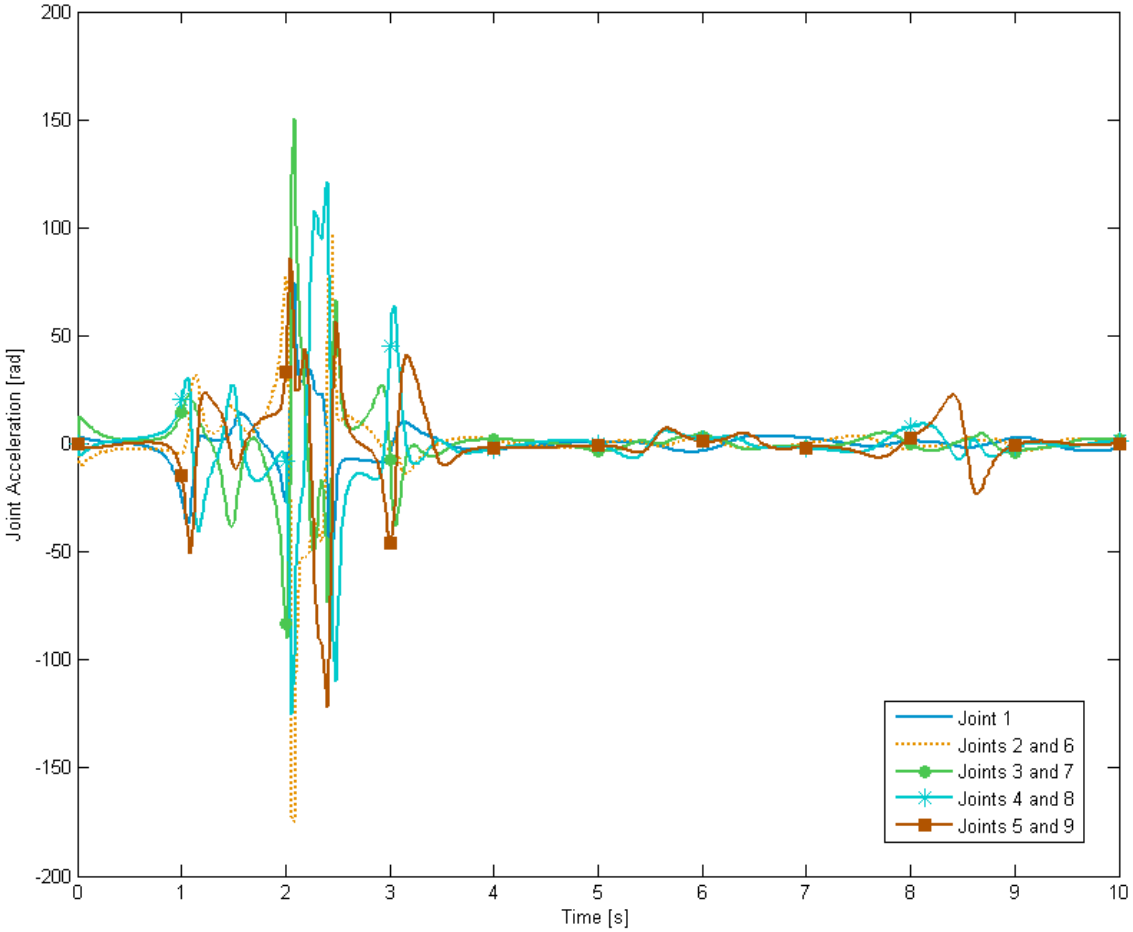

Joint Accelerations

A3. Velocities and accelerations of the 10-link tree structure with applied torques.

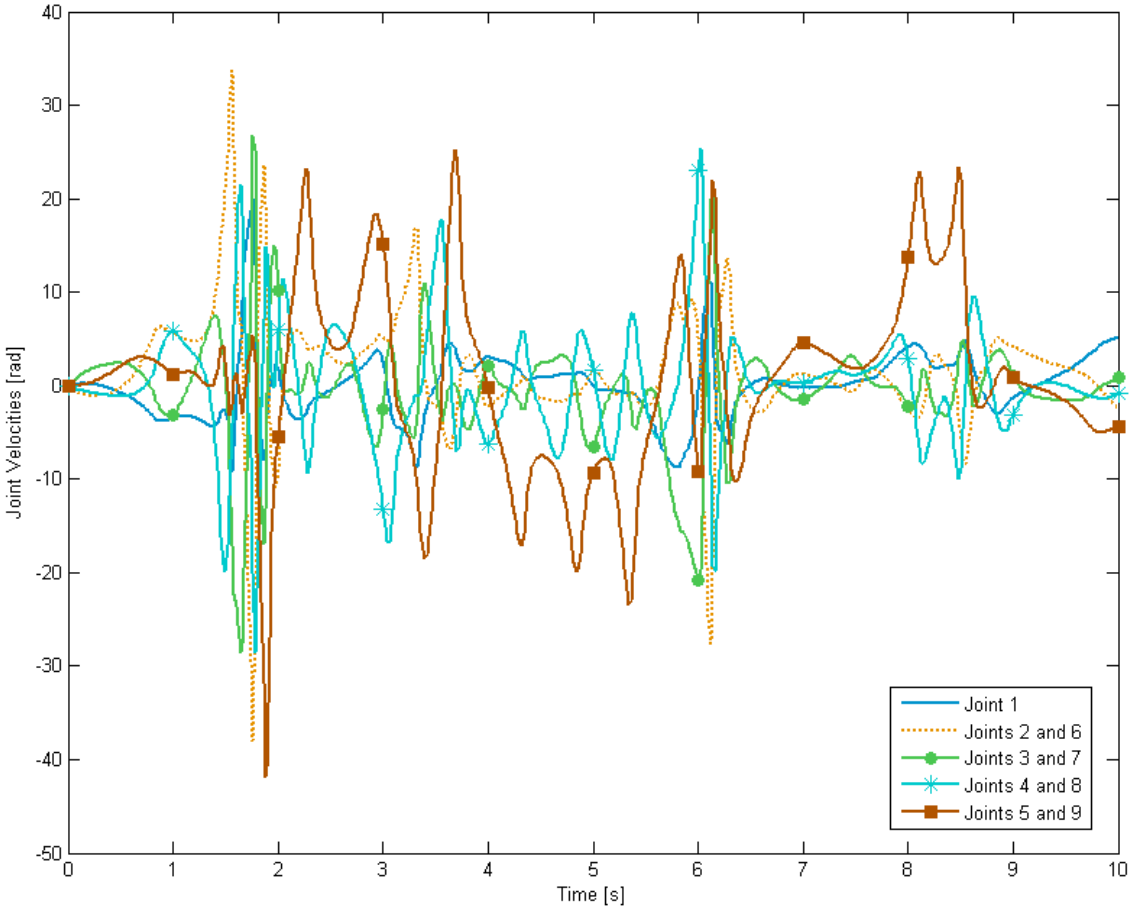

Joint velocities

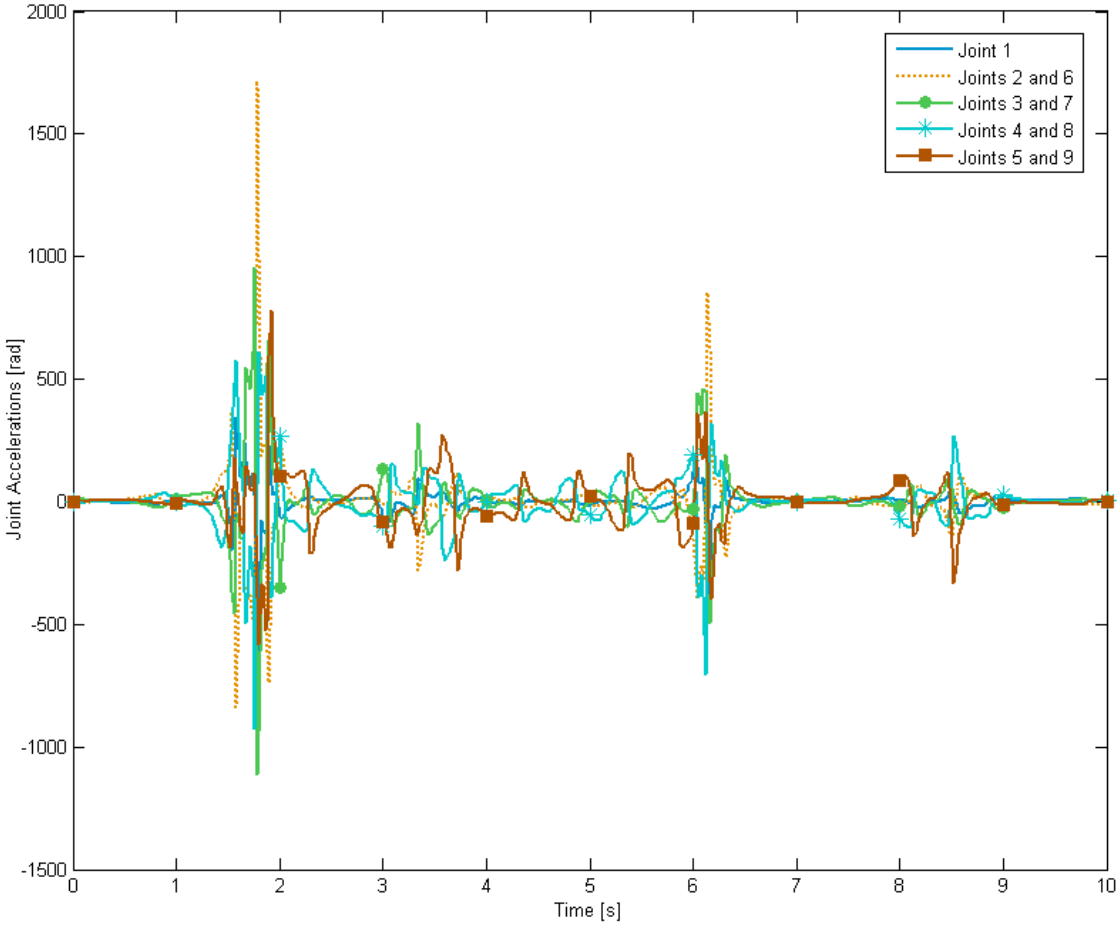

Joint Accelerations